University of Alberta

Sulfide Stress Cracking Susceptibility of Low Alloy Steels for Casing Application in Sour Environments

by

Weishan Huang

A thesis submitted to the Faculty of Graduate Studies and Research
in partial fulfillment of the requirements for the degree of

Master of Science
in
Chemical Engineering

Department of Chemical and Materials Engineering

Fall 2012
Edmonton, Alberta

Abstract

Sulfide stress cracking (SSC) resistance of casing steels with different alloying chemistries (i.e. Ti-B and Mn-Cr-Mo) was evaluated using constant load tensile test and slow strain rate test in NACE-TM0177 environment. SSC resistance in terms of RA_{H2S}/RA_{air} and time to failure was found to decrease with increase of material strength. For more susceptible steels, a mix mode of transgranular and intergranular fracture was observed. For less susceptible steels, intergranular fracture was less prevalent.

Inclusions were found to be the dominant factor contributing to SSC susceptibility. Mn-Cr-Mo steels were more susceptible to inclusions than Ti-B steels. Cracking was found to be initiated mainly from elongated inclusions such as MnS, Al-Si-O, or large globular Ca-enriched oxide inclusions. Clustering of inclusions were main SSC initiation sites. The distribution and morphology of carbides played an important role in SSC propagation. A uniform microstructure with fine globular carbides was found to improve SSC resistance.

Acknowledgements

I would like to express my deep appreciation to both of my supervisors Dr.Jingli Luo and Dr. Hani Henein, for their guidance and support throughout the course of this study.

Natural Science and Engineering Research Council of Canada (NSERC) and Evraz Inc. NA are gratefully acknowledged for funding of the project. I also want to express my special thanks to Mr. Josiah Jordan and Dr. Laurie Collins for their helpful comments and suggestions during this study and their kindness in enabling me to use their facilities in Regina to conduct a part of my work.

In addition, I am deeply grateful for the assistance of the following people: Dr. Iouri Makarov, Ms. Gayle Hatchard, Ms. De-ann Rollings, and the CME machine shop staff.

Finally, I would like to thank my family and my boyfriend Qingxun Low for their encouragement and selfless support.

TABLE OF CONTENTS

LIST OF TABLES

LIST OF FIGURES

LIST OF SYMBOLS

A	Actual cross sectional area of the gauge section of the specimen, mm^2
$C_{critical}$	Critical hydrogen concentration for crack initiation, mol/cm^3
$C_{irreversible}$	Hydrogen concentration in irreversible traps, mol/cm^3
$C_{reversible}$	Hydrogen concentration in reversible traps, mol/cm^3
K_{1C}	Fracture toughness in inert environment
K_{ISSC}	Critical stress intensity factor
K_{1th}	Threshold stress intensity coefficient
P	Desired load, N
RA_{air}	Reduction in area in air, %
RA_{H2S}	Reduction in area in hydrogen sulfide medium, %
S	Applied stress, MPa
S_c	Critical stress factor

LIST OF ABBREVIATIONS

AES	Auger Electron Spectroscopy
AISI	American Iron and Steel Institute
API	American Petroleum Institute
ASTM	American Society for Testing and Materials
CaO	Calcium oxide
CaS	Calcium sulfide
Ca/S	Calcium/sulfur ratio
CH_3COOH	Acetic acid
CIR	Computerized Inclusion Rating
C-Mn	Carbon-Manganese
Cr-Mo	Chromium-Molybdenum
DCB	Double Cantilever Beam
EDX	Energy Dispersive X-ray Spectroscopy
ERCB	Energy Resources Conservation Board
FeS	Troilite
FeS_2	Pyrite
Fe_7S_8	Pyrrhotite
Fe_9S_8	Kansite
HIC	Hydrogen Induced Cracking
HRB	Rockwell B hardness
HRC	Rockwell C hardness
H_2S	Hydrogen sulfide
IRP	Industry Recommended Practice
JIS	Japanese Industrial Standard
Mn-Cr	Manganese-chromium
Mn-Cr-Mo	Manganese-chromium-molybdenum
MnS	Manganese sulfide
Mo_2C	Molybdenum carbides

NACE	National Association of Corrosion Engineers.
NaCl	Sodium chloride
OCTG	Oil Country Tubular Goods
RAR	Reduction in Area Ratio (RA_{H2S}/RA_{air})
SEM	Scanning Electron Microscope
SMYS	Specified Minimum Yield Strength
SSC	Sulfide Stress Cracking
SSRT	Slow Strain Rate Test
TEM	Transmission Electron Microscope
Ti-B	Titanium-Boron
TiN	Titanium-Nitride
Ti-Nb(C,N)	Titanium-Niobium Carbonitride

1. INTRODUCTION

As conventional oil and gas reserves are exhausted, there is a greater reliance on sour gas reserves. Many oil and gas wells in Western Canada contain significant amounts of hydrogen sulfide, termed sour wells, and these wells become increasingly sour over time. Casing is the steel pipe that is inserted in oil or gas wells during drilling operations to line the wellbore and prevent the well from caving and contamination. Hydrogen sulfide (H_2S) comes to be present in sour wells naturally as a result of the action of bacteria with sulfate or elemental sulfur in low-oxygen conditions [1].

The steelmakers must cope with the increasing demand for casing products used in sour service. Increasing development of deeper sour wells requires the casing or tubing materials with higher strength. In addition, resistance to Sulfide Stress Cracking (SSC) is one of the crucial properties the steels must possess in aqueous H_2S environment to ensure a safe and successful oil and gas production. This imposes a severe restriction on the selection of tubing and casing material for drilling operations because SSC resistance is known to decrease with increasing yield strength [2].

SSC is a hydrogen embrittlement phenomenon which results in a steel failing well below its yield strength. The presence of H_2S promotes the diffusion of hydrogen atoms into the steel resulting in hydrogen embrittlement rather than bubbling off harmlessly from the steel surface [3]. Intensive research over recent decades has aimed at studying SSC behaviors of low alloy steels due to their lower costs.

Numerous research results have been published on the effect of cleanliness and microstructures on the SSC resistance of steels. Initiation of SSC cracks is usually associated with steel cleanliness. The size and morphology of the inclusions has a strong effect on cracking susceptibility. Inclusions with sharp interface provide easy crack path and are ideal cracking nucleation sites. Elongated MnS inclusions and coarse cubic TiN particles are

known to be the most detrimental initiation sites [3]. The effect of microstructure on SSC resistance has been examined for acicular ferrite, ferrite-pearlite, upper bainite/lower bainite, quenched and tempered martensite. A ferrite-pearlite microstructure has been found to be the worst structure[4], while quench and tempered martensite is found to perform the best in sour environments[5]. Acicular ferrite has attracted much attention recently due to its high toughness and has been also been reported to have satisfied SSC performance[2]. However, despite years of investigations, the mechanisms of SSC remain unclear and are still not clearly defined. Very little information is available on the causes and dominant factor contributing to SSC behaviors. This will be the focus for this study.

A number of experimental methods have been developed for SSC assessments. Constant load tension test is one of the most widely used methods and will be the test method for this study. Constant load test involves applying a constant load to a specimen in a H_2S environment for the duration of 720 hours. This test generates a failure/no failure result and time-to-failure data is reported. Slow strain rate test (SSRT) is a rapid material screening test and involves applying a constant strain rate to the specimen while it is exposed to a corrosive sour environment. SSRT test will be used in this study as well to compare with the results from the constant load test.

This thesis is divided into seven chapters. A detail review of the literature followed by the objectives of this study will be given in Chapter 2. In this Chapter a review will be given of the SSC process and the effect of environmental and metallurgical factors on SSC susceptibility. In Chapter 3, experimental procedures for SSC evaluation, inclusion quantification, and carbide characterization are presented. Results of SSC tests, inclusion and carbide characterization are given in Chapter 4. In Chapter 5, a discussion of SSC cracking behaviors, effect of cleanliness, effect of carbide morphology is presented. Conclusions of the findings are in Chapter 6 followed by a recommendation of future work in Chapter 7.

2. LITERATURE REVIEW

2.1 Sour service

A sour service environment refers to the environment containing a significant amount of H_2S and may result in failure of material by means of cracking or corrosion. Such sour environments are found in oil and gas production wells, transmission pipelines or equipment in the refinery process. In Alberta, the Energy Resources Conservation Board (ERCB) defined sour service in Directive 10 by the partial pressure of H_2S. Any oil and gas wells that contain H_2S equal or greater than 0.3 kPa are categorized as sour wells [6]. NACE standard MR0175 [7] further defines the severity of sour environment based on the partial pressure of H_2S and the pH of the fluid as shown in Figure 2.1. The vertical line 0.3 kPa differentiates the sweet from sour wells. Region 0 in Figure 2.1 refers to the environments with the partial pressure of H_2S less than 0.3 kPa. The SSC regions 1, 2, 3 refer to the severity of exposure in sour environment that may result in SSC. Selection guidelines for materials used in different regions of Figure 2.1 are documented in NACE MR-0175[7]. Critical sour wells are also defined in ERCB and Industry Recommended Practice (IRP) volume 1 based on the potential release rate of H_2S and the proximity of population centres or areas [8, 9].

The presence of hydrogen sulfide promotes the absorption of hydrogen into the steels thus leading to several hydrogen embrittlement mechanisms such as sulfide stress cracking (SSC) and hydrogen induced cracking (HIC) that will be discussed later. Failures have been documented in oil/gas well casing and tubulars, pipelines, and pressure vessels[10].

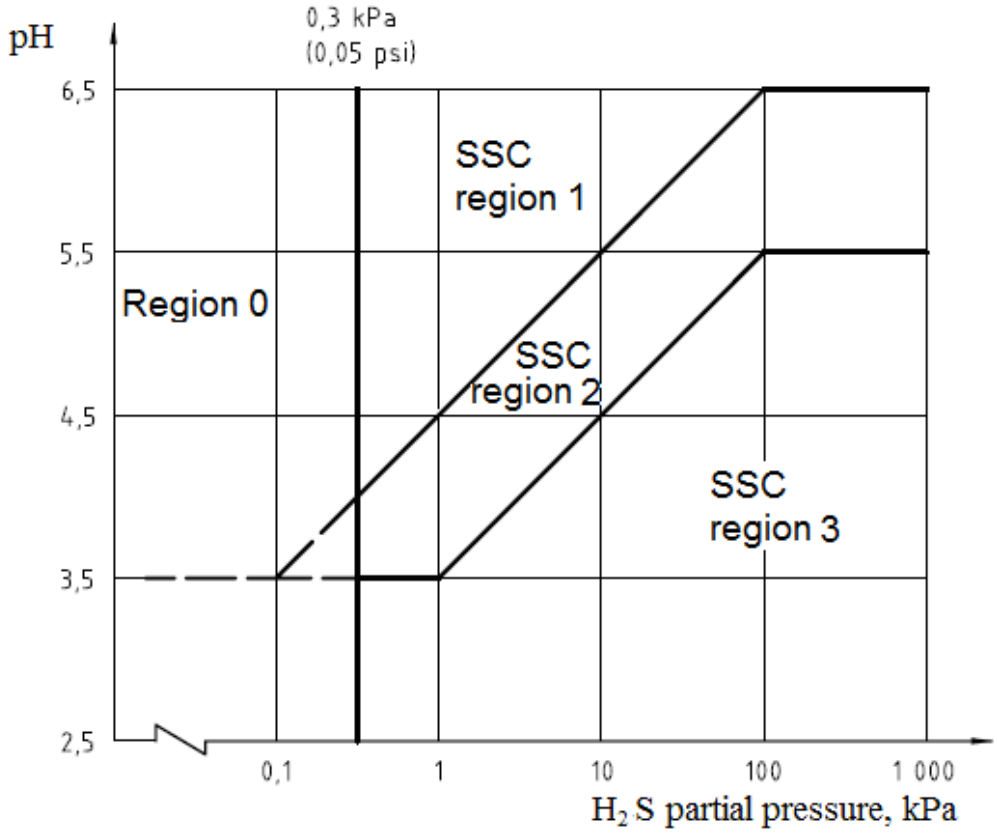

Figure 2.1: The severity of sour environments [7].

2.2 Casing steel requirements for sour environment

American Petroleum Institute (API) has specified the basic requirements for casing, tubular goods and drill pipes to ensure safe applications in the oil and gas industry. For many years, J55*, K55*, L80*, C90*, and T95* grades Oil Country Tubular Goods (OCTG) have been used in drilling and production operations when H_2S is present. These grades are considered acceptable to use at all temperatures in sour service if they meet the Specified Minimum Yield Strength (SMYS) in API requirements [7]. Though J55 and K55 have been used in sour environment, they are not specifically designed for that application [11]. API standardized L80, C90, and T95 casing and tubing products specifically for sour service applications in 1975, 1985 and 1989, respectively [11]. These three grades are quench-and-temper heat treated casing grades and are required by API-5CT specification to have controlled hardness and yield strength. For L80, it must not be harder than 23 Rockwell

* These casing grades are defined in API-5CT specification [12].

C and yield strength is controlled to within a variation of 15 ksi (i.e. in the range of 80-95ksi) [11, 12]. L80 (type 1) casing can be produced either by a seamless process or by a forming and welding process. Similarly for C90 and T95, their hardness must not exceed 25.4 Rockwell C and yield strength not exceed 15ksi from the SMYS in API-5CT specification [11, 12]. C90 and T95 casings are required to be produced using the seamless process due to the concern about the non-homogeneous microstructure in the weld regions for electric welded products [11, 12]. For exploration of deeper sour gas wells, higher strength grades, namely C100, C105, and C110 have not been standardized by API yet, but NACE International has established the minimum requirements for these grades in the NACE MR-0175 standard. These three grades are also required to have a yield strength not to exceed 15 ksi from the SMYS and maximum hardness of 30 Rockwell C [11, 12]. Cr-Mo alloying is required for these grades with quench-and-temper heat treatment. This is because Cr-Mo low alloy steels are considered to provide better SSC resistance compared to C-Mn alloyed steels [5, 11].

Among all the API casing grades, L80 is the most widely used casing grade in sour service and it is the main focus in this study. L80 grade offers several advantages compared to other casing grades: It is known that SSC resistance decreases with yield strength of steels and L80 has the lowest yield strength among all the API quench-and-temper casing grades; Quench and temper heat treatment could lead to a more uniform microstructure than in the as-rolled condition which could improve the SSC resistance[9]. In addition, higher casing grades with similar sour service performance as L80 require more alloying thus adding more cost to production [9].

Both API-5CT specification and ERCB-Directive 10 have documented the basic chemistry and processing requirements for L80 type 1 steel used for sour service (Table 2.1 and Table 2.2). ERCB imposes additional constraints on carbon, manganese, phosphorus, and sulfur contents for sour well operations in Alberta. For critical sour well drilling, more constraints of alloying elements

and processing methods are documented in IRP Volume 1 and included in Table 2.1 and 2.2 for comparison. It should be noted that the IRP volume 1 requires minimum of 90% martensite before tempering while the API-5CT standard only requires minimum of 50% martensite. The IRP requirement can result in a more uniform microstructure for improving SSC resistance of casings.

Table 2.1: Alloying chemistry requirements (wt%) for L80 used in sour service [6, 8, 9, 12].

	API-5CT	ERCB Directive 10	IRP Volume 1
C	0.43	0.32 (0.35% if S < 0.005% and P < 0.015%)	0.32
Mn	1.90	1.40 (1.45% if S < 0.007%)	1.20
P	0.030	0.020 (0.025% if S <0.005%)	0.020
S	0.030	0.010 (0.015% if Cr + Mo > 0.60%)	0.010
P+S	---	0.025 (0.030% if Cr + Mo > 0.30%; 0.035% if Cr + Mo >0.6%)	---
Ni	0.25	0.25	0.20
Si	0.45	0.45	0.35
Cu	0.35	0.35	0.20
Cr	---	---	1.30
Mo	---	---	0.65
Al	---	---	0.04
V	---	---	0.05
Nb	---	---	0.04
Ti	---	---	0.04
B	---	---	0.0025

Table 2.2: Processing requirements for L80 using in sour service [6, 8, 9, 12].

	API-5CT	ERCB Directive 10	IRP Volume 1
Minimum Tempering temperature (^{o}C)	566	621	---
Hardenability	50%martensite; HRC(min.)= 52x(%C)+21	---	90%martensite; HRC (min.) =58×(%C)+27
Prior Austenite Grain size	---	---	7 or finer
Yield strength (MPa)	552-655	---	---
Ultimate Tensile Strength (MPa), min.	655	---	---
Hardness (HRC) reading, max.	---	22	---
Hardness average value (HRC), max.	23	21	---
Toughness- Charpy V-Notch min.(J) @ 0^{o}C, Longitudinal	27-47	80	---
Toughness- Charpy V-Notch min.(J) @ 0^{o}C, Transverse	14-24	55	---

2.3 Role of hydrogen sulfide in sour environment

Intensive research efforts over decades have been focused on the degradation of materials due to the presence of H_2S in sour environments. Not only it is an extremely toxic gas, H_2S also contributes to corrosion damage and environmental embrittlement problems. Hence it is important to understand different degradation processes caused by H_2S and to develop special materials to protect the integrity of the oil and gas production systems.

2.3.1. Hydrogen sulfide corrosion

Corrosion is the most common form of damage due to the presence of H_2S in sour environments. Hydrogen sulfide is commonly known as an acid gas because it can be dissolved in aqueous environment to form acidic and corrosive solutions. Corrosion damage to steels is manifest by the formation of thick sulfide scale, large weight loss of metal, and formation of pitting. Figure 2.2 [13] shows an image of corrosion damage of an oil well tubing. Corrosion rate of low alloy carbon steels in sour production environments can exceed 2.5 mm/year and it tends to increase when pH of the aqueous environment decreases [14].

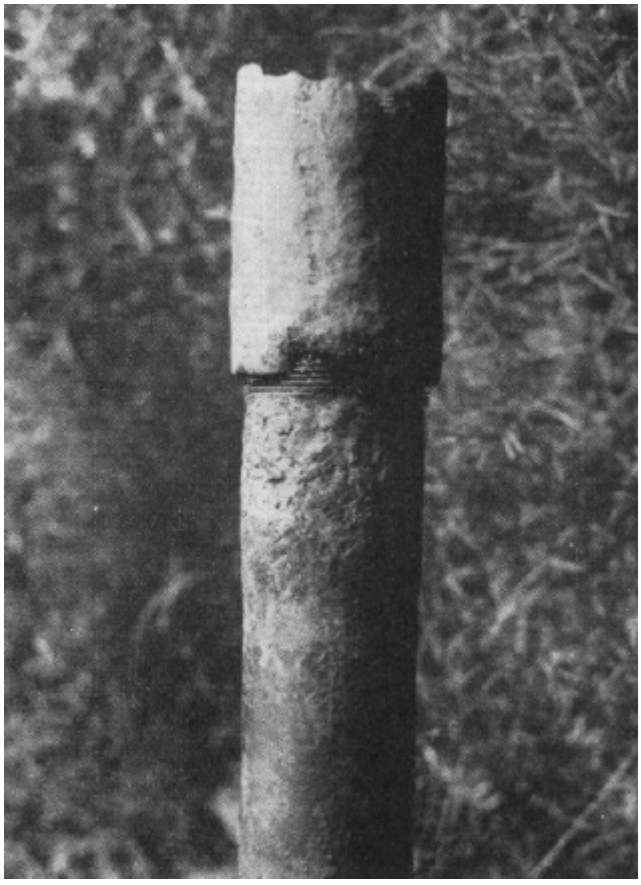

Figure 2.2: Hydrogen sulfide corrosion attack of oil well tubing after 24 months of service [13].

In an acidic environment (pH <5), hydrogen sulfide is quite stable and

dissolves in an aqueous solution to react with iron (Figure 2.3) [15]. For other conditions with higher pH levels, other sulfide species, i.e. HS^- and S^{2-}, are stable and can be present in solution to result in other sulfide corrosion mechanisms.

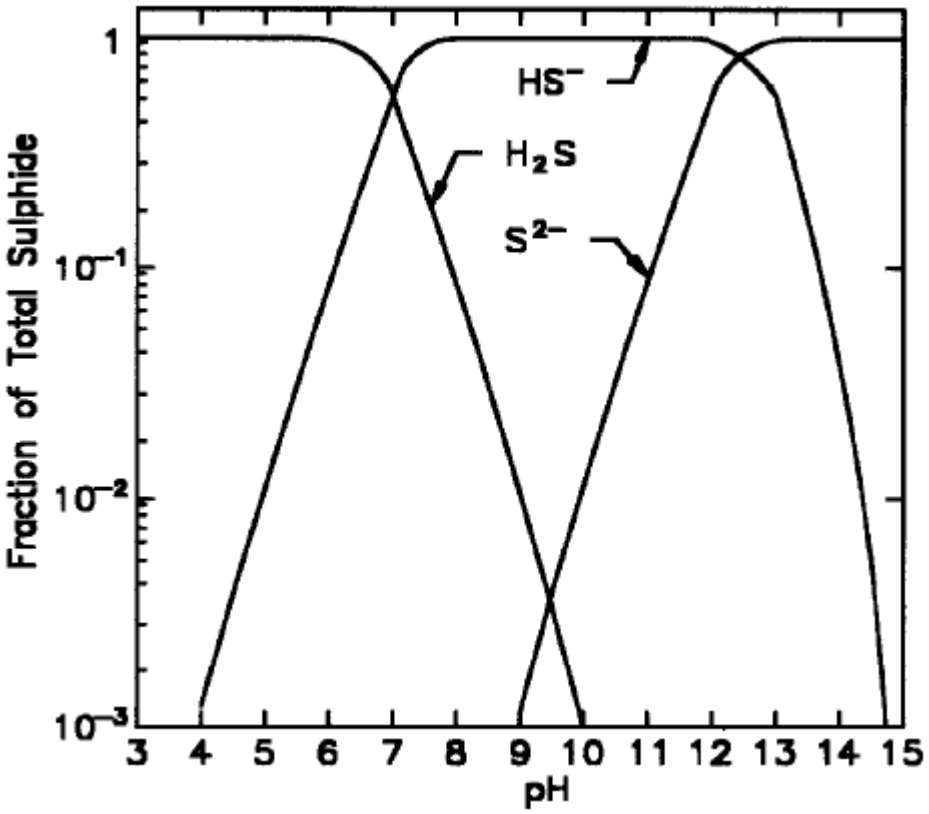

Figure 2.3: Relative fraction of sulfide species at different pH conditions [15].

A typical corrosion mechanism in an anaerobic environment is given by equations 2-1 to 2-4 [15, 16]:

Anode: $$Fe \rightarrow Fe^{2+} + 2e^- \quad (2\text{-}1)$$

Cathode: $$H_2S + H_2O \rightarrow H^+ + HS^- + H_2O \quad (2\text{-}2)$$

$$HS^- + H_2O \rightarrow H^+ + S^{2-} + H_2O \quad (2\text{-}3)$$

Net reaction: $$Fe + H_2S_{(aq)} \rightarrow FeS + 2H^0 \quad (2\text{-}4)$$

Depending on the pH, the concentration of H_2S, the presence of other reacting species in solution (e.g. carbon dioxide, chlorides), and the oxidizing

potential of the environment, different molecular forms of iron sulfide product may form. These include FeS (troilite), FeS_2 (pyrite), Fe_7S_8 (pyrrhotite), Fe_9S_8 (kansite) and they have a significant effect on the kinetics of the corrosion process [15]. At lower hydrogen sulfide concentration (2mg/L), troilite and pyrite are the predominant species present in the reaction products. Corrosion rate is low under these conditions because the crystal lattice of troilite and pyrite have relatively less defects and can reduce the diffusion of iron cation to protect iron from further corrosion [15, 17]. At higher hydrogen sulfide concentration (>20mg/L), the sulfide film consists mostly of kansite. The corrosion rate increases since kansite has a more imperfect crystal lattice compared to troilite and pyrite and it doesn't possess protective properties[15, 16]. The compositions of corrosion products also depend on pH levels. At lower pH, around 3 to 4, troilite and pyrite are the major components in the sulfide film, whereas at pH levels from 6.6 to 8.8, kansite is the dominant component and the film is unprotected [16]. For other pH levels, the sulfide film can be a mixture of kansite, troilite and pyrite.

2.3.2. Sulfide stress cracking (SSC)

Sulfide stress cracking is a material failure that occurs when a susceptible material is under the combined action of a H_2S-containing aqueous environment and presence of external stress, either applied or residual [18]. Failure is commonly encountered for moderate and high strength steels used in production tubular, oil and gas refinery equipment, and transmission pipelines. The first SSC failure occurred in the early 1950s on tubular steels with hardness greater than 22 HRC [3]. The NACE International organization then made a recommendation to heat treat the steels to hardness less than 22 HRC to prevent SSC and found it reasonably successful in practice [3].

Sulfide stress cracking is generally recognized to result from hydrogen embrittlement and it is observed most intensively near room temperature condition. Before SSC process could occur, a number of critical steps

including hydrogen adsorption, evolution and absorption must take place. As shown in reaction 2-4, one of the products from hydrogen sulfide corrosion is hydrogen atoms that evolved at cathodic sites. In most corrosive environments, the majority of the hydrogen atoms adsorbed on the metal surface would recombine to form molecular hydrogen gas and bubble off harmlessly from the surface[15]. However with the presence of H_2S or other dissolved sulfur species (i.e. HS^-, S^{2-}), the recombination reaction can be "poisoned" thus forcing the hydrogen atoms absorbed in the metal to cause hydrogen embrittlement. Hydrogen either absorbed from the environments or retained in the steels from the steelmaking process can result in unexpected catastrophic failures [19]. This process is illustrated in Figure 2.4 [19]. Consequently, the presence of hydrogen sulfide leads to an increase of hydrogen charging in steels compared to conditions without hydrogen sulfide[15].

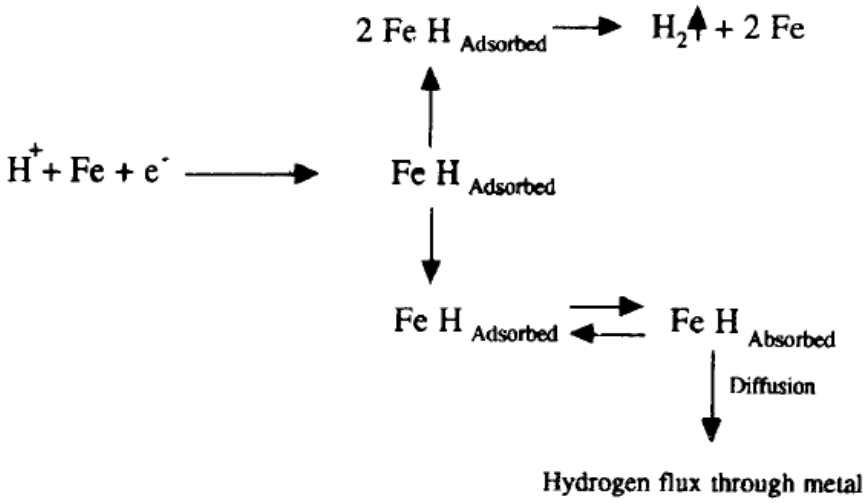

Figure 2.4: Illustration of hydrogen evolution and entry process [19].

Initiation of SSC usually occurs at high stressed regions where hydrogen is likely to accumulate or be trapped, i.e. grain boundaries, inclusions, segregation bands, dislocations etc. Figure 2.5 illustrates SSC cracks initiated from the stress concentrator. Multiple crack initiation sites could occur near

stress concentrators [20]. SSC crack propagation is facilitated by connecting brittle microcracks in the steel matrix to the main crack until catastrophic failure results at stresses well below the yield strength of steel. Due to the increase of hydrogen charging in H_2S medium, there exists a threshold stress intensity coefficient below which SSC will not occur [21]. This threshold value is much lower than the fracture toughness in inert environment [21]. As a result, steel that operates safely in a normal condition would become dangerous in hydrogen charging environment.

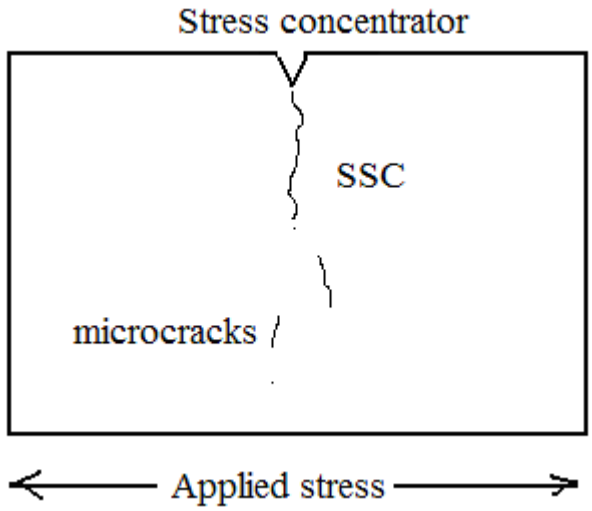

Figure 2.5: Illustration of SSC cracks.

SSC usually occurs in a brittle manner with a direction perpendicular to the applied stress. Failure features a transgranular or intergranular mode of fracture, or a combination of both. Asahi and his coworkers [22] observed that there exists a critical strength above which the fraction of intergranular cracking increases with the increase of yield strength. Steels with yield strength below the SSC critical strength, the mode of fracture becomes transgranular (Figure 2.6). Increase of intergranular fracture leads to a decrease in SSC resistance in terms of SSC threshold stress (Figure 2.7).

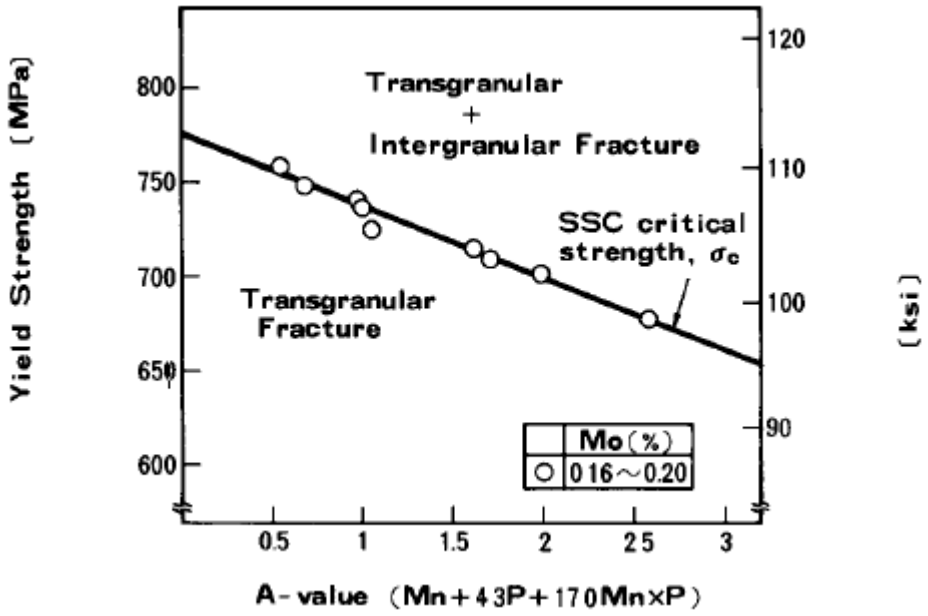

Figure 2.6: Relation of SSC critical strength and mode of fracture[22].

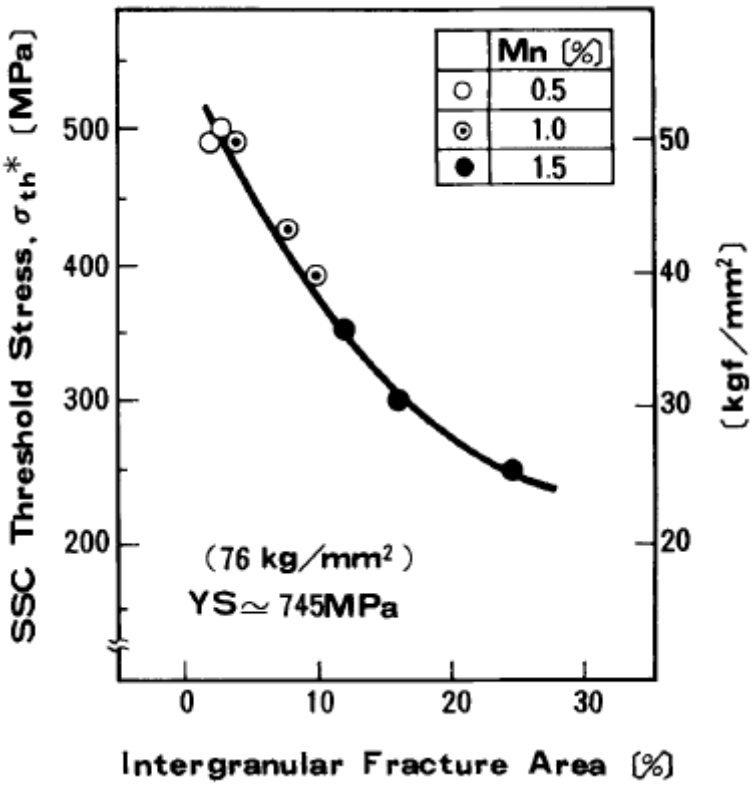

Figure 2.7: Relation of intergranular fracture area and SSC threshold stress [22].

Susceptibility of steels to SSC depends on both environmental factors (e.g pH, concentration of H_2S, temperature) and material factors (chemical composition, strength, microstructure, cleanliness etc). These will be addressed later in Chapter 2.5.

2.3.3 Hydrogen induced cracking (HIC)

Hydrogen induced cracking (HIC) is another type of hydrogen embrittlement problem and can cause failures in transmission pipelines, production tubular, and pressure vessels. HIC is a different failure mechanism from SSC. It can take place in the absence of applied stress and propagate in the axial direction of the pipe, whereas SSC requires the presence of applied stress and a crack propagates perpendicular to the stress direction. Common in both types of cracking mechanisms is a susceptible steel microstructure and the presence of a hydrogen charging environment [9].

The hydrogen entry process as was shown in Figure 2.4 for SSC is the same for HIC. Once in the steels, the hydrogen atoms accumulate at hydrogen traps, such as voids around inclusions and laminations, and they recombine to form hydrogen gas molecules which could lead to a very high internal pressure and eventually crack initiation and propagation (Figure 2.8).

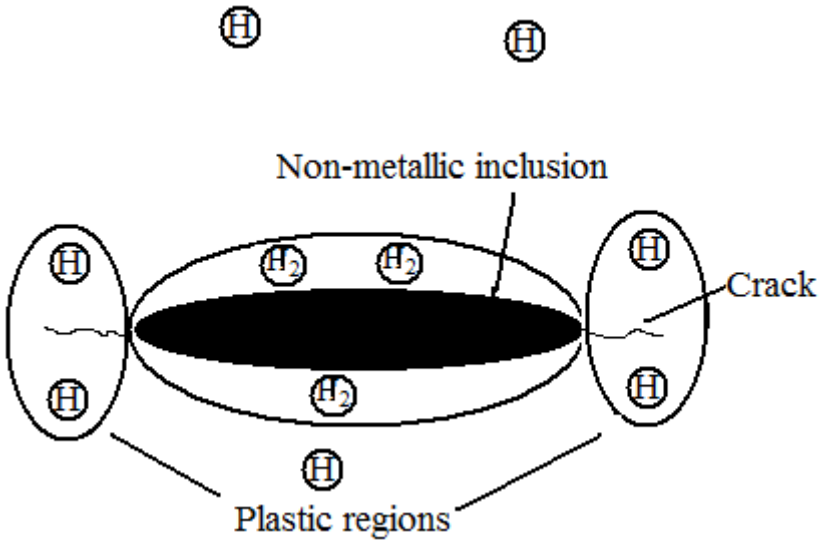

Figure 2.8: Illustration of HIC cracking mechanism [3].

HIC may occur in the form of blistering or a series of step cracks. Figure 2.9(a) and 2.9(b) show examples of both forms respectively [3, 23]. Elongated MnS inclusions and planar arrays of other inclusions are typical initiation sites for HIC [3]. Susceptibility to HIC is related to the sulphur content and inclusion shape in the steel. Increasing sulphur content would increase HIC susceptibility due to the formation of elongated MnS inclusions. Controlling inclusion shape, reducing centerline segregation, and reducing nitrides and oxides are also important for mitigating HIC [3, 9]. Hydrogen induced cracking may propagate by connecting the individual HIC initiating from defects and grow in a stepwise or straight manner parallel to the rolling direction [24].

It should be noted that HIC resistant steel is not necessarily SSC resistant. However, HIC may initiate SSC [9, 24].

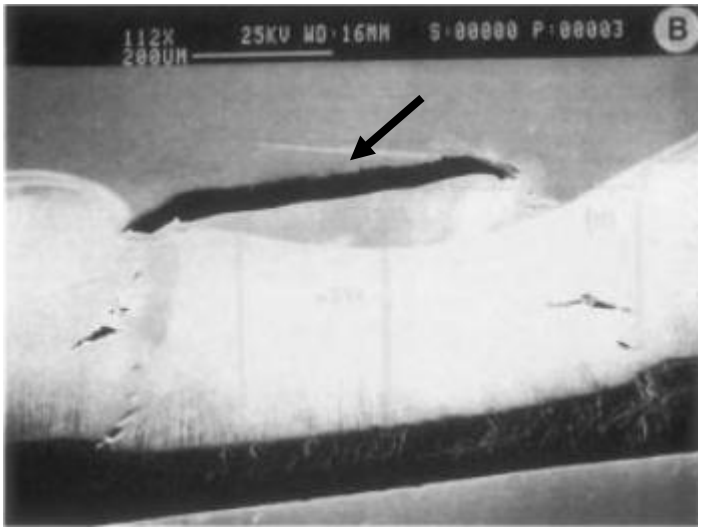

Figure 2.9(a): An example of a blister crack as shown by the arrow [3].

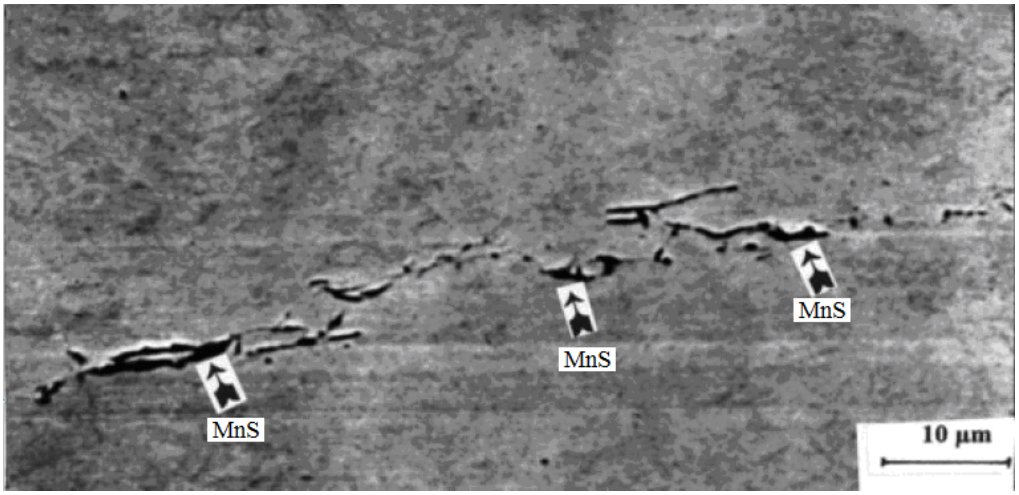

Figure 2.9(b): Stepwise HIC cracks initiating from elongated MnS inclusions [23].

2.3.4 Hydrogen embrittlement mechanisms

There are several popular theories about the mechanisms of hydrogen embrittlement in literature. This topic is still very controversy due to the several viable mechanisms for hydrogen related failures. These theories include the decohesion theory, enhanced local plasticity theory, and the pressure theory.

The decohesion model has been proposed based on Troiano's original theory [25] that electrons from dissolved hydrogen atoms in the lattice fill the incomplete d-bond of the transition metals [10]. The increase of electron density in the lattice causes the increase of inter-atomic spacing thus reducing the cohesive strength in the metal lattice. At any hydrogen-enriched locality in the lattice, the cohesive strength of the metal lattice is reduced. When external stress is applied, it is easy to overcome the resistive cohesive force in the metal lattice which is weakened by the diffusion of hydrogen.

The enhanced plasticity model [26] has been developed based on the fractography study of low strength steels. The increase of mobility of dislocations in hydrogen enriched regions results in an enhanced local plastic deformation. There are more experimental supports for this model. Birnbaum's [27] observations on iron and other materials using very thin specimens in

Transmission Electron Microscope (TEM) has shown that the number of active dislocations suddenly increase when low pressure hydrogen is introduced [10]. This model differs from the decohesion model in that decohesion model involves bond breaking resulting in a cleavage mode of fracture where enhanced plasticity by hydrogen should favour a ductile mode of fracture. Other studies by Morasch and Bahr [28] and Wen et al.[29] have observed different behaviors of hydrogen, this includes hydrogen preventing the dislocation cross slip and the hardening effect of hydrogen.

The pressure theory is an earlier model proposed by Zapffe & Sims [30]. It involves the combination of hydrogen atoms to form molecular hydrogen gas in the voids inside the metals resulting in a build up of internal pressure. The main criticism about this explanation is that it requires a high hydrogen fugacity environment and a high internal pressure for this mechanism to be effective.

Troiano and coworkers [25] refuted the pressure theory because it would predict an initial ductility loss in the material and contradict experimental observations. Troiano's decohesion model proposed that the degree of hydrogen embrittlement should be consistent with the hydrogen concentration in the region of maximum triaxiality in the lattice [19]. Hancock & Johnson[31]'s study observed crack propagation even at very low hydrogen pressure, as measured in sub-atmospheric condition. This contradicts the pressure theory.

2.4 Test methods for SSC

Testing for SSC requires application of a tensile stress and an exposure to a sour aqueous environment. Standard methods for evaluation of SSC resistance of steels have been documented in NACE TM0177 standard [18]. This standard provides techniques for using different types of specimens including smooth tensile bar (method A), bent-beam (method B), C-ring (method C), and double-cantilever-beam (method D). One or more of these

methods can be used to evaluate SSC susceptibility. Method A is a uniaxial tensile test. It offers an un-notched specimen with a well-defined stress state [18]. It is usually applied when the tensile load of the steel surpass 50% of Specified Minimum Yield Stress (SMYS) [8, 9]. Common test load used in method A is 80-85% SMYS. Method B is used for evaluating SSC susceptibility of carbon and low alloy steels in the presence of stress concentration. The compact size of a bent-beam specimen allows testing of localized areas and thin materials [18]. Method C, using a C-ring specimen, is used for evaluating SSC resistance of metals under circumferential loading (i.e. hoop stress). Method D, using a double-cantilever-beam specimen, is used for measuring the SSC resistance of metals to crack propagation. All of these tests could provide a failure/no failure results with test duration from 336 hours (method D) to 720 hours (methods A, B, C).

Resistance to SSC is generally measured by time to failure (methods A, B, C) and other parameters determined from the test, e.g. critical stress factor S_c (method B) and critical stress intensity factor K_{ISSC} (method D). Test environments generally consist of an acidified brine solution with saturated H_2S at 24±3^oC (methods A, B, or C) or 24± 1.7 ^oC for method D [18]. Method A is used for evaluating SSC resistance in this study, as the test equipment is readily available in the lab.

Resistance of HIC is usually evaluated by a standard method documented in NACE TM0284 standard [32] and performed at the same test environments as SSC tests for 96 hours without external stress. However, SSC test is much more comprehensive for evaluating steel performance in sour environment. It is usually not required to perform HIC test if SSC test is performed.

SSRT test is also used for evaluation of SSC resistance. In this test, the specimen is slowly strained in tension and simultaneously exposed to a sour aqueous environment until the specimen fractures. The rate of straining is constant and slow enough to allow time for corrosion and hydrogen absorption to take place. Strain rates in the range of 10^{-4} to 10^{-7}/s are recommended by

ASTM [33] for SSRT. This test initially developed for rapid screening of materials susceptible to Stress Corrosion Cracking (SCC). Because SSRT can give a quick assessment on material's performance, many researchers have started to use it for evaluating SSC [34-36]. The time-to-failure and ductility obtained in the sour environment are usually compared with the results obtained in an inert environment.

2.5 Factors affecting SSC resistance in steel

Sulfide stress cracking of casing steels in sour environment has been a critical issue in industry for many years. Understanding the factors affecting SSC is of critical importance for improving steel design used for sour service. The environmental and metallurgical factors will be reviewed in this chapter.

2.5.1 Environmental factors

SSC susceptibility is strongly influenced by the amount of hydrogen absorption in wet H_2S medium. Many studies have shown that hydrogen diffusion through the steel does not have simple diffusion behaviour as described by Fick's law but is dominated by trapping [37]. Trapping is a process by which dissolved hydrogen atom is bound to some specific sites such as vacancies, dislocations, inclusions, grain boundaries, voids, and boundaries of second phase particles[38]. Several environmental factors, namely pH, H_2S concentration, and temperature have been reported to influence hydrogen uptake and SSC susceptibility of steels. These environmental factors will be reviewed in Chapter 2.5.1.1 and 2.5.1.2.

2.5.1.1 Effect of pH and H_2S partial pressure

The effect of pH has been studied by Snape [39] and Hudgins et al.[40]. Snape [39] tested the SSC performance of API N80 steels at various pH using smooth beam specimens. It was found that an increase in pH leads to a decrease in SSC susceptibility and reported as an increase in time to failure

(Figure 2.10). Snape[39] also observed that hydrogen absorption in steel can increase significantly with decreasing pH (Figure 2.11).

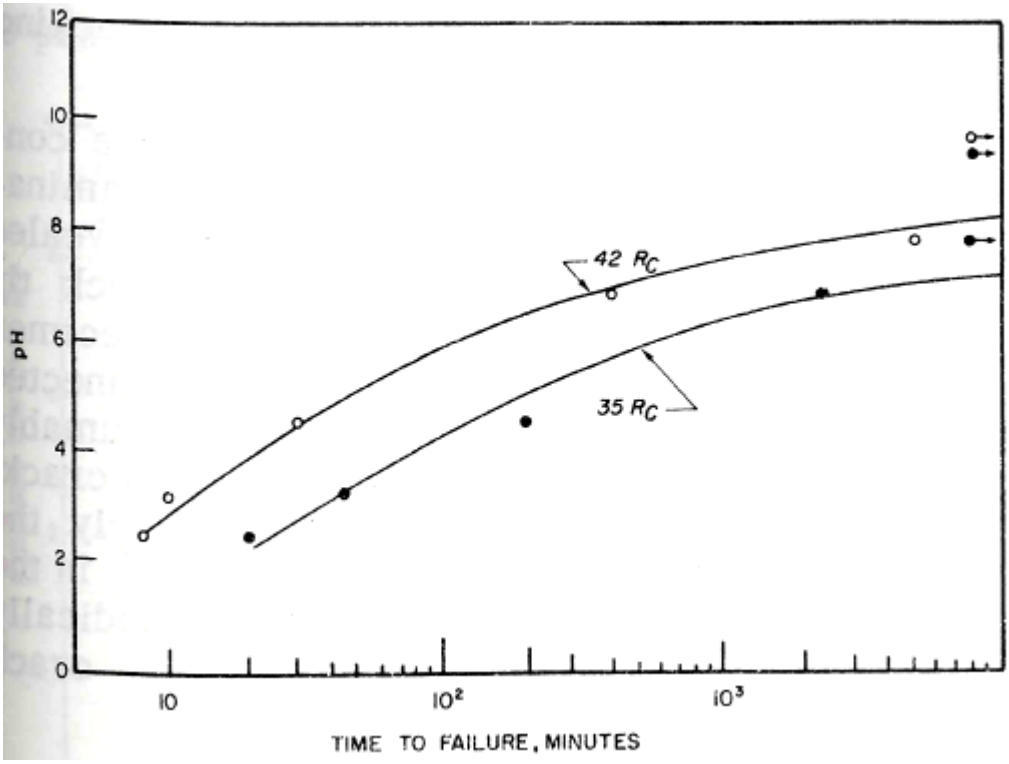

Figure 2.10: Effect of pH of corrodent on time-to-failure of API-N80 steel heat treated to different hardness levels. Applied stress was 90ksi [39].

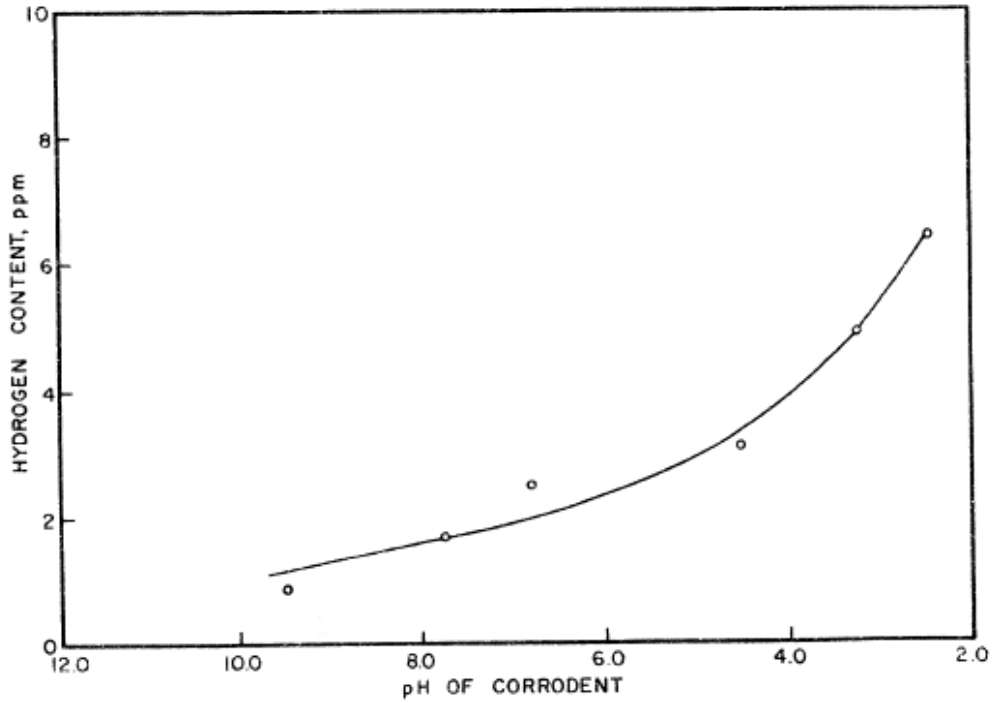

Figure 2.11: Hydrogen absorption as a function of pH for 30 minutes exposure of API-N80 steel. Applied stress 90 ksi[39].

The significant effect of hydrogen sulfide concentration on SSC resistance for various tubular steels was reported by Kane and Greer [41], as shown in Figure 2.12. Except for V150 steels, SSC threshold stress of all steels decreases with increasing hydrogen sulfide concentration. The design of steels suitable for sour oil and gas wells requires knowledge about their yield strength limit and safe operating hydrogen sulfide concentration (Figure 2.13). As seen, each type of steel has a safe H_2S concentration limit below which SSC would not occur on specimen with applied stress equivalent to 100% of their yield strength. This concentration limit decreases with the increase of yield strength [41].

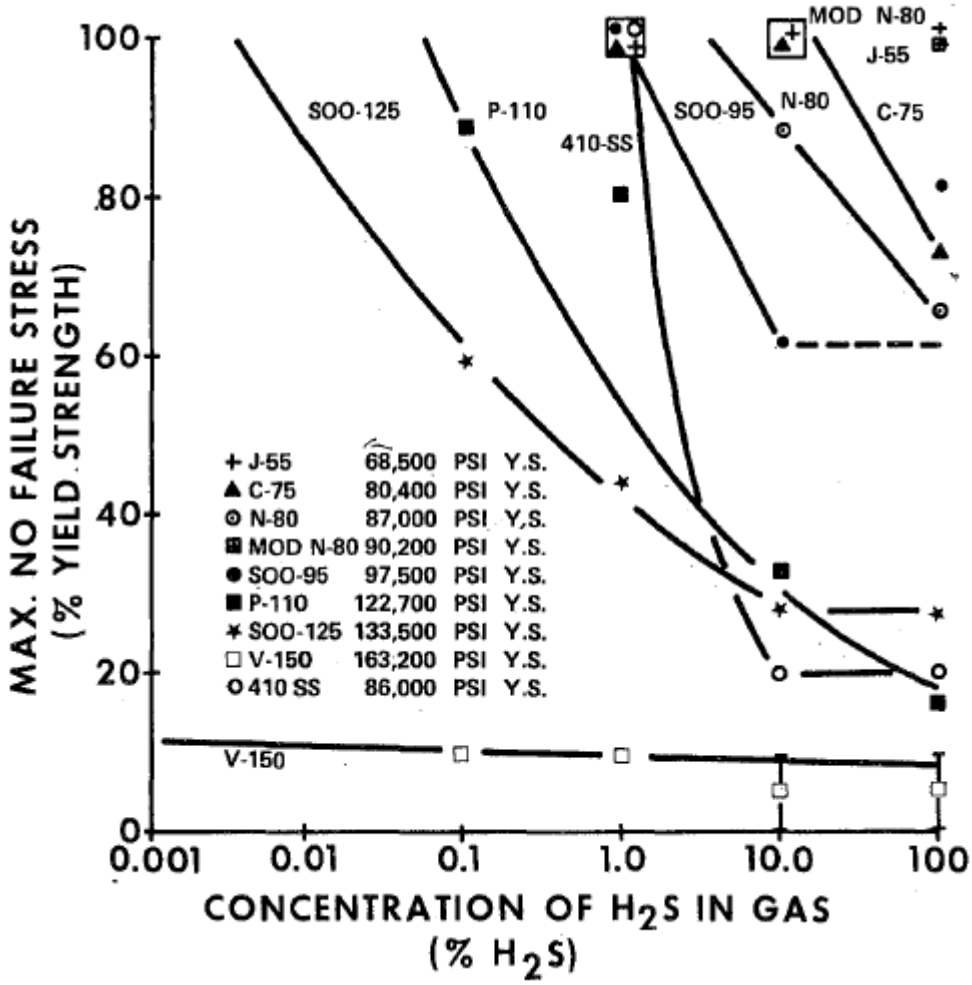

Figure 2.12: Maximum no failure stress versus hydrogen sulfide concentration for various steels [41].

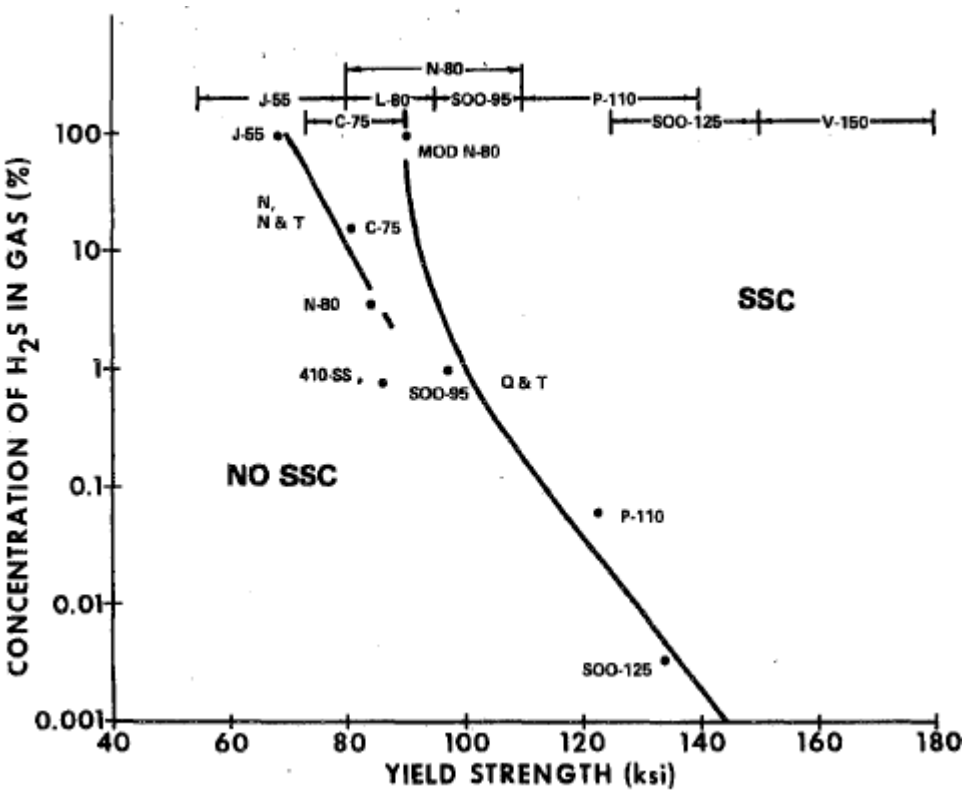

Figure 2.13: The maximum H_2S concentration limit for SSC-free behavior at 100 percent of yield strength-applied stress as a function of the yield strength of the steels [41].

The combined effects of pH and H_2S partial pressure have been studied by Omura et al. [42] and Asahi et al. [43]. Omura and his coworkers[42] tested the SSC resistance of 125ksi low alloy steels at various combinations of pH and H_2S partial pressure at ambient temperature using NACE TM0177 standard test method A with smooth round bars specimens. As seen in Figure 2.14, increasing pH and decreasing H_2S partial pressure generally decrease the SSC susceptibility. More failures are observed at pH<4 and 0.05-0.1MPa H_2S partial pressure; and the hydrogen permeation rate is found to be higher in that range. They suggested the higher cracking susceptibility was because of the increased environmental severity in terms of hydrogen ingress into the steels.

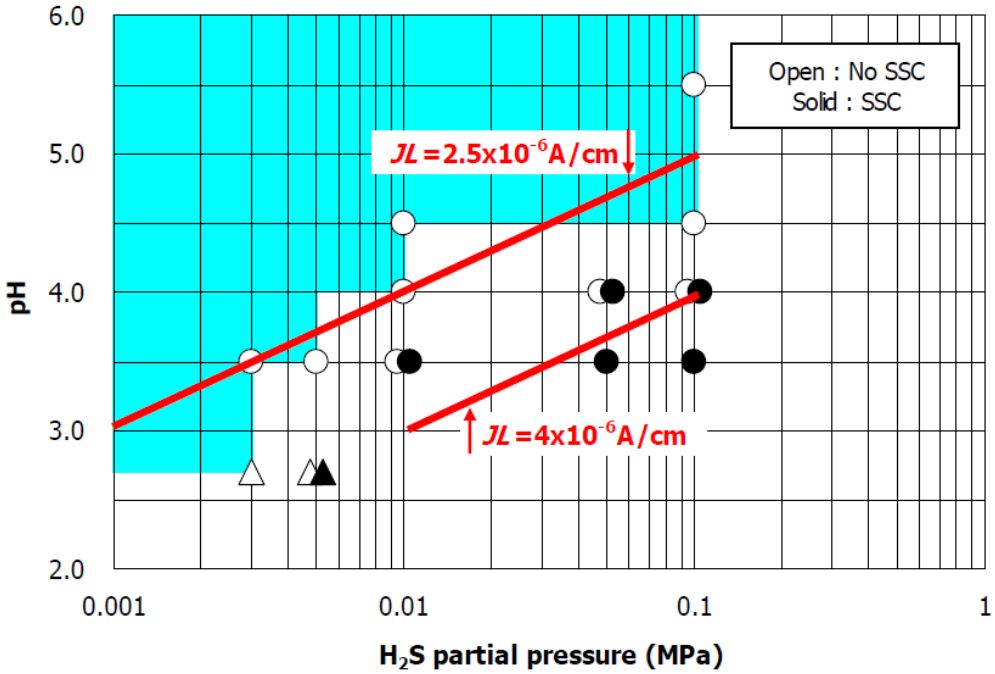

Figure 2.14: Effect of pH and H_2S partial pressure on SSC susceptibility and hydrogen permeation[42].

Asahi et al.[43] also investigated the effect of pH and H_2S partial pressure on SSC resistance of C125 grade casing steels using NACE TM0177 standard tensile test, V-notched four-point bent beam test, and SSRT test. But they found that the SSC test results were predominantly defined by the H_2S partial pressure rather than the effect of pH. They suggested the hydrogen entry at the point of failure was more dependent on hydrogen sulfide pressure. Change in one unit of pH (i.e. a tenfold change in [H+]) has the equivalent effect to a tenfold change in H_2S partial pressure for hydrogen entry into steels [43].

2.5.1.2. Effect of temperature

Sulfide stress cracking susceptibility is strongly dependent on service temperature. Many studies have reported that an increase in temperature reduces the risk of SSC failure [10, 42, 44, 45]. Ferritic and martensitic steels are reported to have more susceptibility to SSC when the service temperature is below 90 ^{o}C [44]. Kobayashi and Omura [45] have found that decreasing

testing temperature significantly increases the hydrogen uptake for low alloy steels resulting in higher cracking susceptibility. Figure 2.15 shows the effect of temperature versus SSC threshold stress for various steels. Increasing temperature increases SSC resistance in terms of threshold stress. Maximum SSC susceptibility occurs near room temperature [10].

For safe application of steels in sour service, Figure 2.16 shows the minimum temperature at which SSC failure would not occur under applied stress equivalent to 100% yield strength. The minimum temperature increases as material's yield strength increases.

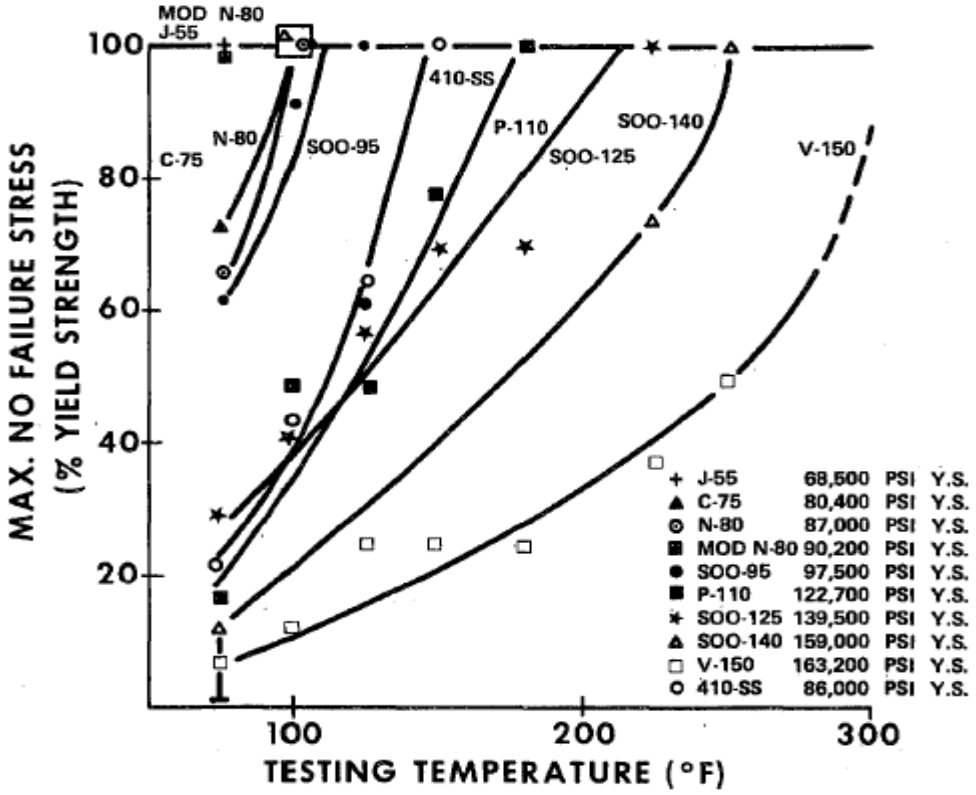

Figure 2.15: Effect of temperature on SSC threshold stress for various steels[41].

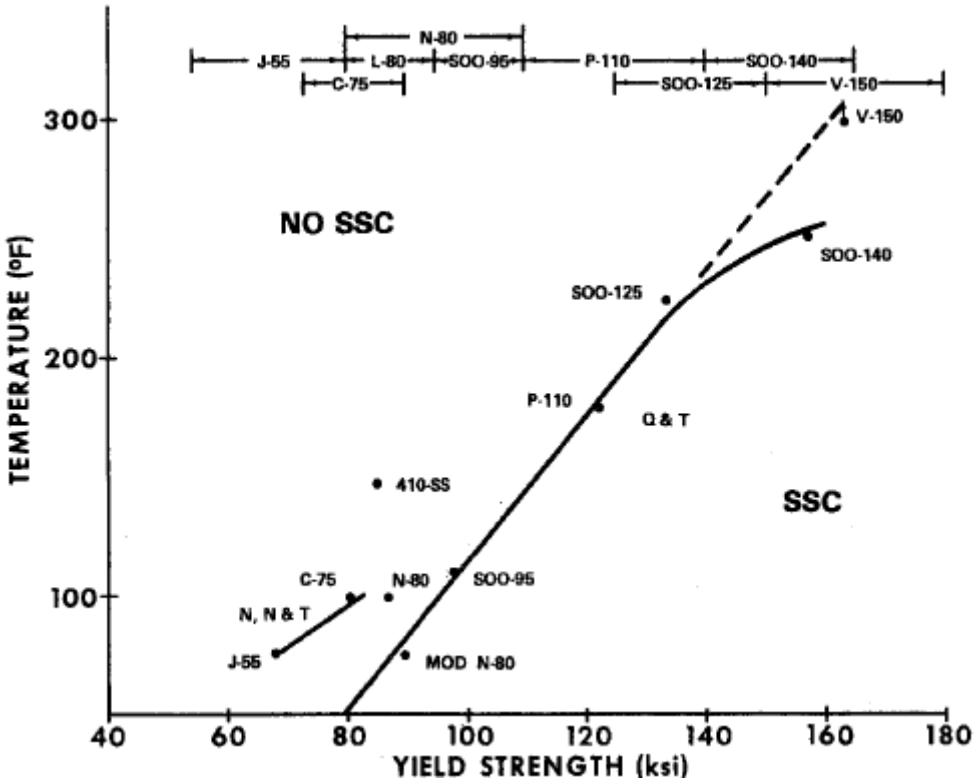

Figure 2.16: Minimum temperature for SSC-free behavior at 100% of yield-strength applied stress as a function of the yield strength of the steel[41].

2.5.2 Metallurgical factors

Understanding the effect of metallurgical variables could aid in a better design of steels for applications in sour service. SSC resistance is strongly dependent on the complex interactions of metallurgical variables in steels. It is difficult to discuss each of these factors alone, since these factors tend to have effects on each other. In this chapter, patterns of these metallurgical variables will be addressed, but it should be noted that interactions and synergistic effects of these factors on SSC susceptibility could occur.

2.5.2.1 Effect of chemical compositions

Addition of alloying elements can have several effects on the properties of steels such as improving hardenability, corrosion resistance, deformability, and machinability.

The resistance to HIC and SSC generally decrease with an increase in

carbon content [46]. This is mainly due to the effect of carbon on the microstructure and hardness. Increase in carbon content tends to increase carbon segregation and also enhances the segregation effect of manganese and phosphorus which both have adverse effects on SSC resistance (Figure 2.17). Above 1wt% manganese and 0.005wt% phosphorus increases the cracking susceptibility regardless of the carbon level [47, 48].

Increasing sulphur contents are also known to increase SSC susceptibility. This is due to the formation of more MnS stringer inclusions which provides ready crack path for crack nucleation. Calcium is usually added to modify the shape of MnS stringers into globular CaS particles.

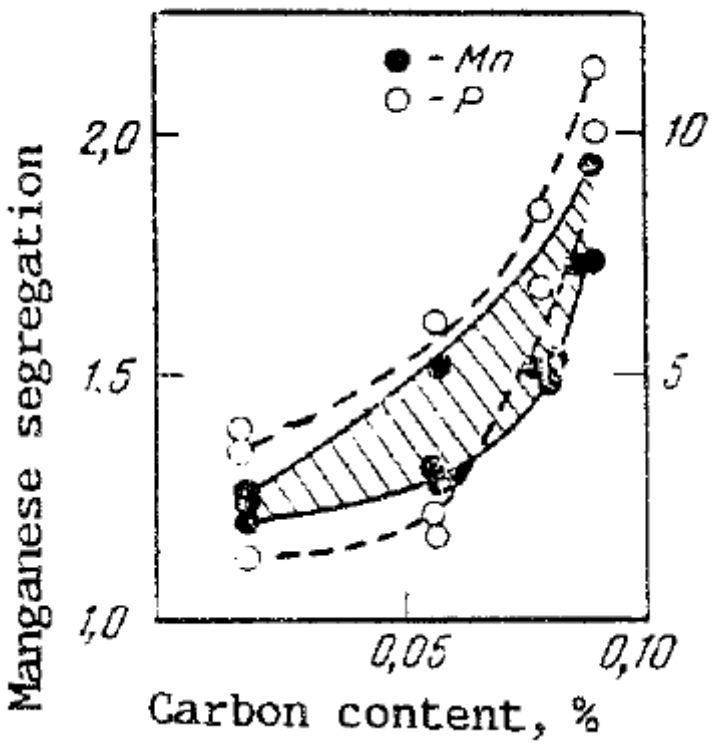

Figure 2.17: Effects of carbon content on manganese and phosphorus segregation [46].

For non-carbide forming elements such as copper, nickel, silicon, and aluminum, addition of copper and nickel reduce hydrogen uptake in the steels

and lower cracking susceptibility. Copper content above 0.2 wt% leads to a decrease in SSC susceptibility by reducing the subsurface hydrogen concentration [47, 48]. Aluminum content in the range of 0.2wt% to 0.6wt% has demonstrated improved resistance to hydrogen embrittlement in H_2S containing media, and it slows down the diffusion of hydrogen by obtaining a structure of ferrite with evenly distributed carbides [10, 47, 48]. Silicon addition above 1wt% increase cracking susceptibility for quench and temper carbon steels and 0.4-0.8wt% additions show the best resistance to hydrogen embrittlement[47, 48]. These elements are present in solid solution with iron.

For carbide forming elements such as chromium, molybdenum, titanium, vanadium, and niobium, both chromium and molybdenum have demonstrated beneficial effects on SSC. Before carbide precipitation occurs, these elements are present in solid solution with iron. Addition of Cr can improve hardenability and corrosion resistance, but high level of Cr (>0.5 wt%) result in formation of M_7C_3 and $M_{23}C_6$ carbides which is incoherent with the matrix and can lead to crack initiation from hydrogen accumulation [10, 47, 48]. Mo is an important solid solution strengthener and also plays a role in precipitation strengthening. It can significantly improve hardenability, promote development of a hard martensitic structure. Molybdenum additions up to about 0.75wt% has demonstrated to show improved SSC resistance in AISI 4130 steels (i.e. Cr-Mo low alloy steels); but above this concentration, acicular Mo_2C phase precipitates in the alloy after tempering above 500^oC, which reduces SSC resistance significantly [49]. Vanadium and niobium has been reported to have beneficial effect on grain refinement as well as formation of fine carbides. The effect of titanium is controversial. Some researchers point out titanium decreases SSC susceptibility by decreasing hydrogen permeation flux due to formation of Ti-Nb(C,N) precipitates. Others have found that presence of second phase Ti-Nb(C,N) precipitates led to SSC initiation [10, 47, 48].

2.5.2.2 Effect of mechanical properties

Strength level is one of the most important factors influencing SSC resistance. Resistance of steels to SSC decreases with increasing strength levels [2, 10]. Figure 2.18 shows threshold stress intensity versus yield strength of AISI 4340 low alloy steel in aqueous and gaseous environments containing hydrogen[49]. The threshold stress intensity for crack growth generally decreases with increasing yield strength regardless of the environments [49]. Steels with very high strength are not suitable to use in hydrogen charging environments.

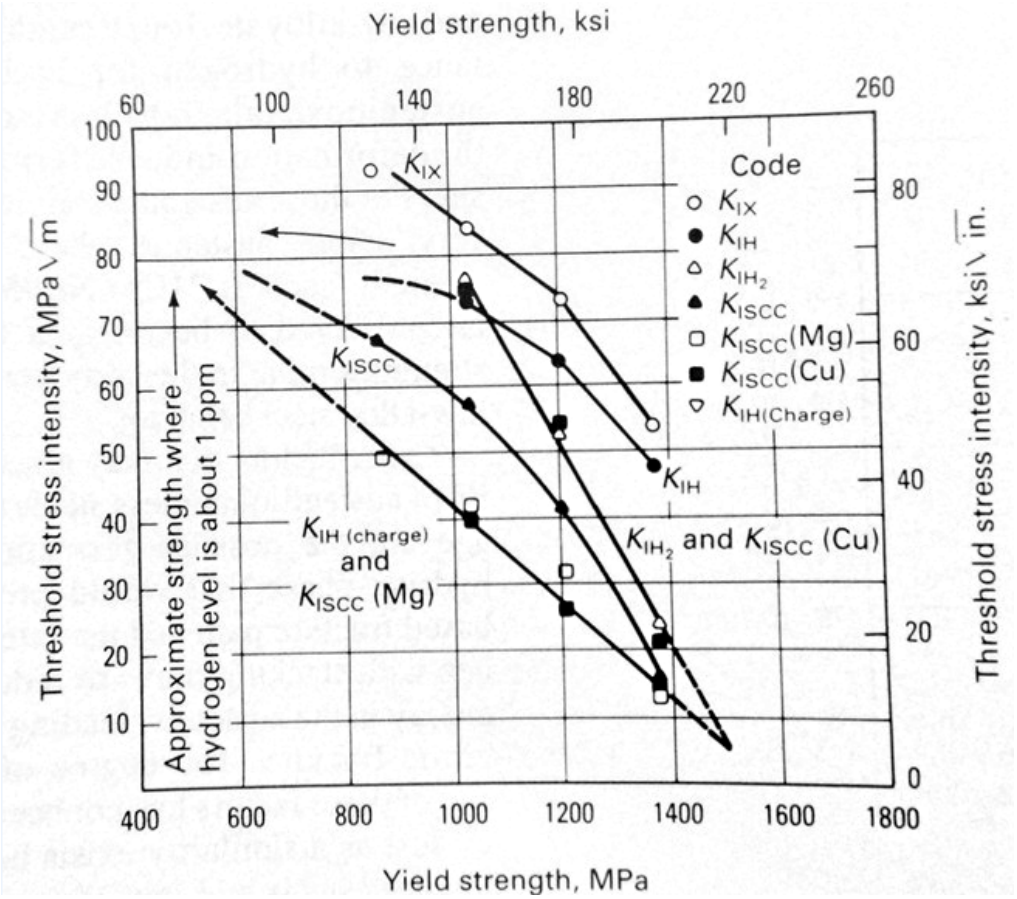

Figure 2.18: Effect of yield strength on some threshold stress intensity parameters for crack growth (i.e. fracture toughness) in a commercial AISI 4340 steel plate. K_{IX}=threshold stress intensity as a function of yield strength in air;K_{IH} is similar to K_{IX} but slowly loaded; K_{ISCC} (Mg) and K_{ISCC} (Cu) represent specimen coupled to magnesium and copper, respectively [49].

Similarly, effect of hardness on threshold stress intensity (K_{ISSC}) of Mo-Nb modified 4130 low alloy steels is shown in Figure 2.19 [50]. Increasing hardness decreases threshold stress intensity (or fracture toughness) for crack growth. Hardness of 22 HRC is usually used as a safety limit for L80 grade casing steels used for sour service to ensure safe applications, though cracking could still take place below this value.

Toughness of steels is also strongly related to HIC and SSC resistance [9, 10]. Improving toughness of steels can improve cracking resistance. Both API 5CT [12] and ERCB directive 10 [6] have minimum requirements for toughness of casing steels, as shown in Table 2.2 for L80 steels used for sour service.

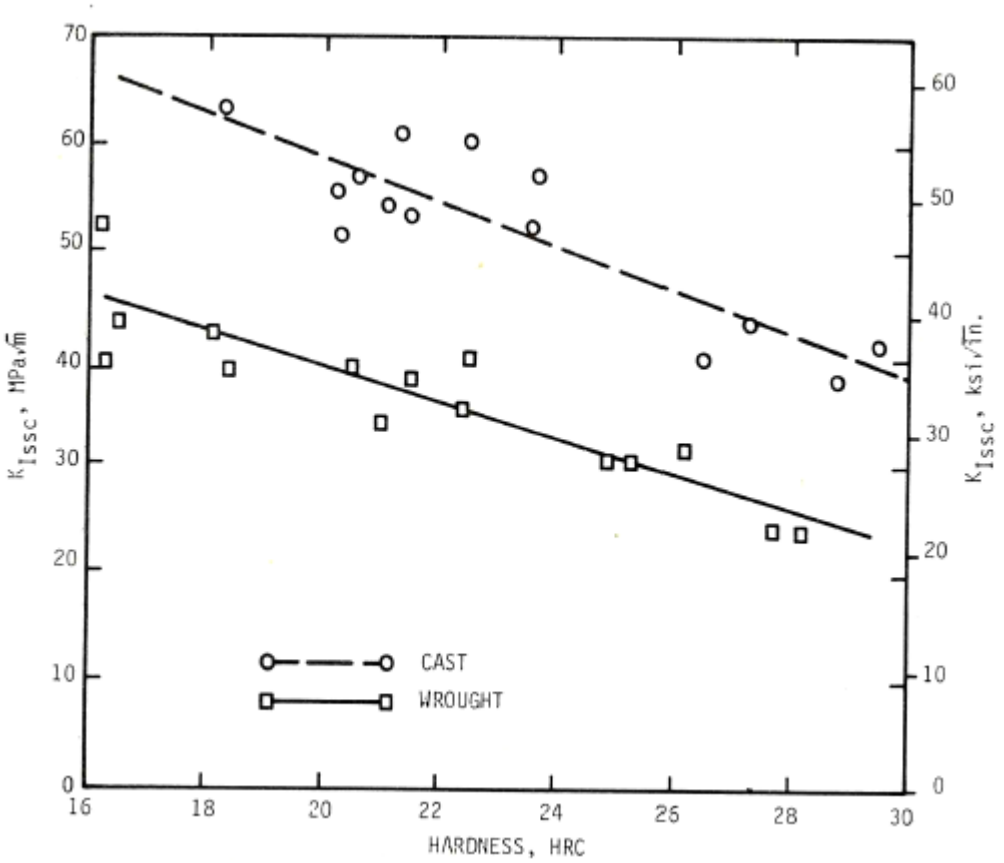

Figure 2.19: Effect of hardness on the sulfide fracture toughness, K_{ISSC} for Mo-Nb-modified 4130 steel [50].

2.5.2.3. Effect of microstructure and heat treatment

The microstructure not only has a critical role on material performance but also on SSC resistance. Because microstructure is influenced by heat treatment and alloying chemistry, these factors are difficult to separate and must be considered together.

Microstructures such as ferritic-pearlitic microstructure, upper/lower bainite, quenched and tempered martensite have been studied extensively in literature. Comparing steels at similar strength level, a quenched-and-tempered microstructure with fine grains is more resistant to cracking than a normalized or bainitic steel [49]. Ferritic-pearlitic microstructure has been shown to have the greatest susceptibility to SSC due to the presence of high number of interfaces that provide sinks for hydrogen [4]. When hydrogen accumulates to a critical value, cracking results [2]. The most resistant microstructure reported in literature is a heavily tempered martensitic structure with equiaxed ferrite grains and spheroidized carbides that distribute uniformly in the matrix [49, 50]. Acicular ferrite and ultrafine ferrite are of particular interest to steel makers recently due to their high strength and high toughness [2]. Zhao et al. [2] investigated the H_2S resistant behaviors of acicular ferrite and ultrafine ferrite and they found that both microstructures were not sensitive to HIC and SSC.

Grain size has also been reported to have an effect on SSC susceptibility. Refining the grain size has demonstrated to enhance SSC resistance, as shown in Figure 2.20 [49]. However, it has also been reported that this effect of grain size depends on fracture mode. For cleavage fracture, refining grain size would show beneficial effect. In contrast, coarsening grain size would decrease SSC resistance, for intergranular mode of fracture. If the plastic zone size or dimple rupture region is significantly larger than the grain size, no effect of grain size would be expected [50].

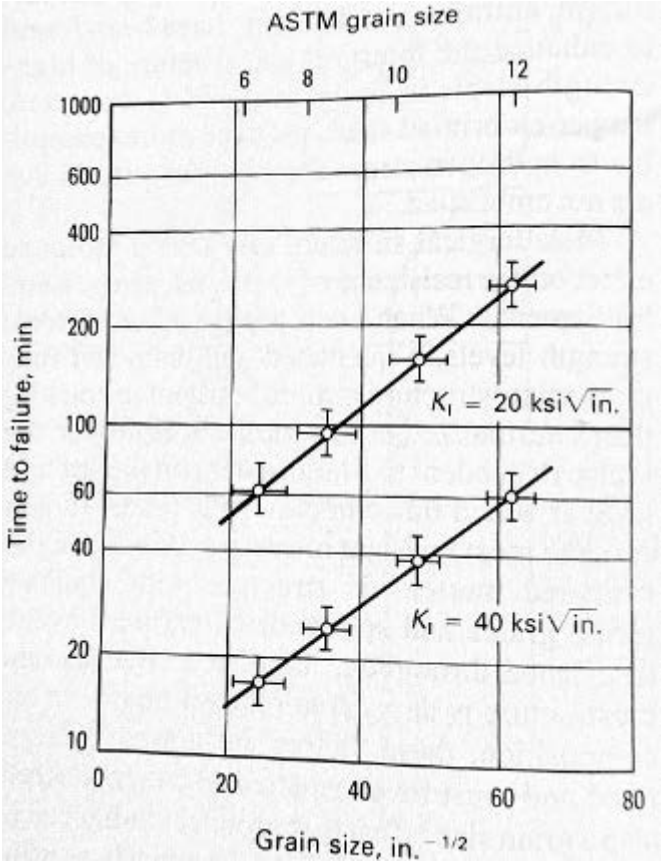

Figure 2.20: Effect of grain size of SSC resistance measured by time-to-failure of two strengths of AISI 4340 low alloy steels [49].

Quantitative studies of the effect of heat treatment on SSC resistance were performed by Snape [39], Hudgins et al. [40], and Hill et al. [51]. These studies compared SSC resistance of low alloy steels using quenched-and-tempered and normalized-and-tempered treatments. The quenching media and final microstructures of steels were not reported. However it is reasonable to assume, quenched-and-tempered steels have a fully martensitic structure after quenching. Normalizing may produce a range of microstructures such as bainite and ferrite/pearlite [50]. All of the studies confirmed that a fully quenched martensitic structure followed by heavy tempering treatments, affords the best SSC resistance[50]. Snape [39] observed that raising the tempering temperature of 0.34C-0.73Cr-0.22Mo steels from 455 to 540 ^{o}C improved the SSC threshold stress from 240MPa to 345 MPa when tested with smooth beam specimens in H_2S-saturated aqueous

solution. Hudgins et al. [40] tested N80 grade steel with C-rings specimens that were loaded to 130% yield strength in H_2S saturated environment after raising the tempering temperatures from 595 to 705 ^oC. They observed a dramatic increase in SSC resistance in terms of an increase in time to failure from 7 hour to more than 3120 hours. Similarly, Grobner et al. [52] studied the effect of molybdenum content on SSC resistance of Mo-Nb-modified 4135 steels at various tempering temperature. Both bent-beam and DCB tests show improvements on SSC resistance as measured by critical stress S_c and fracture toughness K_{ISSC} (Figure 2.21).

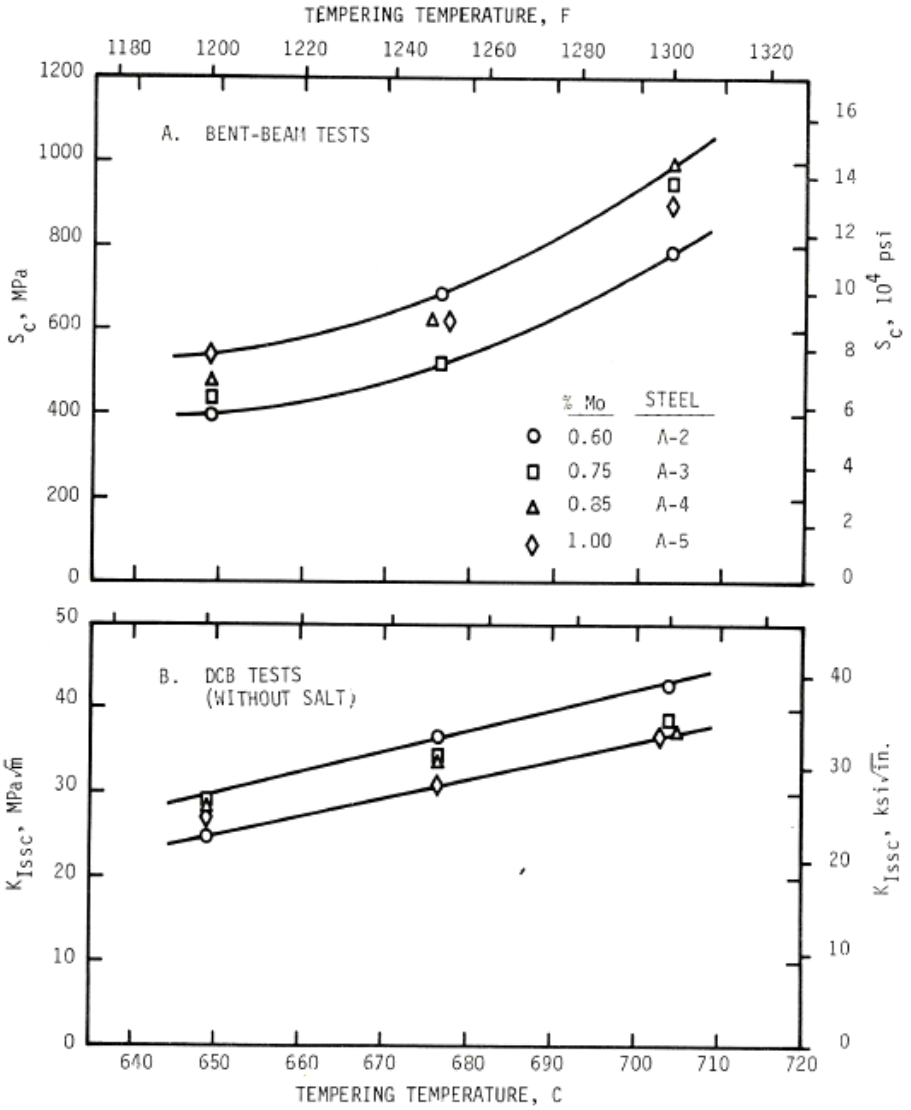

Figure 2.21: Effect of tempering temperatures of a 1-hour temper on the critical stress (S_c) and sulfide fracture toughness (K_{ISSC}) of Mo-Nb-modified 4130 steels[50].

However, tempering at too high temperatures could also degrade SSC resistance due to the formation of untempered bainite or martensite [50], as shown in Figure 2.22. Tempering at too low temperatures (370-575 ^{o}C) may hinder the steels to achieve good SSC resistance due to exposure to the danger of temper embrittlement phenomenon in that temperature range [50].

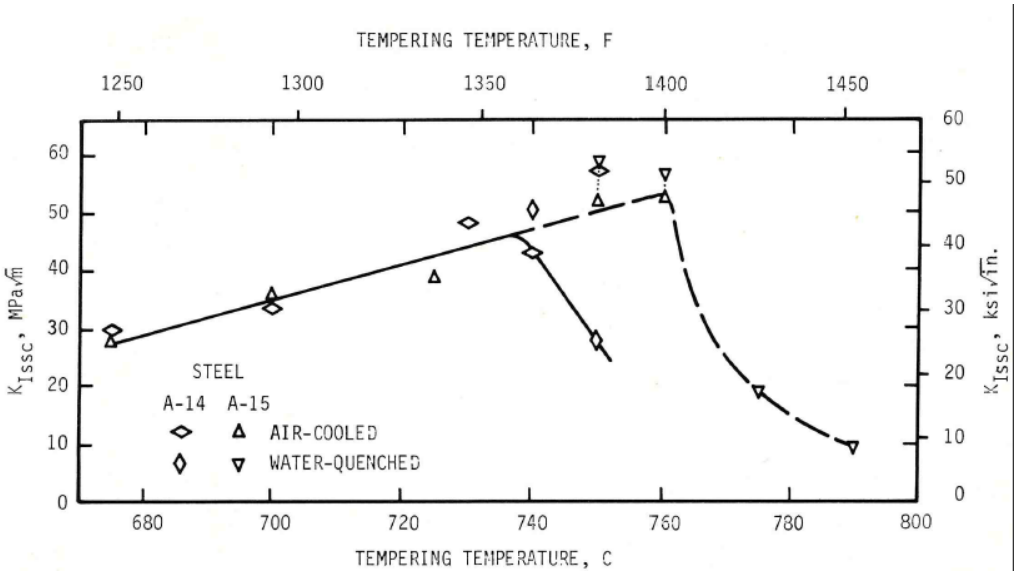

Figure 2.22: Effect of tempering temperature on sulfide fracture toughness (K_{ISSC}), of Mo-Nb-modified 4130 steels [50].

2.5.2.4 Effect of non-metallic inclusions

It is critical to control inclusions in steels because they affect not only mechanical properties of steels but also corrosion behavior and resistance to cracking.

The cracking resistance of steels is influenced largely by the volume fraction, size, distribution, composition and morphology of inclusions which usually act as stress raisers for crack initiation. Large (i.e. size > 10μm) and low deformability inclusions are reported to be particularly detrimental to steels and sometimes failure could occur by a single large inclusion or clusters of inclusions. Dangerous inclusions are usually composed of Al, Ca, and O which are hard and brittle oxide particles [53, 54].

Due to the difference in thermal expansion coefficients of the inclusions and the steel matrix during processing, stresses that arise at the interface between the inclusion and matrix make the interface an ideal location for hydrogen accumulation and crack nucleation. Elongated manganese sulfide and coarse cubic titanium nitride are usually sites for hydrogen accumulation due to their sharp edges with the steel matrix and they are reported to have detrimental effects in promoting SSC and HIC susceptibilities [9, 55, 56].

Many studies have correlated sulfur content to HIC susceptibility. It is well known that increasing sulfur content leads to an increase in HIC susceptibility due to the formation of MnS. Controlling the sulfur content to below 10ppm has been reported to enhance HIC resistance [9]. Controlling the shape of inclusions is particularly important for improving properties and cracking resistance of steels. Elongated inclusions, especially MnS, have been demonstrated to increase cracking susceptibility compared with round inclusions [56, 57]. Addition of calcium is usually used for modifying the shape of sulfide inclusions. Elongated MnS inclusions are very ductile and soft in nature during rolling while CaS are round and hard particles that do not elongate. The beneficial effect of round inclusions is that they reduce the stress risers associated with elongated inclusions [9]. Optimum Ca/S ratio has been reported to be about 2 for effective shape modification and at the same time preventing CaO formation [9].

2.5.2.5. Effect of segregation and casting practice

Segregation of impurities and alloying elements is of critical importance to cracking susceptibility. During continuous castings, segregation of one or more elements occurs. As the casting cools, the solute atoms tend to segregate to the center of the casting, resulting in a banded structure with an enriched centerline [9, 58]. Centerline segregation bands constitute a major quality problem in steels due to the non-uniform distribution of elements and mechanical properties. Since the centerline is enriched with solutes, MnS and

TiN are more likely to precipitate here as well [9, 58]. The segregation bands have low toughness and high lattice strains thus making them preferential sites for hydrogen accumulation and promoting HIC and SSC susceptibility. Centerline carbon segregation could lead to an increased pearlite portion in the center of the slab and increase cracking susceptibility [59]. Segregations of manganese and phosphorus results in a banded structure with high hardness and promote cracking susceptibility.

2.6. Topic selection and research approach

Research over recent decades has been focused on the study of SSC behaviors of low alloy steels due to their lower costs. L80 grade casing steel is most often used in sour service and it is also chosen as the testing material in this study. Increased development of deeper sour wells requires the steel to have improved SSC resistance. The L80 casing steels used in this study is newly developed low alloy steels with Ti-B, Cr-Mo, Mn-Cr alloying treatment. Cr-Mo steels have been reported to have superior performance in sour service. It has been suggested this is due to the presence of alloying carbides[9, 60]. Depending on the alloying contents, different carbide morphologies could result. But little research has been done on the effect of carbides morphology on SSC resistance. A characterization of carbide is necessary to investigate this aspect. Furthermore, limited information is available for SSC behaviors of Ti-B and Mn-Cr alloying steels in sour environment. So an assessment of these casing steels in sour environment is needed.

A number of experimental procedures have been developed for SSC assessment. Constant load tension test is one of the most widely used methods and will be used in this study. The test is a uniaxial tension test. It generates a failure/no failure result and time-to-failure data is reported. SSRT is another test used in this study. It is not a traditional test for SSC evaluation but it has attracted more attention recently because it can give a quick assessment of material performance. Little data is available for SSC evaluation using SSRT.

SSRT test will be used in this study to compare with the results from the constant load test.

This chapter has summarized the effect of environmental factors and metallurgical factors on SSC resistance for low alloy steels. The following are agreed on:

- Decrease in pH and increase in H_2S partial pressure result in a higher SSC susceptibility.
- SSC susceptibility is the highest near room temperature.
- SSC resistance decrease with increase in yield strength.
- Segregation must be minimized to improve the SSC resistance.
- The interface between inclusion and matrix are ideal locations for hydrogen accumulation and crack nucleation. Elongated or coarse inclusions must be minimized.
- Heavily tempered martensite is known to be resistant to SSC.

All these factors have an effect on SSC performance of steels, but which factor is the dominant factor/cause has not been determined. This thesis is intended to fill the information gap. So the objectives for this study include the followings:

- Evaluation of the cracking behaviors of trial compositions of casing steels with different alloying chemistries (i.e. Ti-B, Cr-Mo, Mn-Cr).
- Investigation of the effects of mechanical properties, inclusions (i.e. shape, content, and type) and carbide morphology on SSC susceptibility.

Based on the results obtained, the dominant cause/factor determining SSC performance will be discussed for L80 casing steels. Future studies will be recommended at the end of this thesis.

3. EXPERIMENTAL PROCEDURES

The following chapters describe the test materials, equipment, environments, and procedures for evaluating SSC susceptibility. As indicated in literature review, constant load tension test and SSRT will be used. Techniques for examination of microstructures and fracture surfaces will be described in Chapter 3.2 and 3.3. Techniques for characterization of inclusions and carbides will be addressed in Chapter 3.4 and 3.5, respectively.

3.1 Test Materials

Seven different low alloy casing steels supplied by Evraz Inc. NA have been investigated in this study. These include six quenched-and-tempered steels and one as-rolled microalloyed steel. The materials were received in the form of pipe samples. The processing and alloying strategy of the casing steels is shown in Figure 3.1. The quench-and-temper steels can be divided into two main groups with different alloying strategies. One group is alloyed with titanium-boron (Ti-B); the other is alloyed with manganese-chromium-molybdenum (Mn-Cr-Mo). The Mn-Cr-Mo group can be subdivided into Mn-Cr alloying and Cr-Mo alloying. The main chemical compositions of the steels tested are given in Table 3.1.

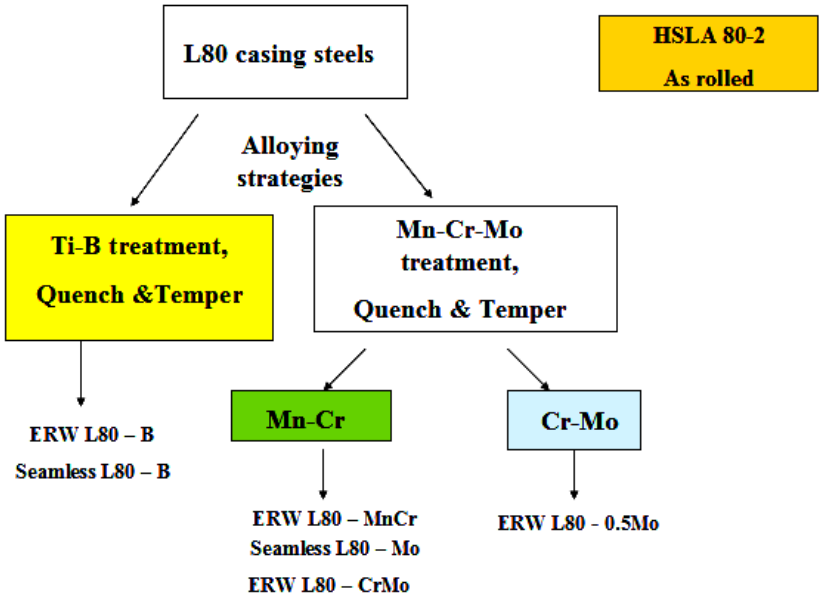

Figure 3.1: The processing and alloying strategy of the casing steels.

Table 3.1: Chemical composition (wt%) of casing steels tested.

	C	Mn	P	S	Si	Cr	Mo	Other
ERW L80 – B	0.24	0.98	0.007	0.0016	0.24	0.15	0.02	Ca, Ti, B
Seamless L80 – B	0.25	1.13	0.014	0.0100	0.23	0.42	0.04	Ca, Ti, B
ERW L80 – MnCr	0.25	1.34	0.007	0.0008	0.21	0.46	0.01	Ca
Seamless L80 – Mo	0.28	1.10	0.010	0.0040	0.24	0.20	0.06	Ca
ERW L80 – CrMo	0.24	1.12	0.012	0.0008	0.27	0.33	0.12	Ca
ERW L80 - 0.5Mo	0.25	0.69	0.007	0.0011	0.19	0.25	0.49	Ca
HSLA 80 -2	0.18	1.33	0.010	0.0026	0.20	0.06	0.07	Ca, Nb, Ti, V

3.2 Microstructure examinations

The as received specimens were mounted in epoxy resin (Buehler, part # 208128). Before viewing the microstructure under the Scanning Electron Microscope (SEM), the following procedures were performed:

- Wet grounded the specimens from 200 grit to 1200 grit finish with silicon carbide paper (supplier: Buehler, part # 30-5308).
- Cleaned and swabbed the specimens with ethyl alcohol followed by drying in warm air.
- Polished the specimens with 1µm diamond suspension (supplier: Buehler, part # 40-6530).
- Repeated cleaning step with ethyl alcohol and dried in warm air
- Polished the specimens with 0.05µm alumina suspension (supplier:

Buehler, part # 40-6377-032).

- Repeated cleaning step with ethyl alcohol and dried in warm air
- Etched the specimens with 2% Nital solution (2mL nitric acid+98mL ethyl alcohol) at room temperature until the surface appeared to be a light gray color (usually in about 6-8 seconds).
- Cleaned with water followed by cleaning with ethyl alcohol and drying in warm air.

For examining the microstructure, a Hitachi S-2700 Scanning Electron Microscope (SEM) equipped with a PGT (Princeton Gamma-Tech) IMIX digital imaging system and a PGT PRISM IG (Intrinsic Germanium) detector for Energy Dispersive X-Ray Analysis were used. Accelerating voltage used was 20kV, and working distance was 17mm. Magnifications of 100x, 500x, 1500x and 5000x were used and images were taken.

3.3 Cracking susceptibility tests

3.3.1 Constant load SSC test

NACE TM0177-2005 [18] standard test method A was used as one of the test methods to evaluate the SSC susceptibility of the steels. Method A is a constant load tensile test in an acidified, hydrogen sulfide saturated aqueous brine solution. A proof ring testing device supplied and calibrated by Cortest Inc. is used for NACE standard method A. Figure 3.2 shows a photograph of the Cortest proof ring device.

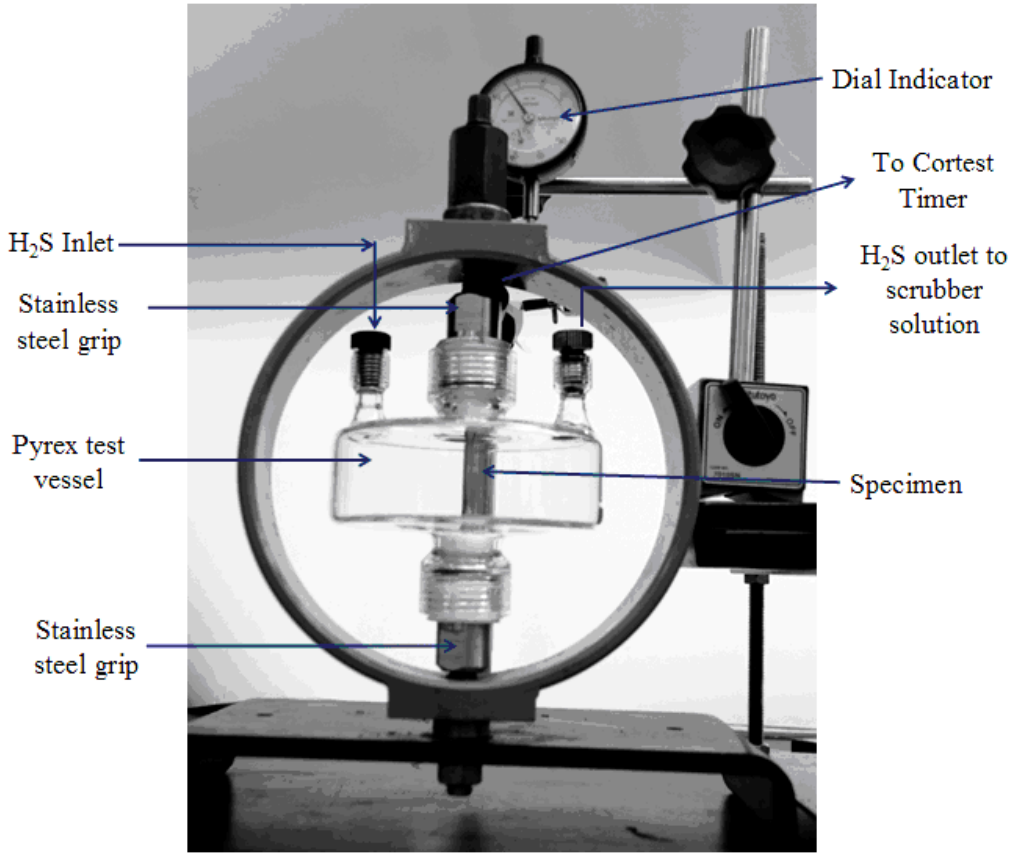

Figure 3.2: Cortest proof ring testing device.

Each individually calibrated proof ring (accuracy: ±1%) is accompanied by a conversion chart which is used to determine the applied load from the deflection of the ring. The calibration chart is shown in Appendix A. The tensile specimen is loaded under uniaxial tension which can be easily adjusted using a 30.5 cm (i.e. 12'') adjustable wrench on the tension-adjusting screw and lock nut. The applied stress is determined based on the nominal specified minimum yield strength (SMYS) for casing and tubing given in the API-5CT specification for L80 steel. For this test, 85% of SMYS (i.e. equivalent to 73-80% of Actual Yield Strength for as-received materials) was used for all the specimens. The applied stress was then converted to applied load using the following equation[18]:

$$P = S \times A \qquad 3\text{-}1$$

Where:

P=desired applied load (N)

S=applied stress (MPa)

A=actual cross sectional area of the gauge section of the specimen (mm^2)

The required deflection of the ring for a desired applied load was determined from the calibration chart of the proof ring and measured accurately using a Mitutoyo dial indicator (accuracy:±0.01mm) on the ring when loading. The corresponding time-to-failure was recorded by a Cortest Timer attached to the proof ring.

The specimen grips were made of stainless steel in order to be fully resistant to the test environment. Pyrex glass environmental chamber was used in the test to permit visual observation of the specimens at all times and was secured by o-rings seals (with diameter: 1.27cm (0.5") OD, 0.635 cm(0.25")ID and 3.18cm (1.25")OD, 2.54cm (1")ID) to prevent any leakage during testing.

NACE TM0177 standard method A gives a failure/no failure result and time-to-failure data is measured. For all materials, failure is either a complete separation of tensile specimen in the solution or observation of cracks on the gauge section of the specimen at 10X using Leica DMILM optical microscope after 720 hours test duration [18]. However, evaluation based solely on time to failure has shown in literature to have more experimental scatter [61].

SSC is a type of hydrogen embrittlement, and is manifest by a loss in ductility. With respect to the stress-strain curve of a material, measures of ductility are the total plastic strain and reduction of area (RA) at fracture. The ratio of ductility in H_2S environment to that in an inert environment may be a more meaningful criterion for evaluation of SSC susceptibility than only the measure of ductility in H_2S environment. The ratio of reduction in area (RAR) is defined as follows:

$$RAR=RA \text{ in } H_2S/RA \text{ in air} \qquad 3\text{-}2$$

After the specimen failed in the test environment, the specimen was taken out of the environment immediately and cleaned with ethanol in an ultrasonic cleaner for 45 minutes. The specimen was then dried with compressed air and

prepared for examination in SEM. The diameter of the specimen was measured using the measuring tool in SEM (accuracy: ±2%) and then the reduction of area of the specimen is determined. For the specimen that passed the test after 720 hour test duration, it was removed from the test environment immediately. It was cleaned with ethanol in an ultrasonic cleaner for 45 minutes and dried with compressed air. After that, it was pulled to failure in air using the proof ring device. The RA was then determined using the measuring tool in SEM.

For determining the RA in air, the specimen was loaded on the ring in air for the same test duration as in solution and then stressed to failure using the Cortest proof ring.

3.3.2 SSRT Test

SSRT test was also used for evaluation of SSC cracking resistance. The SSRT test involves applying a constant strain rate to the specimen while it is exposed to the same sour environment as in the constant load tensile test until the specimen fractured. The major advantage of this test is that it can provide rapid results for evaluation. The ASTM G129 standard [33] recommends using strain rate between 10^{-4}/s and 10^{-7}/s for running SSRT. A strain rate of $8.9x10^{-7}$/s was chosen for the test. The specimens were immersed in the test environment for 24 hours before straining to allow enough time for hydrogen diffusion.

Model TTS-25kN low speed material testing machine from Adelaide Testing Machines (ATM) Inc. was used for SSRT**.** Figure 3.3 shows the schematic diagram of experimental set-up. It consists of a load frame, a drive mechanism, 25kN load cell, an environmental test vessel, two stainless steel tensile grips specifically designed for the specimens, and computer control system with TC-100 testing software which is a standard package included with the TTS-25kN testing machine. According to the vendor, the accuracy of measurement with the machine is based on the 12 bit accuracy of A/D board

that used to measure the voltage level signals from the load cell. The input range of the A/D board is ±10 VDC which is the approximate signal output of the load cell. The positioning accuracy is ±0.00041 μm for slow speed tests. The TC-100 testing software supplied by the vendor allows the setting of all test parameters (e.g. testing speed, data sampling rate, specimen information etc), stroke control (crosshead movement) and data acquisition. The testing machine is able to handle the required slow strain rate. The load versus displacement curve was displayed on the computer throughout the test. Time to failure, RAR, and fracture stress were determined from the resulting curve.

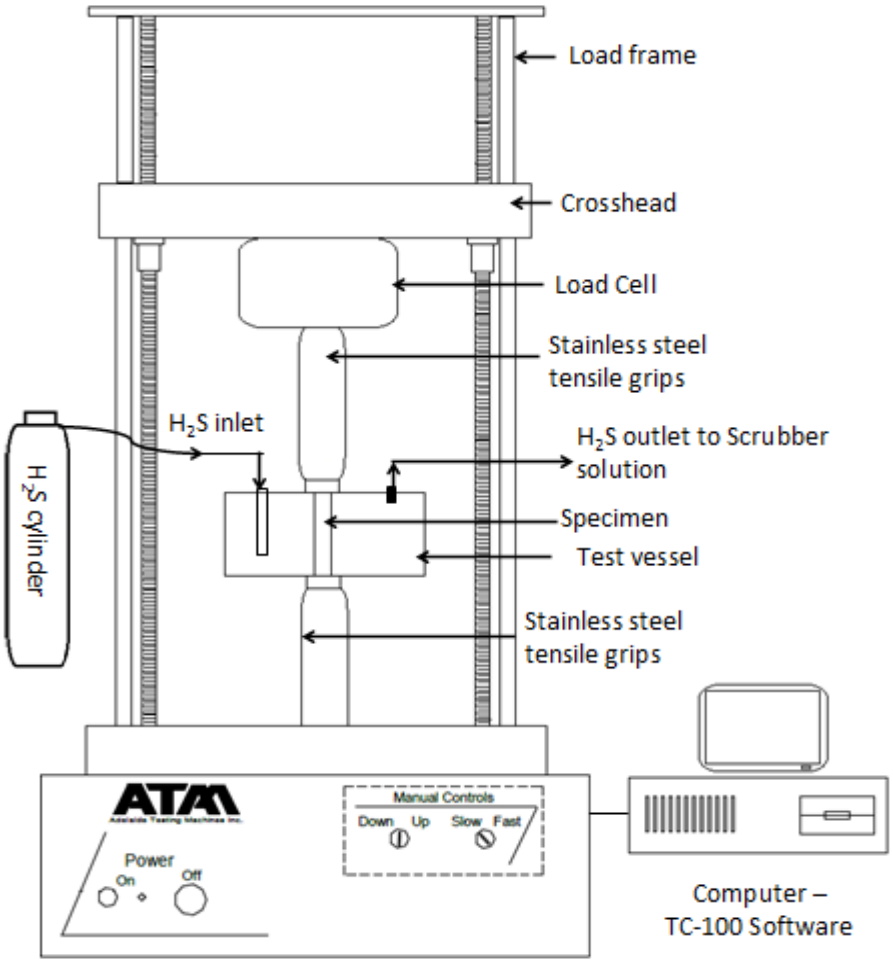

Figure 3.3: Schematic diagram of experimental set-up for SSRT.

3.3.3 Specimen preparation

Smooth round bar tensile specimens with gauge diameter of 3.81mm were machined from the mid-thickness of the casing materials (as indicated by the arrow in Figure 3.4). It was taken from the 90 degree location from the weld seam or 0 degree location for seamless steels. Figure 3.5 shows the dimension of a specimen used for both constant load tensile test and SSRT test. NACE TM0177-2005 standard requires the final surface finish to be 0.81 μm or finer. The specimen used in both tests has a final surface finish of 0.254 μm. Figure 3.6 is a picture of the machined tensile specimen. All specimens were machined according to the requirements described in the NACE TM0177-2005 standard.

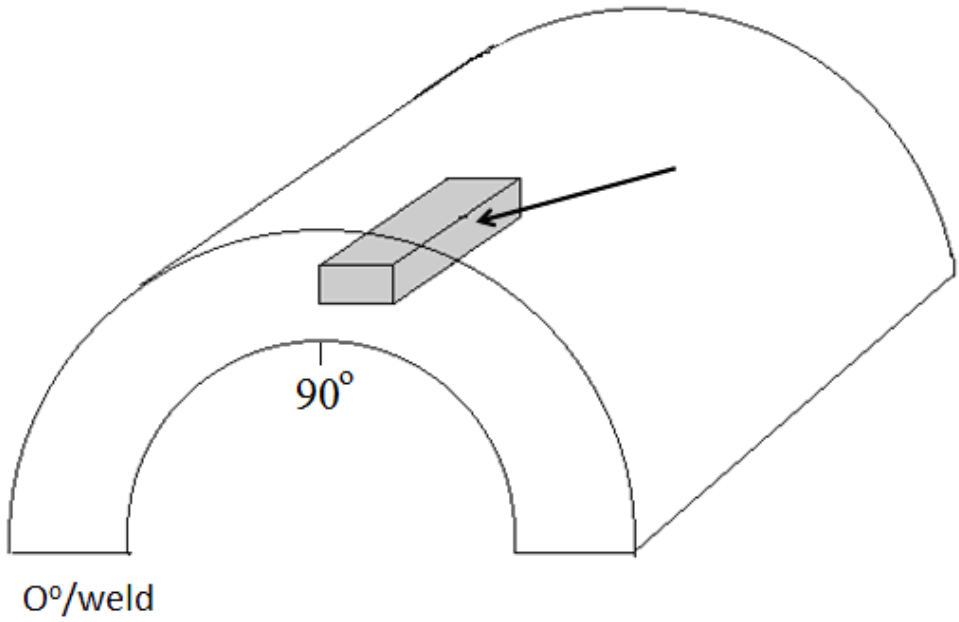

Figure 3.4: Schematic diagram of the cutting location for a specimen. The specimen was cut from the mid-thickness of the pipe wall.

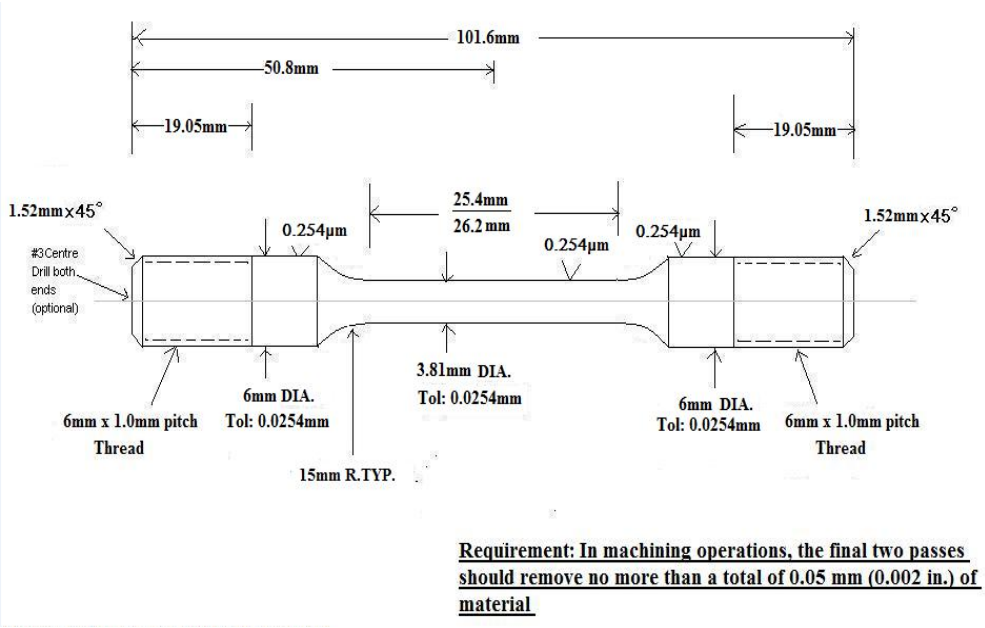

Figure 3.5: Dimensions of specimens for constant load SSC and SSRT tests.

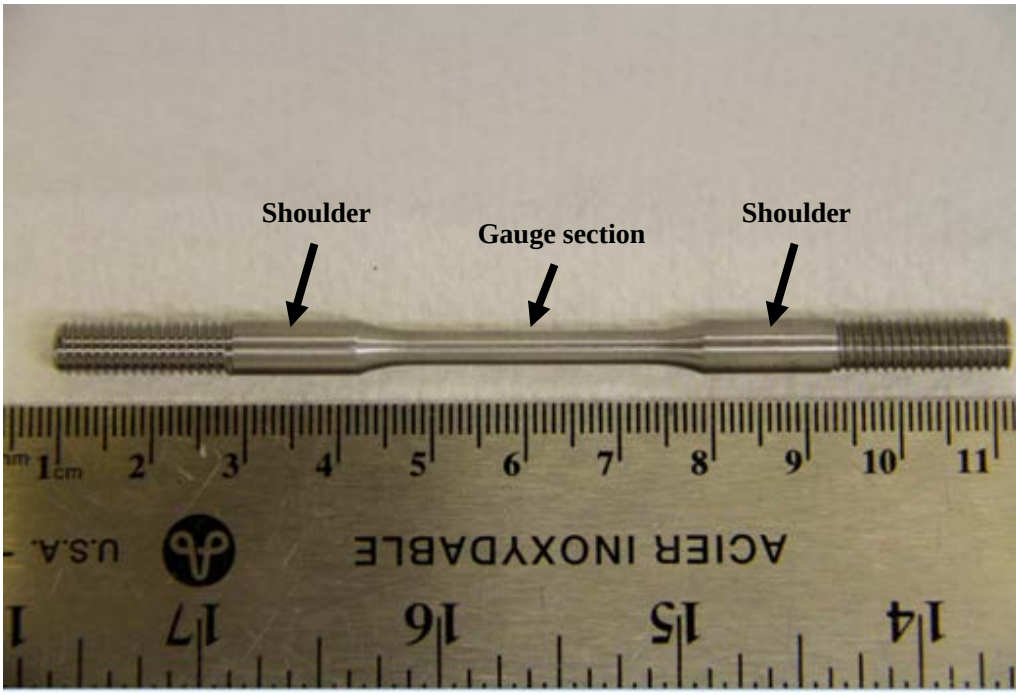

Figure 3.6: Tensile specimen used in proof ring test and SSRT test.

3.3.4. Test environment

NACE TM0177 standard solution “A” was used in both constant load tensile tests and SSRT tests. It consisted of 5.0 wt% sodium chloride (NaCl) and 0.5wt% glacial acetic acid (CH_3COOH) dissolved in distilled water,

saturated with H_2S [18]. The hydrogen sulfide gas (Praxair, 100% purity), NaCl (Fisher Scientific, 99.99% purity) and CH_3COOH (Fisher Scientific, 99.8% purity) were all reagent grades. The pH of the solution before H_2S saturation should be between 2.6 and 2.8, and increase but not exceed 4.0 during the test. A fresh solution (about 500mL) was used for each test. The initial and final pH values of the solution were measured for each test. All tests were conducted at room temperature. Inert gas (nitrogen 99.998% purity) was used for removal of oxygen in the solution at the beginning of the test.

About 2 litre, 25% sodium hydroxide solution was prepared and used as a scrubber solution to neutralize the outlet H_2S gas from both tests before venting to air in the fume hood (as indicated in Figure 3.2 and 3.3 for H_2S outlet). The scrubber solution was replaced when its color turned yellow.

3.3.5 Hardness measurement

A requirement of measuring the hardness of the test material in either HRB or HRC is included in the new edition of the NACE TM 0177 standard. Wilson Rockwell B hardness tester with 100kgf load was used to measure the hardness by taking three locations around the shoulder (as indicated in Figure 3.6) of the cylindrical tensile specimen (i.e. every 120^o). The hardness (HRB) data is then correlated with the results obtained from SSC tests.

3.3.6 Test procedures

Constant load tensile test procedure was carried out as follows, with respect to the photograph of proof ring in Figure 3.2:

- Test solution A was prepared and de-aerated according to the NACE TM 0177-2005 standard.
- The minimum gauge diameter of the test specimen was measured by a digital micrometer (accuracy:$\pm$0.002mm). The applied load was calculated from the desired stress using Equation 3-1. The corresponding ring deflection required to obtain the desired load was determined from

the proof ring calibration chart (as shown in Appendix A).

- The test specimen was cleaned ultrasonically in ethanol for 45 minutes and placed and sealed in the Pyrex test vessel.
- Stainless steel specimen grips were tightened to the test specimen and then threaded on the stud of the ring assembly and the loading bolt. At least half of the threads were engaged.
- The dial indicator was adjusted to stand perpendicularly to the top of ring surface. The reading on the dial indicator was set to zero when the proof ring was unloaded at this time.
- The ring was deflected to the desired value by turning the loading nut using a 30.5cm (12'') adjustable wrench.
- The Pyrex test vessel was filled with the prepared de-aerated test solution to immerse the whole gauge section of the specimen.
- The test solution was purged with pure nitrogen to remove oxygen before introducing H_2S.
- The test solution was then saturated with H_2S. A continuous flow of H_2S at a low flow rate (one or two bubbles per second) was maintained throughout the duration of the test to ensure H_2S saturation and a slightly positive pressure to prevent air entering the test vessel. (Note: the whole test was conducted in a well-ventilated fume hood). The pH of the test solution was measured before and after the test.
- The Cortest Timer was connected to the proof ring to record the test duration. Termination of the test shall be at specimen fracture in solution or after 720 hours test period.
- Specimen was removed from the test cell immediately after it failed. It was cleaned ultrasonically with ethanol and dried then stored in the desiccator until further examination.

For testing in air, the specimen was loaded on the proof ring in air (without the Pyrex test vessel) using the same procedure for 720 hours. After 720 hours, the specimen was then pulled to failure.

Schematic diagram for SSRT is shown in Figure 3.3. SSRT test procedure was carried out as follows:

- Test solution A was prepared and de-aerated according to NACE TM 0177-2005 standard.
- The minimum gauge diameter of the test specimen was measured by a digital micrometer (accuracy:±0.002mm). The test specimen was cleaned ultrasonically in ethanol for 45 minutes and placed and sealed in the test vessel.
- Stainless steel specimen grips were tightened to the test specimen and then threaded on the bottom of the SSRT testing machine and the load cell.
- The operating condition (i.e. specimen name, specimen dimensions and description, test number, data sampling rate and output data recording etc.) was input into the TC-100 software.
- The test specimen was preloaded for 10N by setting the preload function in the TC-100 software to ensure the specimen was aligned and under uni-axial tension.
- De-aerated test solution was added to the test vessel to immerse the whole gauge section of the specimen.
- The test solution was purged with pure nitrogen to remove oxygen before introducing H_2S.
- The test solution was then saturated with H_2S. A continuous flow of H_2S at a low flow rate (one or two bubbles per second) was maintained throughout the duration of the test to ensure H_2S saturation and a slightly positive pressure to prevent air entering the test vessel. (Note: the whole test was conducted in a well-ventilated fume hood). The pH of the test solution was measured before and after the test.
- The test specimen was immersed in the H_2S environment for 24 hours before straining to allow time for hydrogen diffusion.
- SSRT test was started by setting a strain rate of 8.9×10^{-7}/s in the TC-100

software. When the test specimen failed, the system would detect the failure and stopped the data acquisition.

- After the specimen failed, it was removed from the testing assembly immediately and cleaned ultrasonically with ethanol and dried. Specimen was then stored properly in the desiccator until further examination.

For testing in air, the specimen was loaded on the SSRT machine in air (without the test vessel) at the same strain rate ($8.9x10^{-7}$/s) until the specimen fractured.

3.3.7 Fracture surface examination

The fracture surfaces of all tensile specimens from both SSC tests were examined with a Hitachi S-2700 Scanning Electron Microscope equipped with a PGT (Princeton Gamma-Tech) IMIX digital imaging system, a PGT PRISM IG (Intrinsic Germanium) detector for Energy Dispersive X-Ray analysis. Accelerating voltage is 20kV, and working distance is 17mm. The main features examined included mode of fracture, crack initiation site, the presence of secondary cracking and the identification of HIC and SSC cracks. Magnifications of 25X to 3000X were used for examination and fractography images were taken. Crack initiation was mainly viewed at 25X, the fracture mode was viewed using 400 to 700X magnifications, and crack identification was viewed at 3000X.

3.4 Characterization of non-metallic inclusions

Microscopic test methods in ASTM E45-2005 standard and JIS G0555-2003 standard are used to characterize inclusions. Only inclusions that form as a result of deoxidation or due to limited solubility in solid steel (indigenous inclusions) were considered [62, 63]. These inclusions are characterized by their size, shape, concentration but not chemical composition. However, both standards placed the inclusions into four composition-related categories (i.e. sulfides, alumina, silicates, oxides). These are the most

common types of inclusions that considered in these methods. The following chapters will address the methods for quantification of inclusions.

3.4.1. Specimen preparation

The cleanliness of the specimens was examined on as-polished surfaces. Metallographic specimens with 160mm^2 test area were prepared and polished. Polishing procedure was the same as described in Chapter 3.2 but without etching. The specimens were cut parallel to the longitudinal axis of the tube (Figure 3.7) according to the requirements in ASTM E45-2005 standard and JIS G0555-2003.

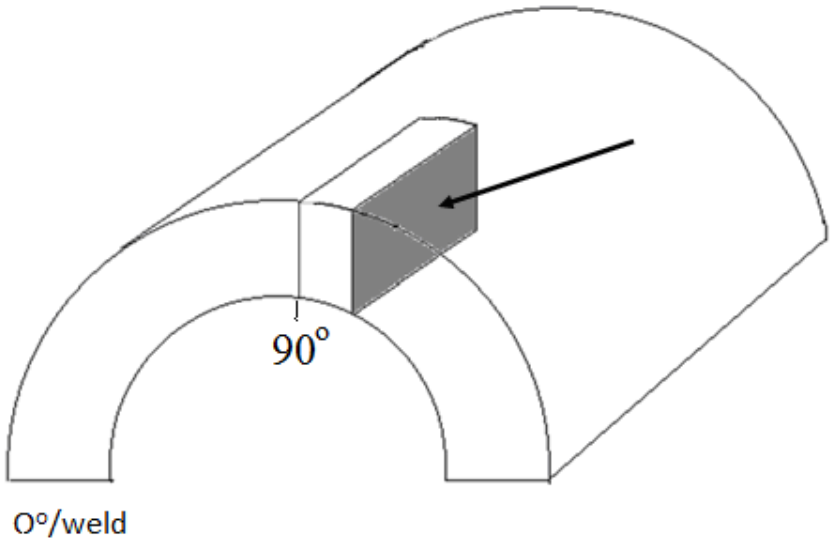

Figure 3.7: The cutting location of specimens for cleanliness examination. The specimen was cut through thickness of the pipe at a location of 90 degree from the weld seam (or 0 degree for seamless pipe).

3.4.2 Examination techniques

Quantitative assessments of inclusion were examined using two microscopic methods, namely SEM equipped with EDX, and OM equipped with Clemex CIR (Computerized Inclusion Rating) 5.0 software. The quantification using Clemex CIR 5.0 software was carried out in the Research and Development center in Evraz Inc NA, Regina. Results obtained from these

two techniques will be compared.

For SEM examination, the same Hitachi S-2700 Scanning Electron Microscope equipped with a PGT (Princeton Gamma-Tech) IMIX digital imaging system, a PGT PRISM IG (Intrinsic Germanium) detector for Energy Dispersive X-Ray analysis, and a Backscattered Electron Detector-GW Electronics System 47 four quadrant solid state detector were used.

SEM-EDX method was based on the evaluation criteria described in ASTM E45-2005 standard. This standard is used to determine the severity level of four types inclusions (i.e. sulfides, alumina, silicate, and oxides) based on inclusion density (mm/mm^2 or $count/mm^2$ for oxides) at a specific magnification, or inclusion length (mm)/count at 100X magnification. The severity level was calculated based on the limits of inclusion density given in Table 3.2 [62]. These severity values are the minimum values for each inclusion type and are rounded down to the nearest whole or half units as specified by the standard.

According to ASTM E45-2005 standard, at least six random fields on the polished specimen are required for microscopic examination on cleanliness. In this study, ten rectangular fields with an area of 0.5 mm^2 were selected randomly on the surface of the specimen. Each 0.5 mm^2 field was examined by SEM and EDX at 2500x magnification in area of 50μmx50μm. This technique is illustrated in Figure 3.8. The size, density, and shape of inclusions were recorded manually after examination for all ten fields. Then severity level was then determined using Table 3.2. This method is very time consuming, so only Seamless L80-Mo and ERW L80-0.5 Mo steel were examined with this method.

Table 3.2: Minimum values for severity levels [62].

(mm/mm^2(in./in.^{2}), or count/mm^2)				
Severity	Sulfide	Alumina	Silicate	Oxides
0.5	0.074(1.88)	0.034(.864)	0.036(.914)	2
1.0	0.254(6.45)	0.154(3.91)	0.152(3.86)	8
1.5	0.522(3.64)	0.368(9.35)	0.352(8.94)	18
2.0	0.872(22.15)	0.686(17.32)	0.640(16.26)	32
2.5	1.298(32.97)	1.110(28.19)	1.020(25.91)	50
3.0	1.796(45.59)	1.644(41.76)	1.492(37.90)	72
3.5	2.362(59.99)	2.294(58.27)	2.058(52.27)	98
4.0	2.996(76.10)	3.060(77.7272)	2.718(69.04)	128
4.5	3.796(96.42)	3.946(100.2)	3.474(88.24)	162
5.0	4.460(113.3)	4.952(125.8)	4.326(109.9)	200
(mm (in.) at 100×, or count)				
Severity	Sulfide	Alumina	Silicate	Oxides
0.5	3.7(0.15)	1.7(0.07)	1.8(0.07)	1
1.0	12.7(0.50)	7.7(0.30)	7.6(0.30)	4
1.5	26.1(1.03)	18.4(0.72)	17.6(0.69)	9
2.0	43.6(1.72)	34.3(1.35)	32.0(1.26)	16
2.5	64.9(2.56)	55.5(2.19)	51.0(2.01)	25
3.0	89.8(3.54)	82.2(3.24)	74.6(2.94)	36
3.5	118.1(4.65)	114.7(4.52)	102.9(4.05)	49
4.0	149.8(5.90)	153.0(6.02)	135.9(5.35)	64
4.5	189.8(7.47)	197.3(7.77)	173.7(6.84)	81
5.0	223.0(8.78)	247.6(9.75)	216.3(8.52)	100

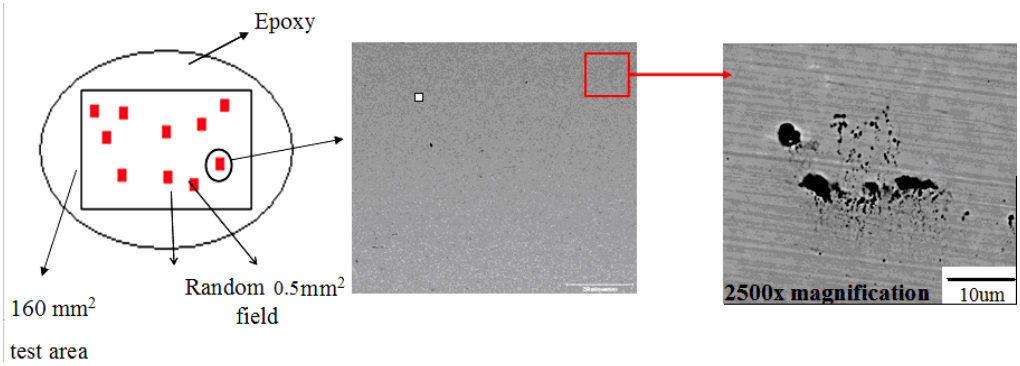

Figure 3.8: Illustration of inclusion quantification using SEM equipped with EDX.

Quantification using OM equipped with Clemex CIR 5.0 software were carried out for all steels, because the Clemex CIR software can automatically analyze the cleanliness of steels in a short time in compliance with ASTM E45-2005 and JIS G0555-2003 standard. As described earlier, the ASTM

E45-2005 is used to determine the severity level based on inclusion density or inclusion length or count at 100X magnification. JIS G0555-2003 standard is used to determine the area fraction (%) of inclusions. In addition to the inclusion types (i.e.sulfide, alumina, silicate, and oxides), the inclusions were subdivided into thin and thick series according to the thickness or width of inclusions (Table 3.3)

Table 3.3: Inclusion width or diameter parameter [62].

Inclusion Type	Thin Series		Heavy Series	
	Width, min, µm	Width, max, µm	Width, min, µm	Width, max, µm
Sulfide	2 (.00008)	4 (.00016)	>4 (.00016)	12 (.0005)
Alumina	2 (.00008)	9 (.00035)	>9 (.00035)	15 (.0006)
Silicate	2 (.00008)	5 (.0002)	>5 (.0002)	12 (.0005)
Oxides	2 (.00008)	8 (.0003)	>8 (.0003)	13 (.0005)

A total of 320 microscopic fields (0.5mm^2/field) on the as-polished specimen surface were scanned automatically by Clemex CIR 5.0 software to collect inclusion data (i.e. shape, type, and size of inclusions) from field#1 to field#320 (as shown in Figure 3.9) for each specimen. Each field was examined with 100X magnification. The software then analyzed the inclusion data for all fields and expressed the results according to ASTM E45 and JIS G0555 standards. One of the limitations of the software is that the inclusion data (i.e. inclusion density or size) that have been analyzed was not stored in the software but is expressed directly in terms of severity levels (ASTM E45 standard) and area fraction% (JIS G0555 standard). This limitation is avoided if using SEM-EDX for evaluation, as the inclusion data was recorded manually before determining the severity level.

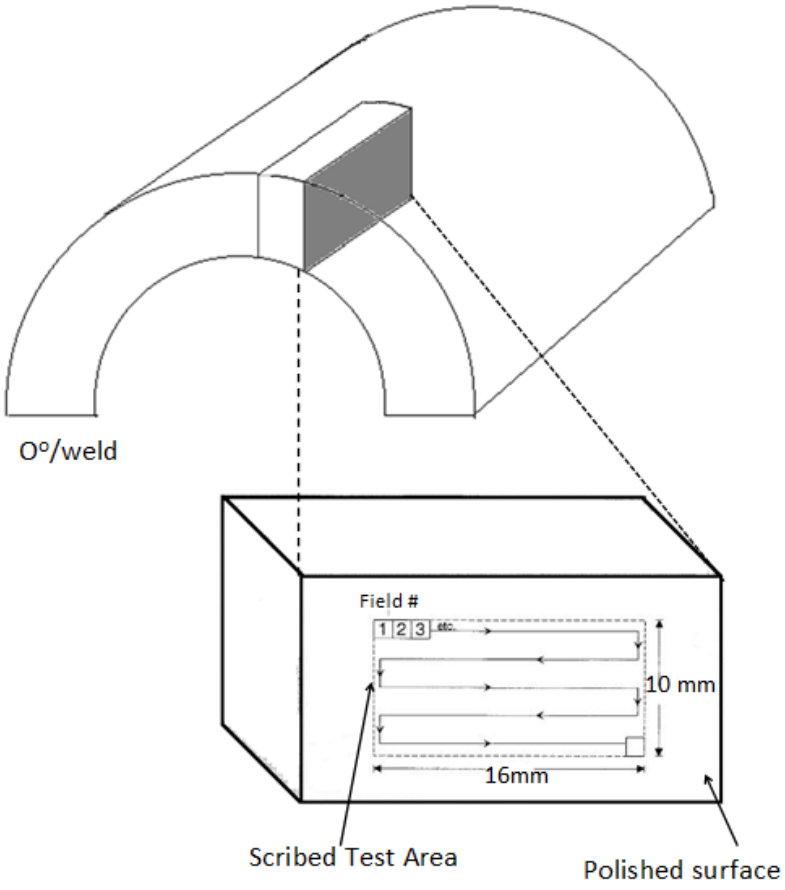

Figure 3.9: Illustration of cleanliness examination by Clemex CIR 5.0 system [62].

3.5 Characterization of carbides

3.5.1 Image analysis technique

Characterization of carbides was performed using professional image analysis software ImageJ 1.46. Image J is written in Java and can run in all operating systems including Linux, Mac OS X and Windows. The area fraction of carbides can be determined using Image J. For this purpose, metallographic specimens were prepared, polished, and then etched with 2% Nital solution to reveal the microstructural features. Same specimen preparation procedure described in Chapter 3.2 was applied and SEM images were taken with magnification of 5000x. Eight SEM images were taken for each specimen for image analysis.

To obtain measurement of the area fraction of different shapes of carbides,

the size and shape of the carbides have to be defined in ImageJ. In this study, only elongated and globular shape of carbides were considered. The shape of carbides was defined based on the circularity of particles in ImageJ. The circularity of particle can be set in a range from value 0 to 1, with 1 being perfectly circular. For globular carbides, the range of circularity was set to 0.8-1 for all specimens assuming some particles are not perfectly circular. For elongated carbides, the range was set to 0-0.3 for all specimens. The size of carbides also can be set in a range of 0 to infinity (μm^2). To define the size of the elongated carbides reasonably, the length and width of 30 randomly selected elongated carbides were measured in ImageJ for each image. The range for size of elongated carbides was then input in ImageJ for automatic analysis on these carbides. Then the area fraction (%) of elongated carbides was generated by the software. Similar procedure was repeated for obtaining area fraction of globular carbides.

The composition of carbide particles was identified using an SEM equipped with JAMP-9500F Auger microprobe (JEOL). The accelerating voltage and emission current for both the SEM and Auger imaging were 15 kV and 8 nA, respectively. The working distance was 24 mm. The sample was rotated 30 degree away from the primary electron beam to face the electron energy analyzer. M5 lens with 0.6% energy resolution was used for the Auger spectroscopy and imaging.

4. RESULTS

4.1 Microstructures

Based on the variations of processing and alloying strategies, the microstructures of the steels are shown in Figures 4.1-4.7. In general, these microstructures were tempered martensite (except for HSLA 80-2 steel). The difference between the microstructures is the distribution and shape of carbides.

The microstructure of ERW-L80-B (Figure 4.1) consists mainly of ferrite and carbides. The carbides of ERW L80-B are mostly globular in shape and distributed randomly in the matrix. Comparing with the Seamless L80-B steel in Figure 4.2, the microstructure is very different despite these two steels are both alloyed with Ti-B. The microstructure of Seamless L80-B (Figure 4.2) consists of ferrite and carbides, and islands of lamellar pearlite. Most of the carbides are clustered inside the lamellar structure and exhibit an elongated shape. Some are distributed inside the ferrite or along the grain boundaries.

Figure 4.3 shows the microstructure of ERW L80-MnCr steel. The microstructure consists of tempered martensite. The carbides seem to be globular in shape. Segregation banding is present (as indicated by the arrow in Figure 4.3). Figure 4.4 shows the microstructure of Seamless L80-Mo steel. Similar to Seamless L80-B, the microstructure consists of ferrite and carbides, and islands of lamellar pearlite. Most carbides are distributed in the lamellar pearlite and exhibit an elongated shape. Some are distributed inside the ferrite or along the grain boundaries. The microstructures of the seamless materials indicate that Seamless L80-B and Seamless L80-Mo may not have been properly quenched during processing visible by the presence of lamellar pearlite. The microstructure of ERW L80-CrMo (in Figure 4.5) consists mainly of tempered martensite. The carbides are distributed inside ferrite and along grain boundaries. Similarly for ERW L80-0.5Mo steel (in Figure 4.6), the microstructure consists of tempered martensite. However the carbides appeared to be smaller and more dispersed throughout structure.

Finally, for HSLA 80-2 steel (in Figure 4.7), the microstructure consists of polygonal ferrite and carbides. Most carbides are distributed along the grain boundaries, with some inside the ferrite.

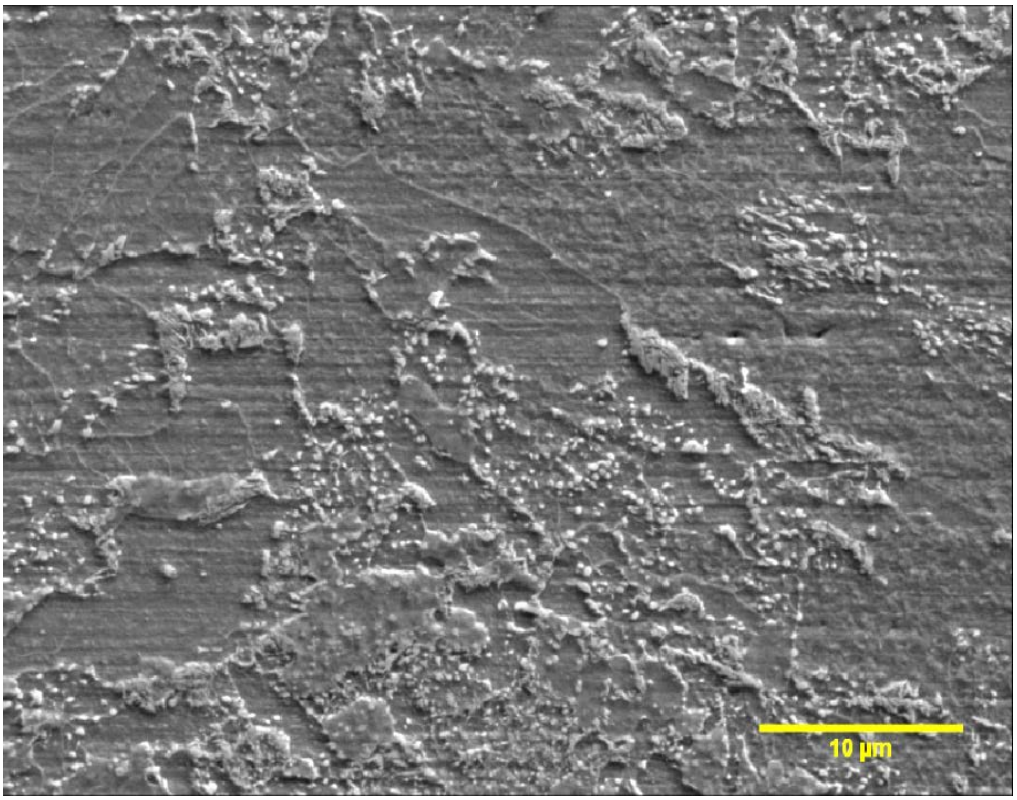

Figure 4.1: ERW L80-B microstructure.

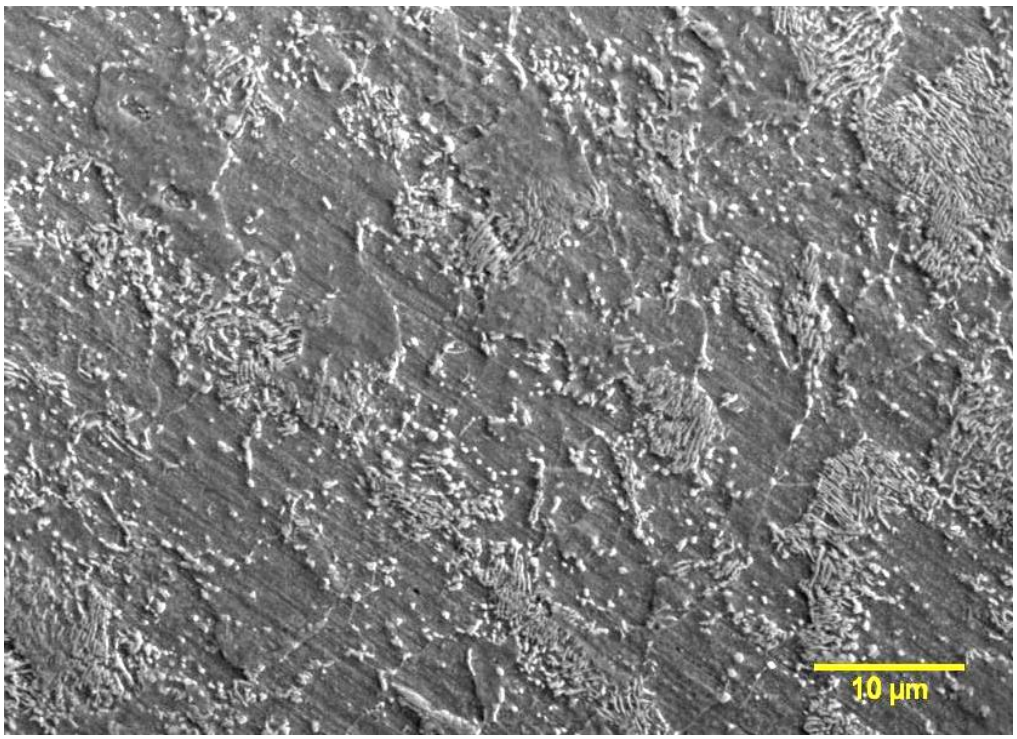

Figure 4.2: Seamless L80-B microstructure.

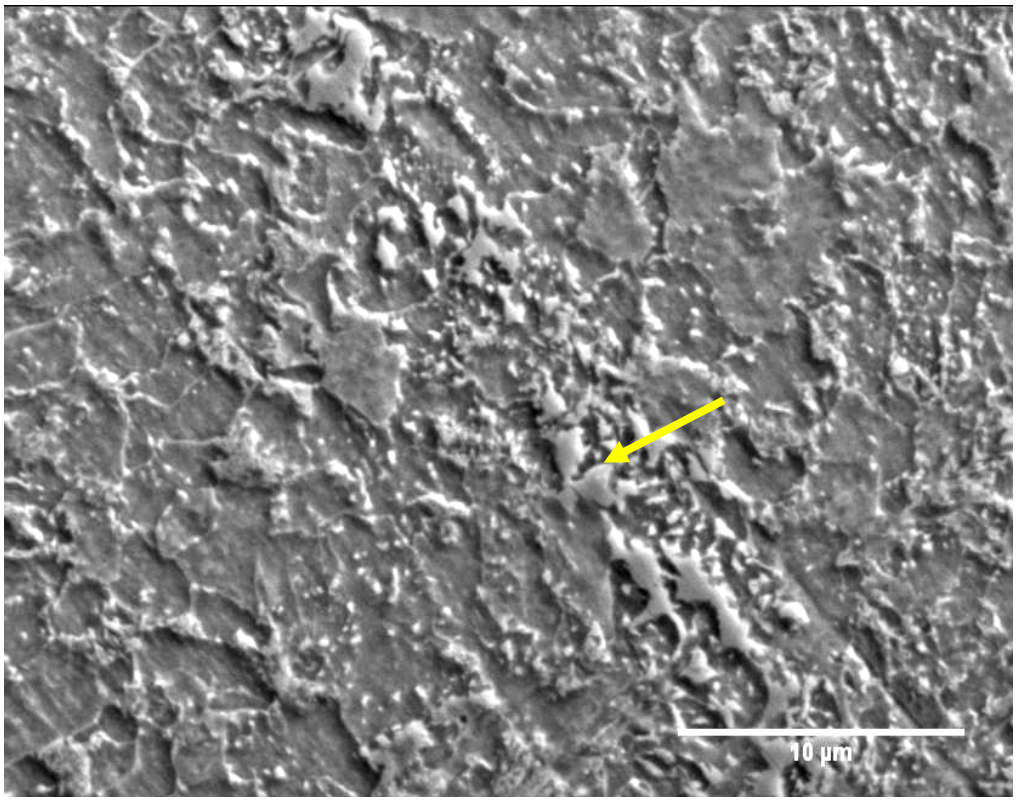

Figure 4.3: ERW L80-MnCr microstructure. The arrow indicates segregation banding.

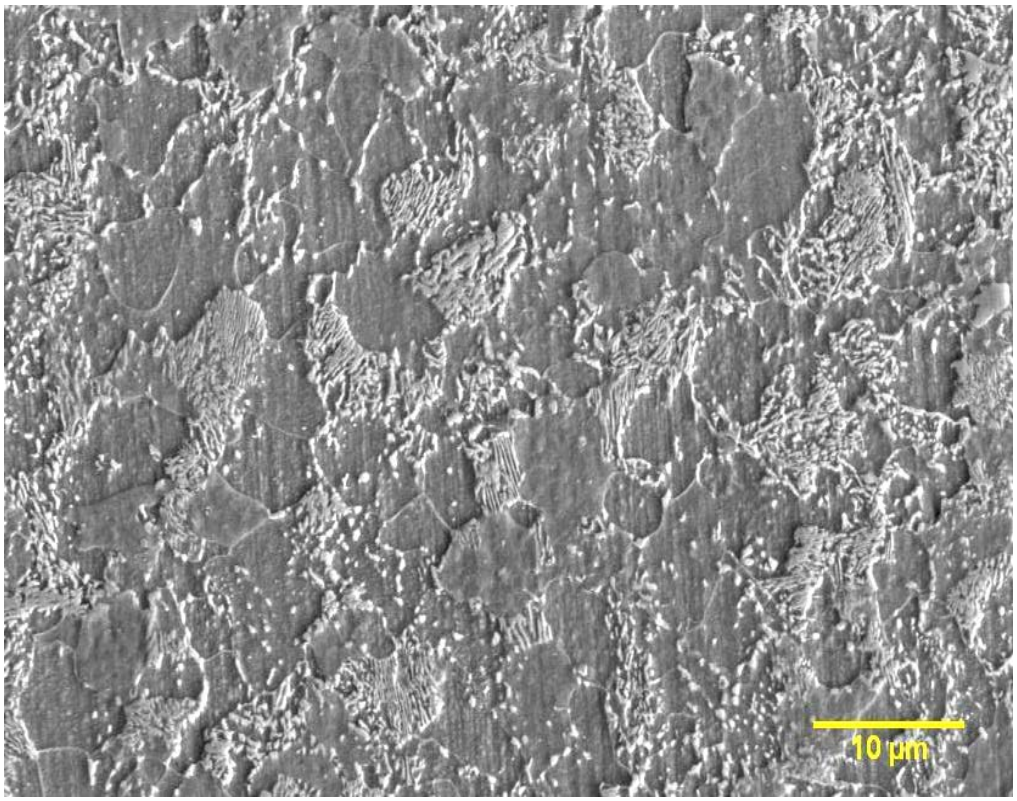

Figure 4.4: Seamless L80-Mo microstructure.

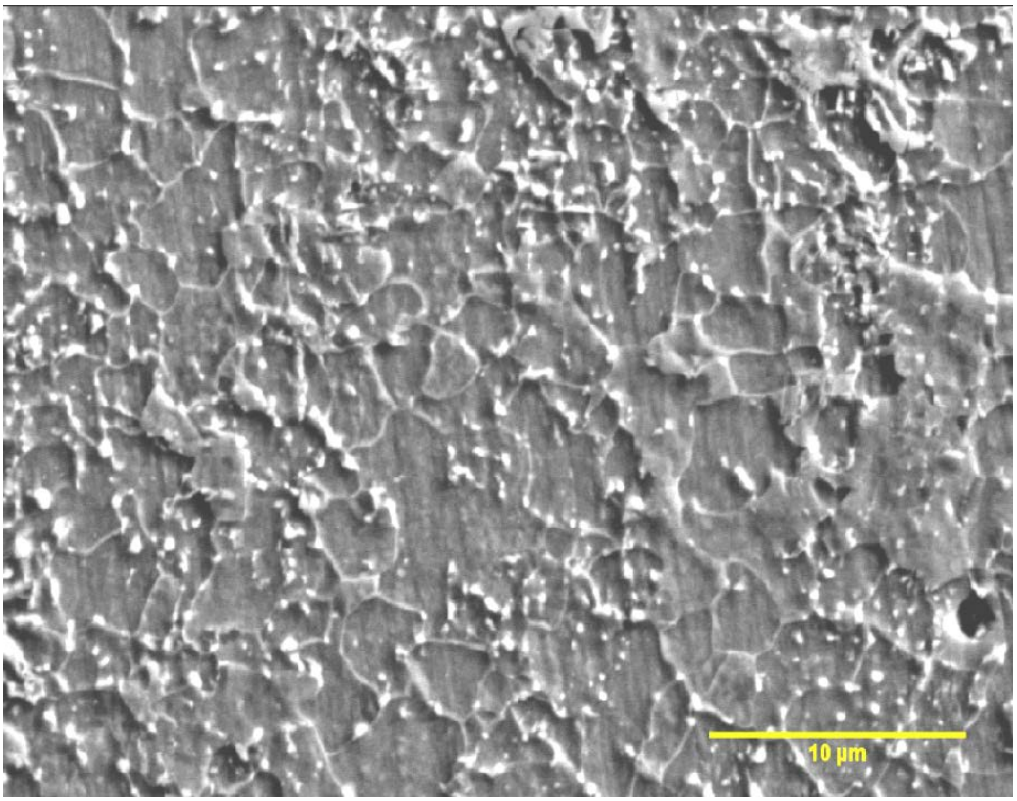

Figure 4.5: ERW L80-CrMo microstructure.

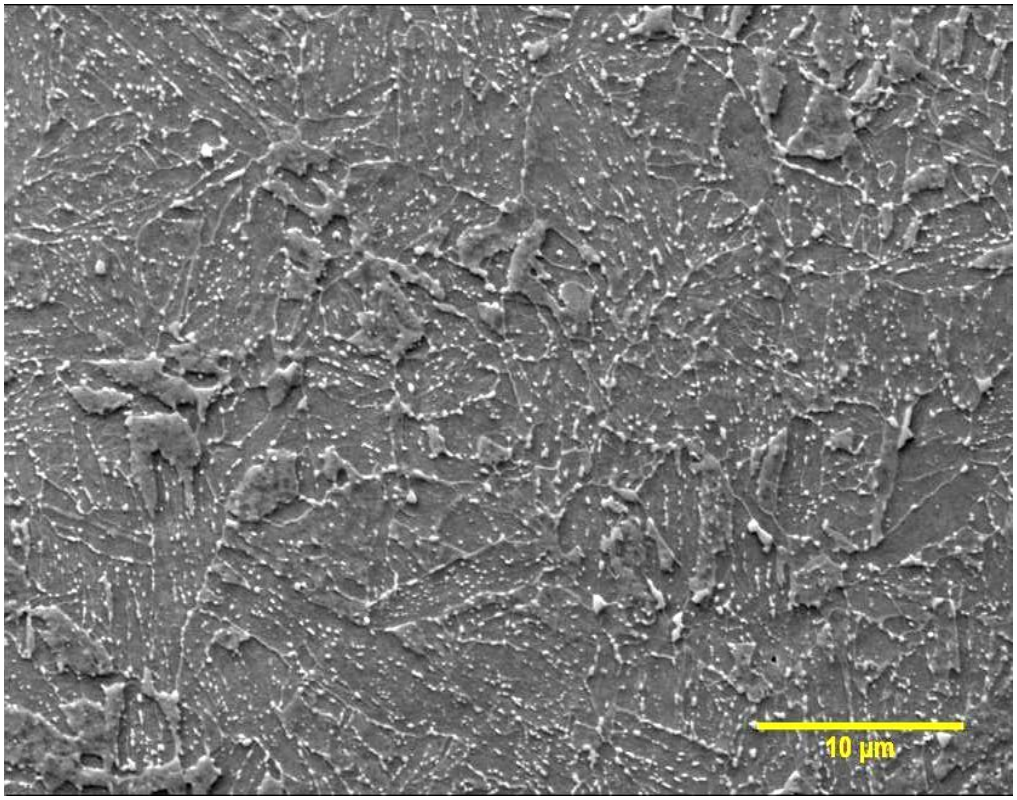

Figure 4.6: ERW L80-0.5Mo microstructure.

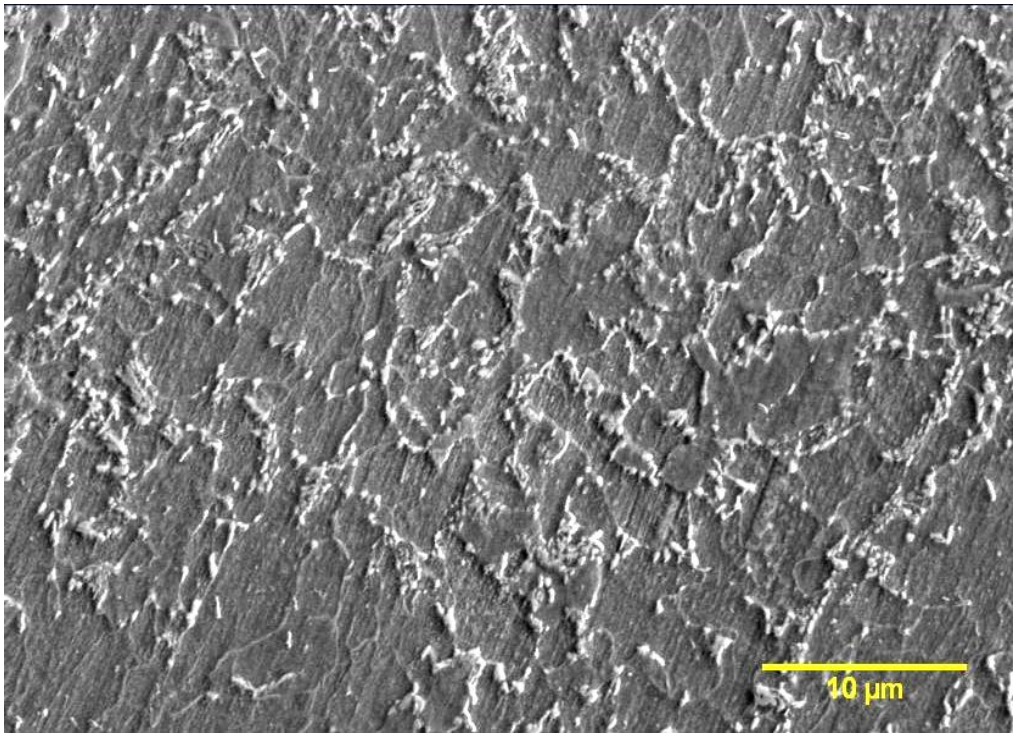

Figure 4.7: HSLA 80-2 microstructure.

4.2 Materials strength

Table 4.1 shows the average yield strength, tensile strength, and Rockwell hardness (HRB) values for the tested steels. The differences in yield strength, tensile strength are large among steels. The actual yield strength and tensile strength values are provided by Evraz Inc. NA.

Table 4.1: Mechanical properties of the casing steels.

Steel	Actual yield strength*(MPa)	Ultimate Tensile strength*(MPa)	Rockwell Hardness** (HRB)
ERW L80-B	618	706	89.8±2.4
Seamless L80-B	613	713	89.4±4.8
ERW L80-MnCr	682	769	92.0±1.9
Seamless L80-Mo	642	745	90.6±4.2
ERW L80-CrMo	585	665	88.5±4.9
ERW L80-0.5Mo	610	680	89.1±1.7
HSLA 80-2	616	689	89.7±3.4

Note: * Provided by Evraz Inc.NA

**the Rockwell hardness was measured at three locations around the shoulders of round bar tensile specimen (Figure 3.6), i.e. every 120^{o}. These values correspond to the hardness of mid-thickness of the steel pipe wall.

4.3 Constant load SSC test (Proof ring test)

The SSC susceptibility is evaluated based on time to failure data and loss in ductility (i.e. RAR). The RAR is defined in Chapter 3.3.1 as the ratio of ductility in H_2S environment to the ductility in an inert environment. This ratio of ductility is a better evaluation criterion than just the ductility in test environment because it factors out the basic differences in chemical compositions and mechanical properties of the materials. Table 4.2 shows the overall result from the proof ring tests in NACE TM0177 test solution A with saturated hydrogen sulfide for test duration of 720 hours or until a complete breakage of the specimen. All steels were tested at 85% of SMYS (i.e. 552MPa for L80 casing steel in API 5CT specification). For all steels, a repeated test of a fresh specimen was conducted at the same test conditions to confirm the reproducibility of the results. The starting pH should be in the range of 2.6-2.8 and final pH needs to be less than 4.0 for the test to be valid. Among all the tested steels, ERW L80-0.5Mo was the only one that passed the test for 720 hours test duration.

4.3.1 Effect of mechanical properties versus SSC resistance

Figures 4.8, 4.9, and 4.10 show the effect of materials' hardness, yield strength, and tensile strength, respectively on SSC resistance in terms of time-to-failure. The steels either failed within 100 hours or after more than 400 hours. ERW L80-0.5Mo and ERW L80-B are the two steels with time to failure greater than 400 hours. ERW L80-MnCr steel failed the SSC test in 20 hours. In general, time to failure decreases as the hardness, yield strength, and

tensile strength of steels increase.

Table 4.2: SSC proof ring test results.

Steel	pH Initial/Final	Result	Time to failure (hour)	RA_{H2S}/RA_{air}
ERW L80-B	2.6/3.5	Failure	624	0.26
	2.7/3.5	Failure	600	0.24
Seamless L80-B	2.7/3.6	Failure	52	0.24
	2.7/3.	Failure	60	0.23
ERW L80-MnCr	2.7/3.6	Failure	20	0.13
	2.6/3.6	Failure	17	0.16
Seamless L80-Mo	2.7/3.6	Failure	36	0.15
	2.7/3.6	Failure	32	0.12
ERW L80-CrMo	2.7/3.6	Failure	60	0.25
	2.7/3.6	Failure	62	0.24
ERW L80-0.5Mo	2.6/3.5	No Failure	>720	0.30
	2.7/3.6	No Failure	>720	0.31
HSLA 80-2	2.6/3.6	Failure	60	0.28
	2.7/3.6	Failure	80	0.30

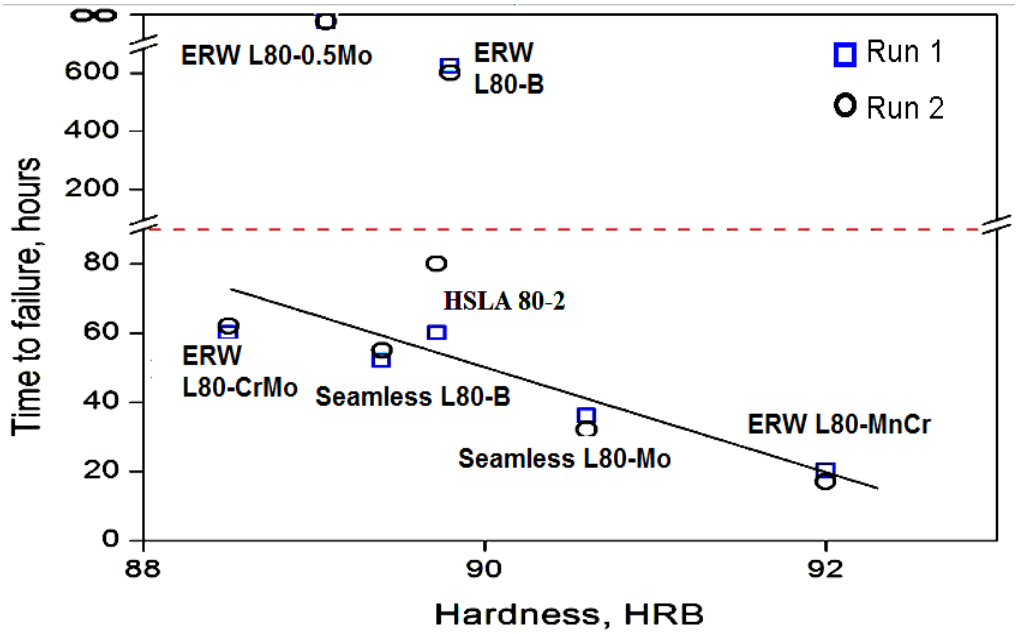

Figure 4.8: Time-to-failure versus hardness of steels.

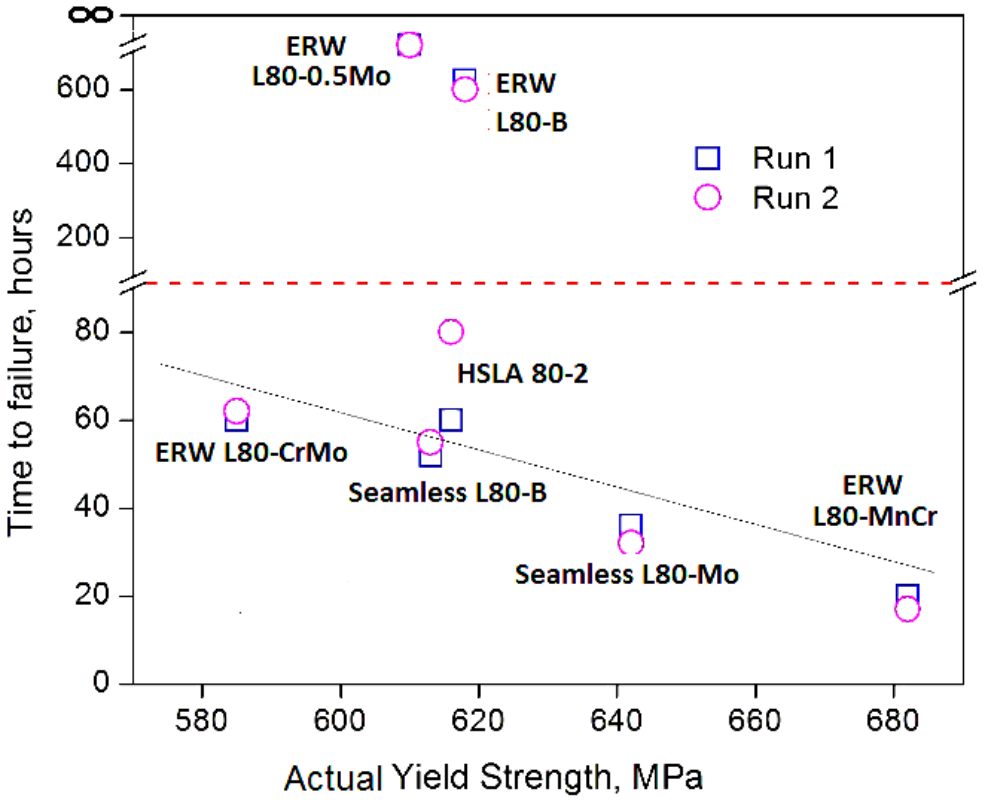

Figure 4.9: Time-to-failure versus actual yield Strength of steels.

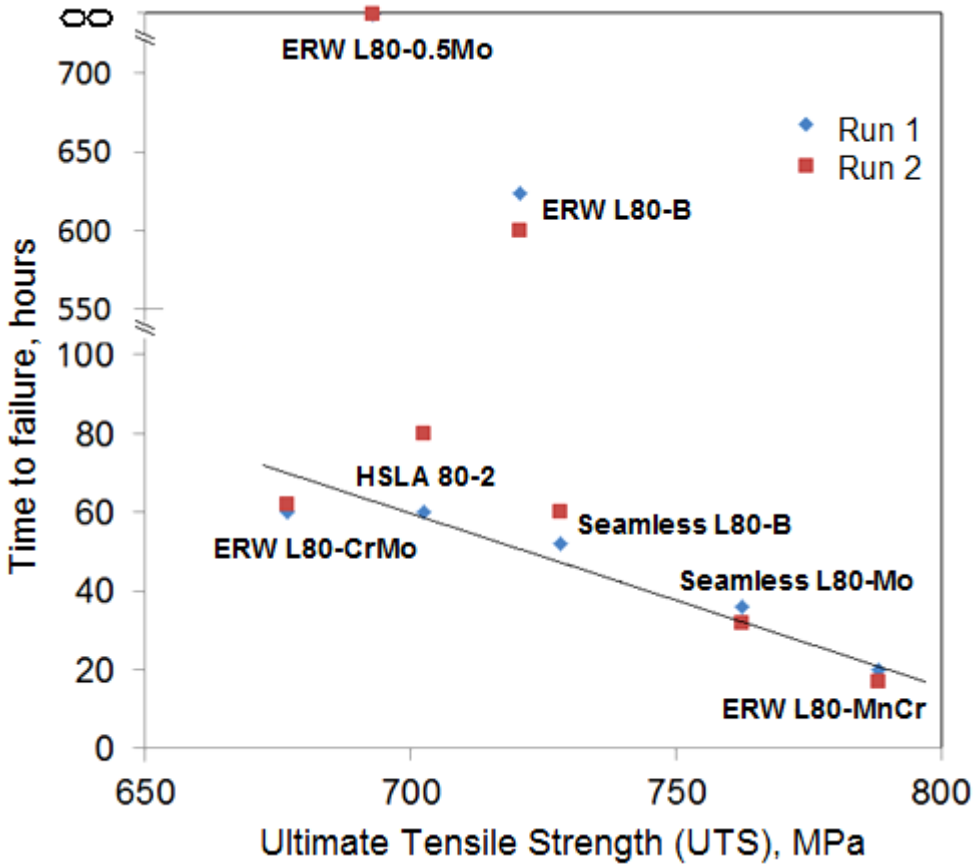

Figure 4.10: Time-to-failure versus ultimate tensile strength of steels.

Figures 4.11, 4.12, and 4.13 show the SSC resistance in terms of RA_{H2S}/RA_{air} (RAR) versus yield strength, hardness, and tensile strength, respectively. The RAR is an indication of the environmental effect and measured the loss in ductility due to hydrogen embrittlement. In general, higher RAR indicates a high resistance to environmental cracking. Lower ratios indicate high cracking susceptibility. As seen in Figure 4.11, 4.12, and 4.13, RAR generally decrease with the increase of yield strength, hardness, and tensile strength. Despite the differences in steel alloying chemistries, an empirical linear relationship between RAR and yield strength can be generated by fitting a best linear function:

$$RAR = -0.0017 \text{ (actual yield strength)} + 1.3 \qquad 4\text{-}1$$

The R^2 for the linear equation is 0.75. This linear relationship can be used to predict the SSC resistance in terms of RAR for the yield strength of steel from 580 to 682 MPa.

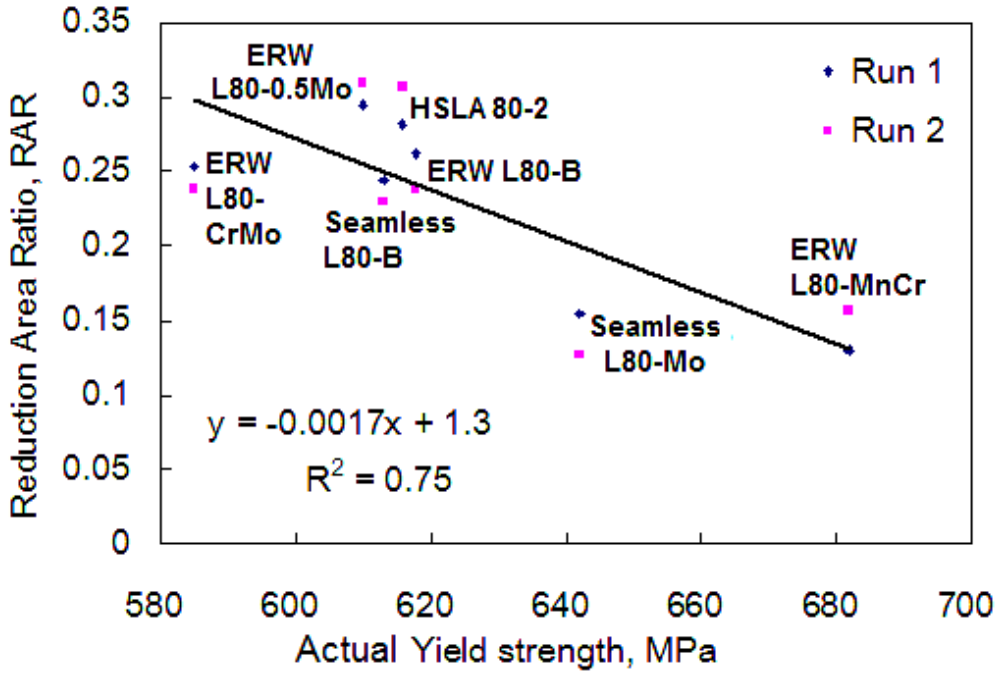

Figure 4.11: RAR versus actual yield strength of steels.

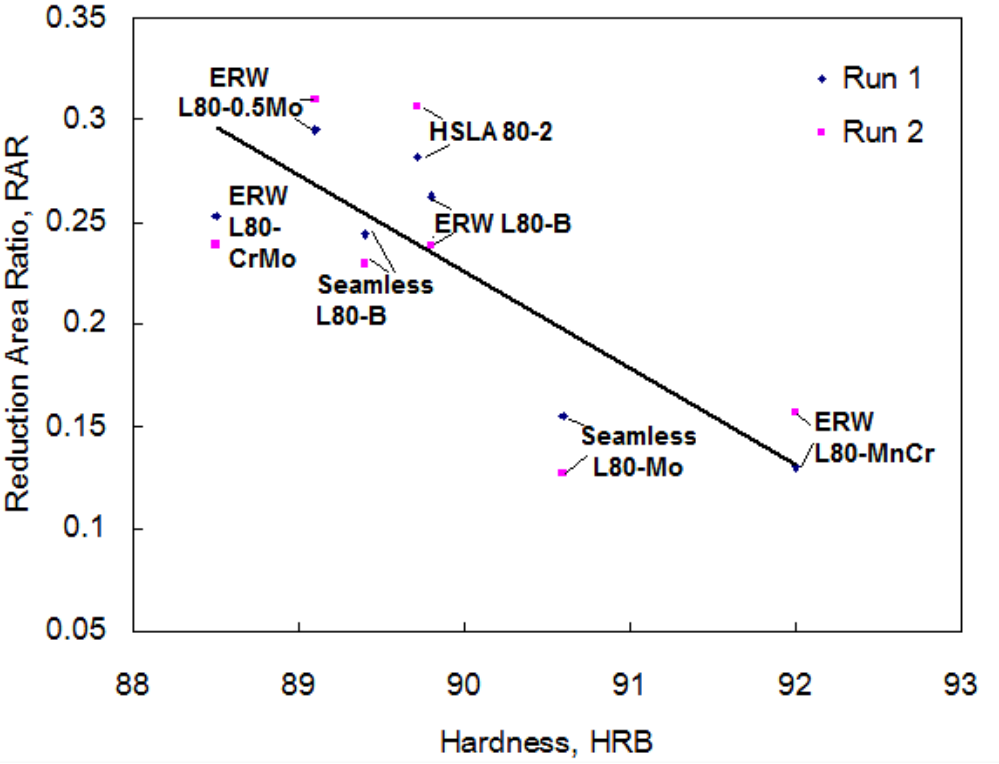

Figure 4.12: RAR versus hardness of steels.

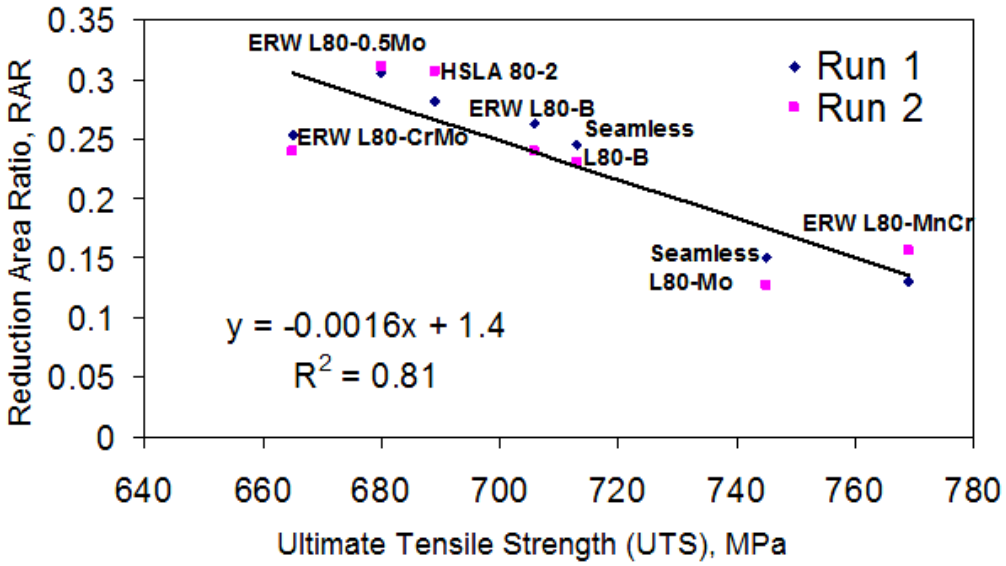

Figure 4.13: RAR versus ultimate tensile strength of steels.

A ranking for SSC susceptibility of steels could be proposed in terms of time to failure and RAR, as shown in Figure 4.14. The ranking is a little different based on different criteria for comparison.

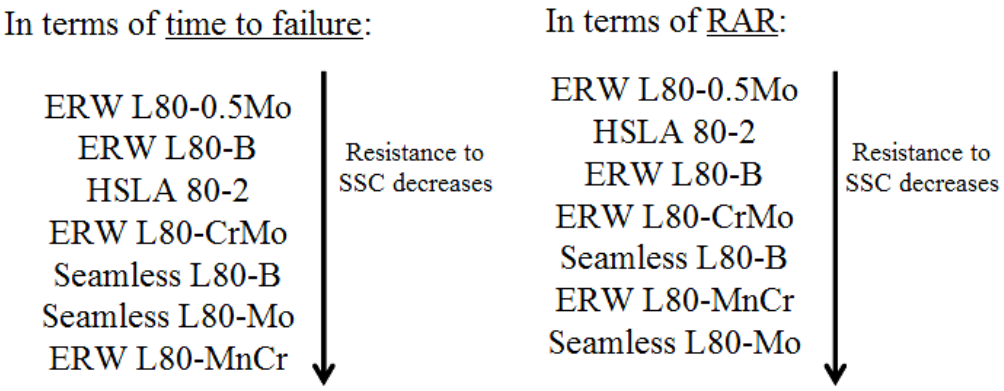

Figure 4.14: A ranking of SSC susceptibility for steels.

4.3.2. Fracture surface examination

All the fracture surfaces of the failed specimens have been examined under SEM. The identification of HIC and SSC cracks, defined in Chapters 2.3.2 and 2.3.3 (page 14), was determined by examining the cracks at 3000X using the SEM as described in Chapter 3.3.7 (page 49). Figures 4.15-4.20 show the fracture surfaces of the test specimens. In Figure 4.15 and Figure

4.16, from the direction of radial marks on the surface, fracture appears to be initiated from the pitting site near the surface (as indicated by the arrow on both figures) and it produces a large, unified, deformation-free (brittle) crack region. This brittle crack region propagated with increasing coarseness until the remaining ligament became insufficient to accommodate the nominal section load, and then fracture ensued (by a ductile mechanism). Figure 4.17 shows a similar fracture surface with brittle crack regions but it is harder to identify the initiation site. SSC could have initiated from the surface or inside the specimen. Many transgranular cracks propagating in the neutral axis are observed. These are believed to be HIC cracks since they are not propagating in a direction perpendicular to the applied stress. A secondary SSC crack along the gauge section of the specimen (perpendicular to the direction of applied stress) is observed. In Figure 4.18, the fracture appears to be similar to those shown in Figure 4.15 and 4.16. From the direction of radial marks, the fracture appears to have initiated near the surface producing a large brittle region. Transgranualar HIC cracks propagating in the neutral axis were observed on the surface (as indicated by arrows on the figure). The fracture surface in Figure 4.19 and 4.20 are hard to interpret but a similar brittle crack region is observed. There may be several crack initiation sites on the surface. Transgranular HIC crack propagating in the neutral axis is observed (as indicated by arrow on the figures).

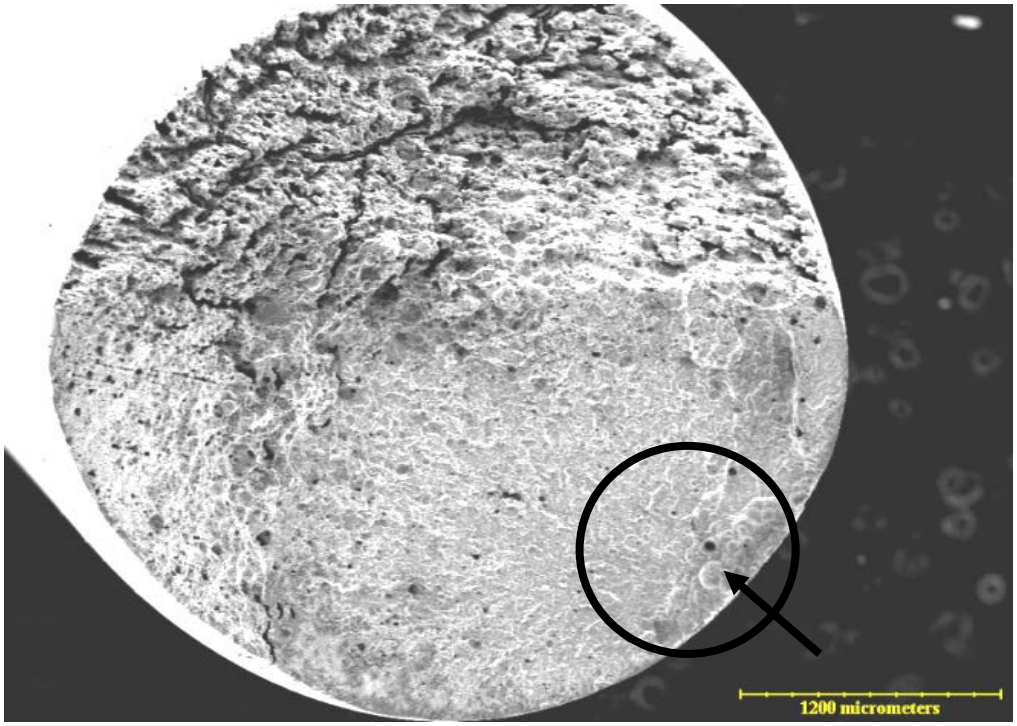

Figure 4.15: ERW L80-B fracture surface.

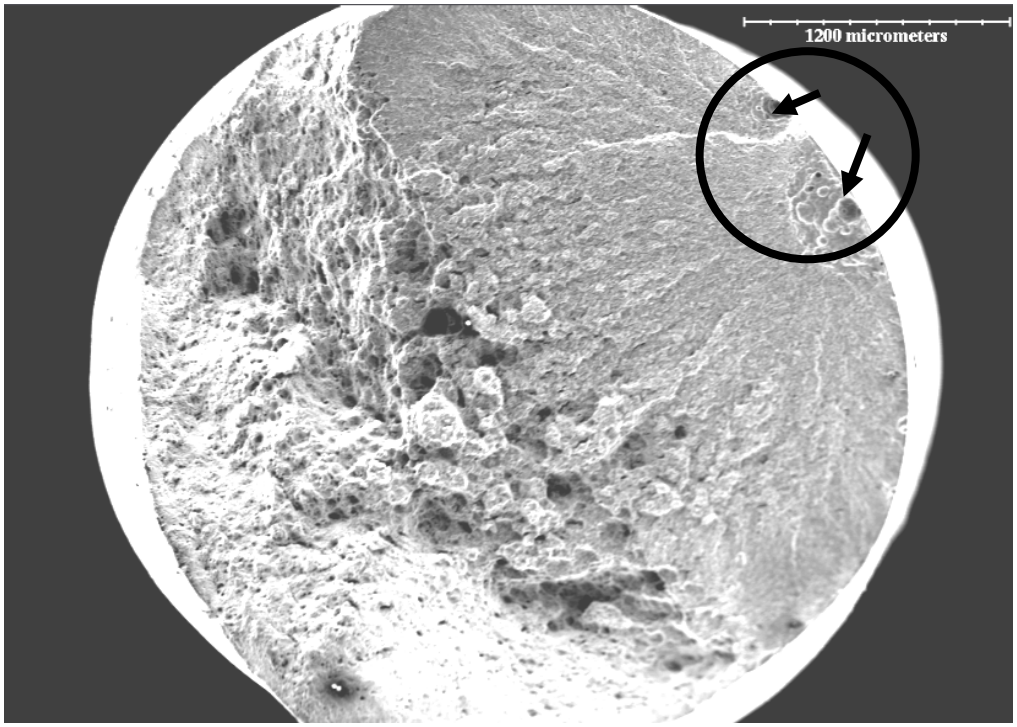

Figure 4.16: Seamless L80-B fracture surface.

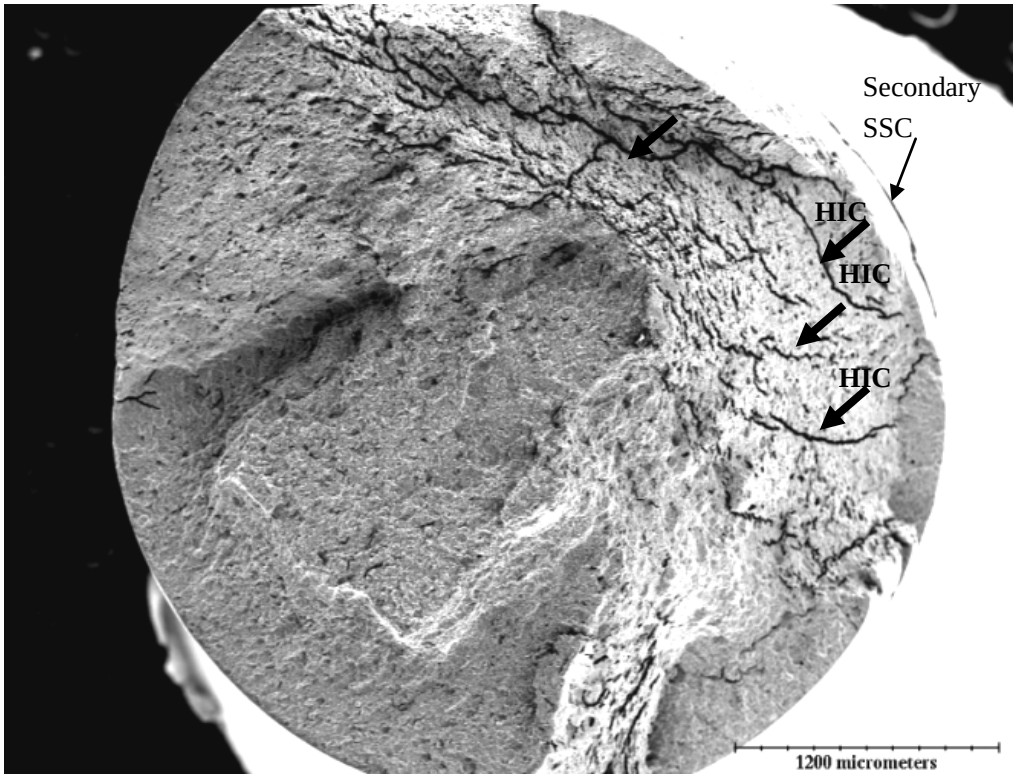

Figure 4.17: ERW L80-MnCr fracture surface.

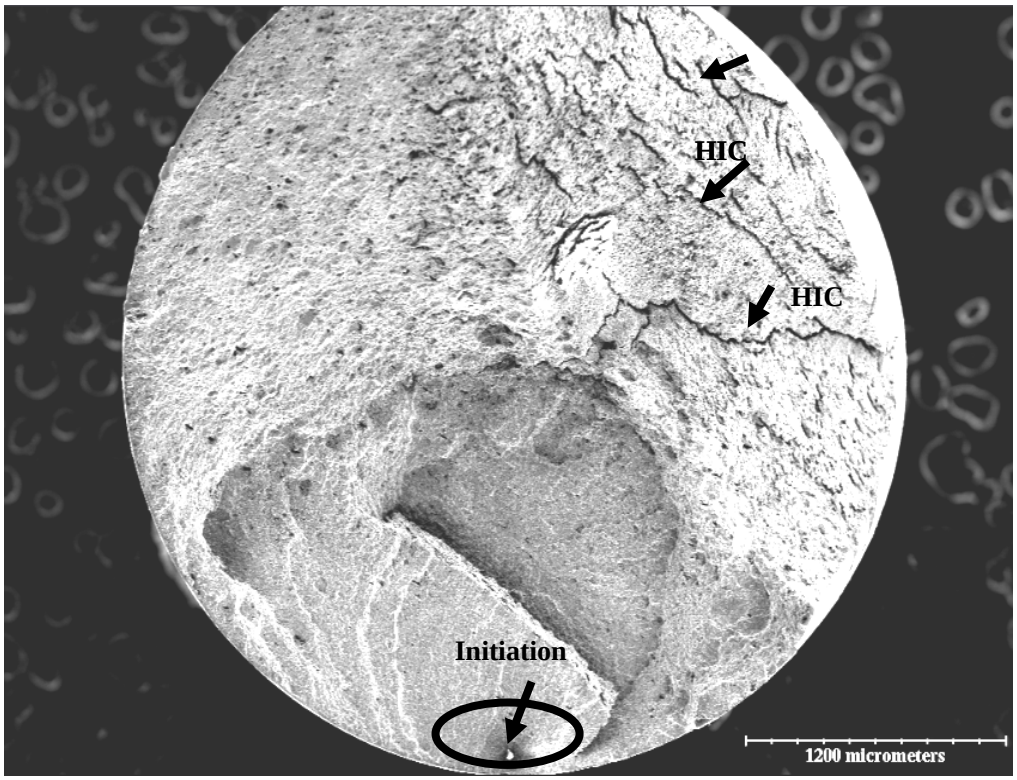

Figure 4.18: Seamless L80-Mo fracture surface.

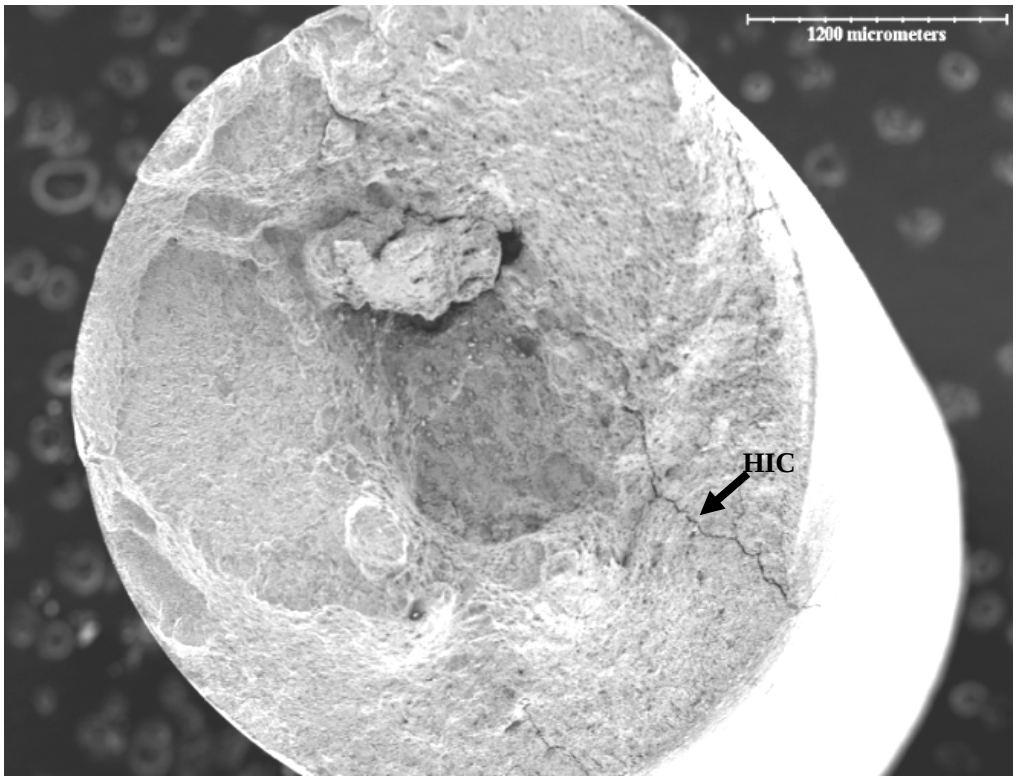

Figure 4.19: ERW L80-CrMo fracture surface.

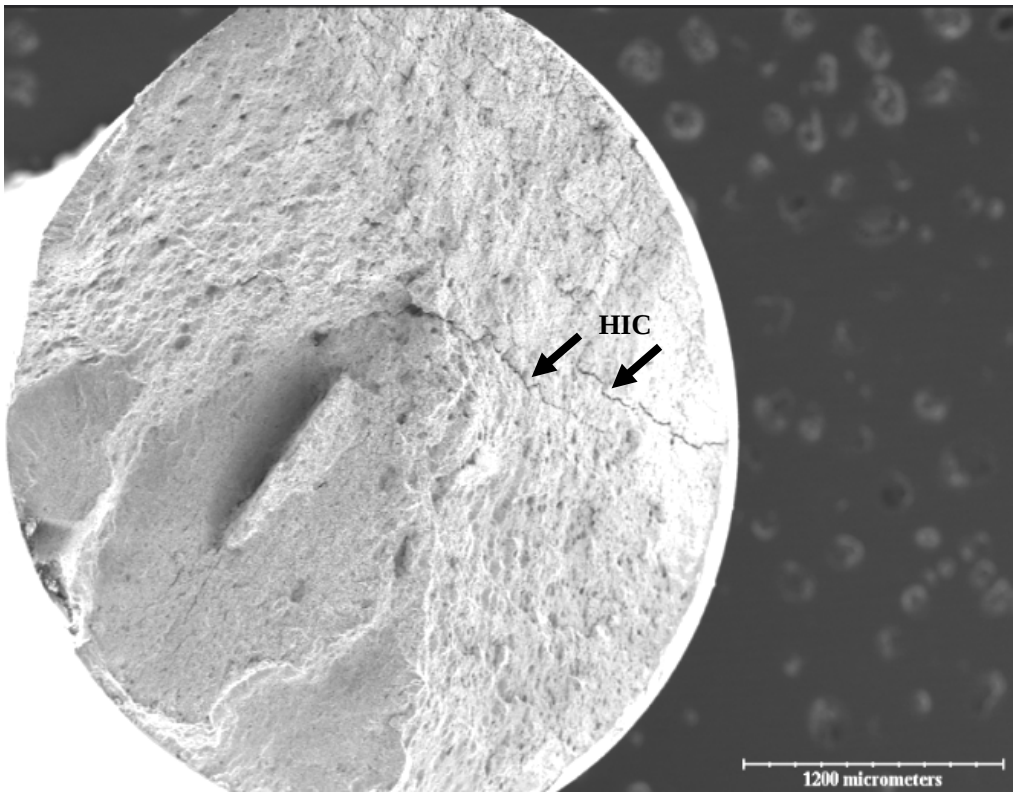

Figure 4.20: HSLA 80-2 fracture surface.

The fracture surface of a specimen failing in air has a characteristic of ductile dimple fracture (as shown in Figure 4.21). This is very different from the fracture surfaces shown in Figures 4.15-4.20. The specimens failed in H_2S environment show distinctive brittle regions caused by hydrogen embrittlement on all surfaces. The size of the brittle area appears to be related to the steel's resistance to SSC. The brittle areas can be measured by selecting the area manually (as shown in Figure 4.22) in any image analysis software (e.g. ImageJ 1.46, or Adobe Acrobat X pro) with an area measuring tool (accuracy:±2%). The brittle-ductile area ratio (%) is then determined as the measured brittle area divided by the total deformed fracture area. Figure 4.23 shows the effect of hydrogen embrittlement on the fracture surface. It can be seen that the larger the brittle area, the lower the cracking resistance.

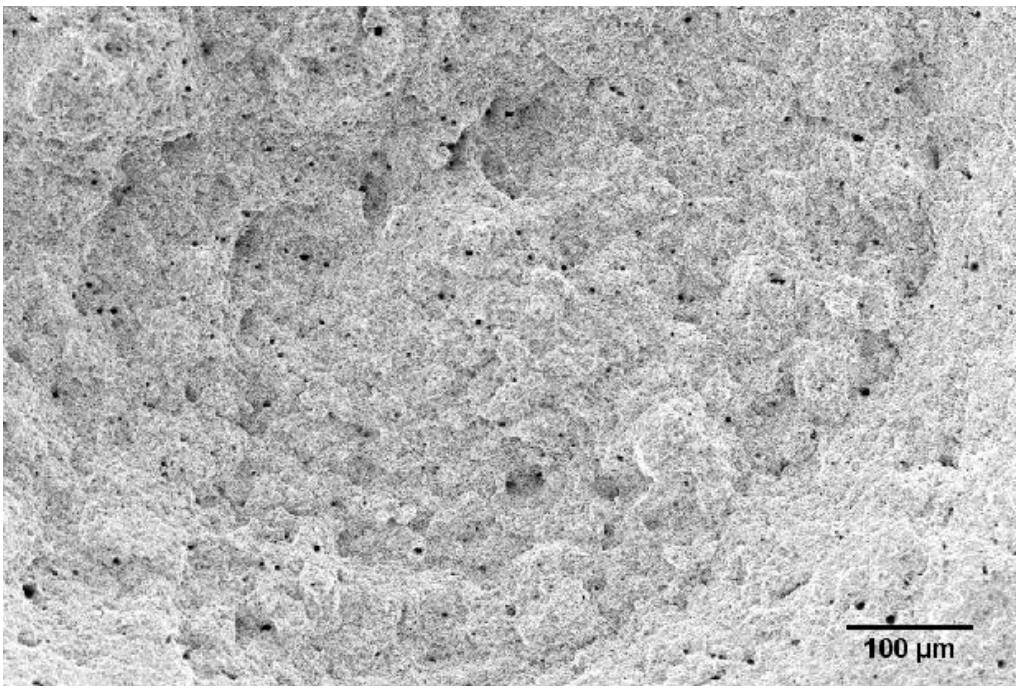

Figure 4.21: Fracture surface of Seamless L80-Mo steel failing in air.

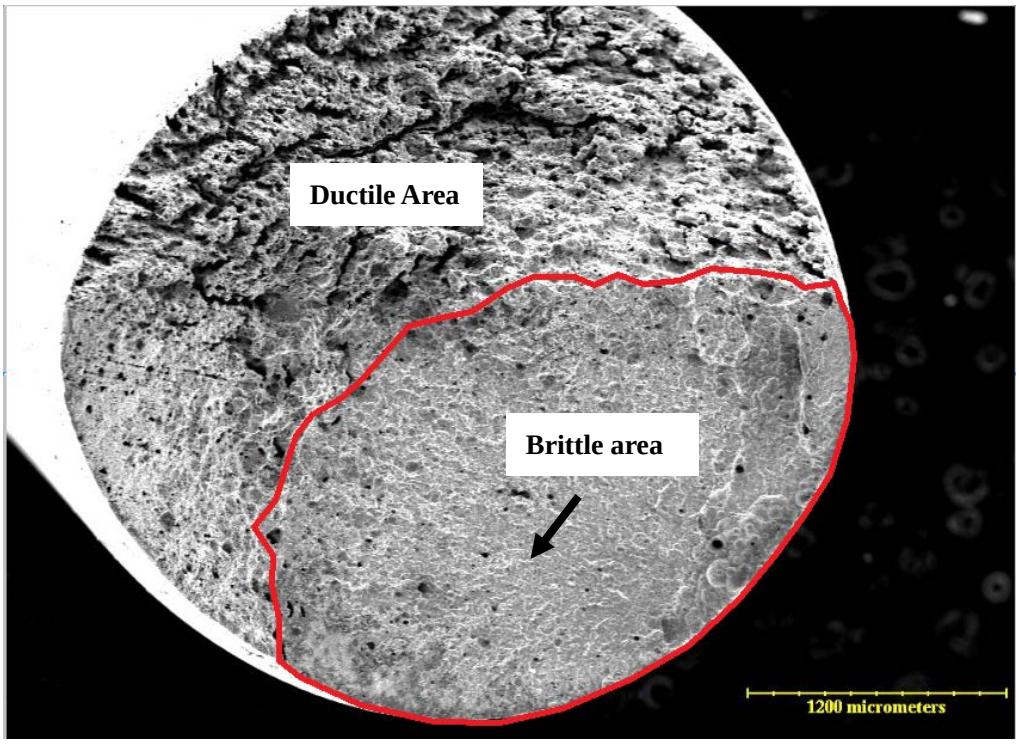

Figure 4.22: Measurement of brittle area on fracture surface (ERW L80-B).

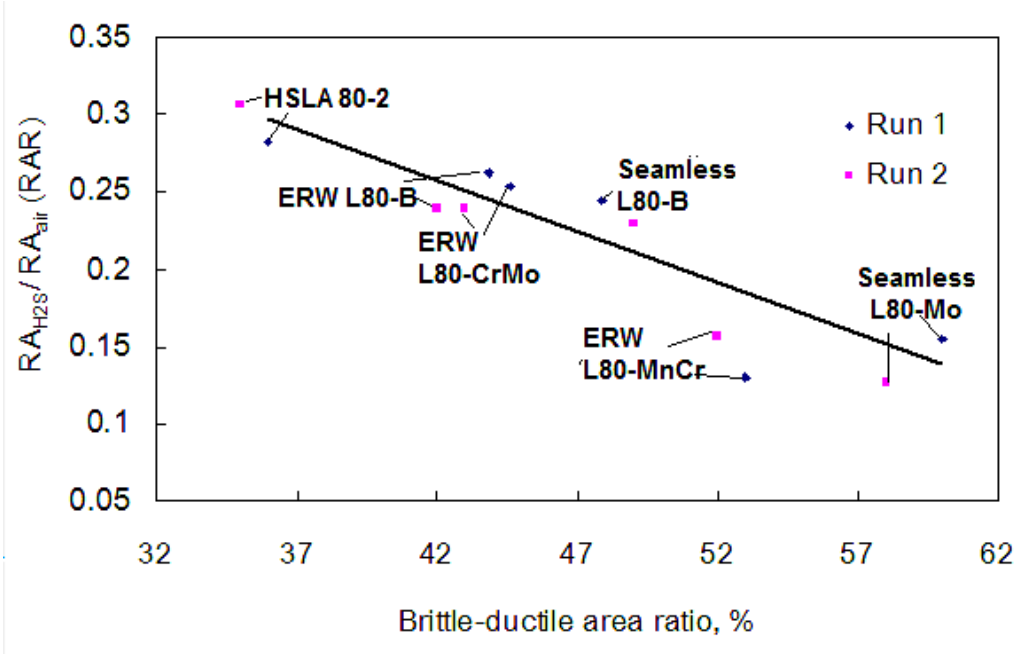

Figure 4.23: Brittle area fraction (%) versus RAR.

The SSC fracture mode is distinctive for steels with different cracking resistance. Figures 4.24-4.28 show the propagation fracture modes of the steels. For steels with higher cracking susceptibility (i.e. lower RAR), a mix of

intergranular and transgranular mode of fracture were observed for ERW L80-MnCr (RAR=0.13) and Seamless L80-B (RAR=0.24). For steels with lower cracking susceptibility, intergranular fracture is less prevalent for ERW L80-CrMo (RAR=0.25), ERW L80-B (RAR=0.26), and HSLA 80-2 (RAR=0.29).

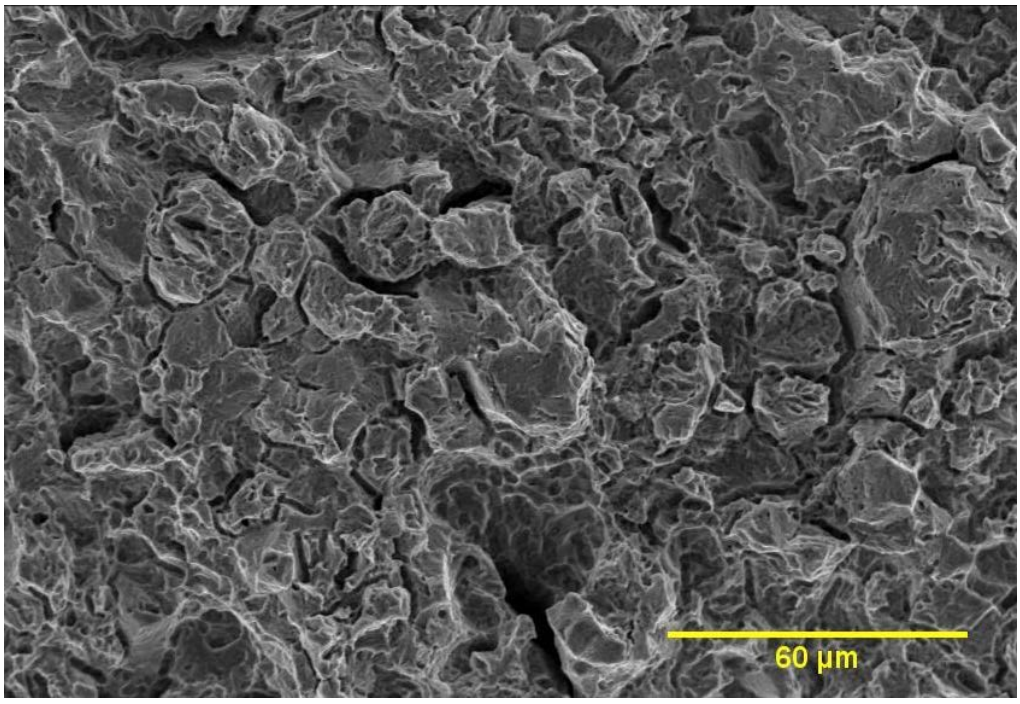

Figure 4.24: ERW L80-MnCr fracture mode.

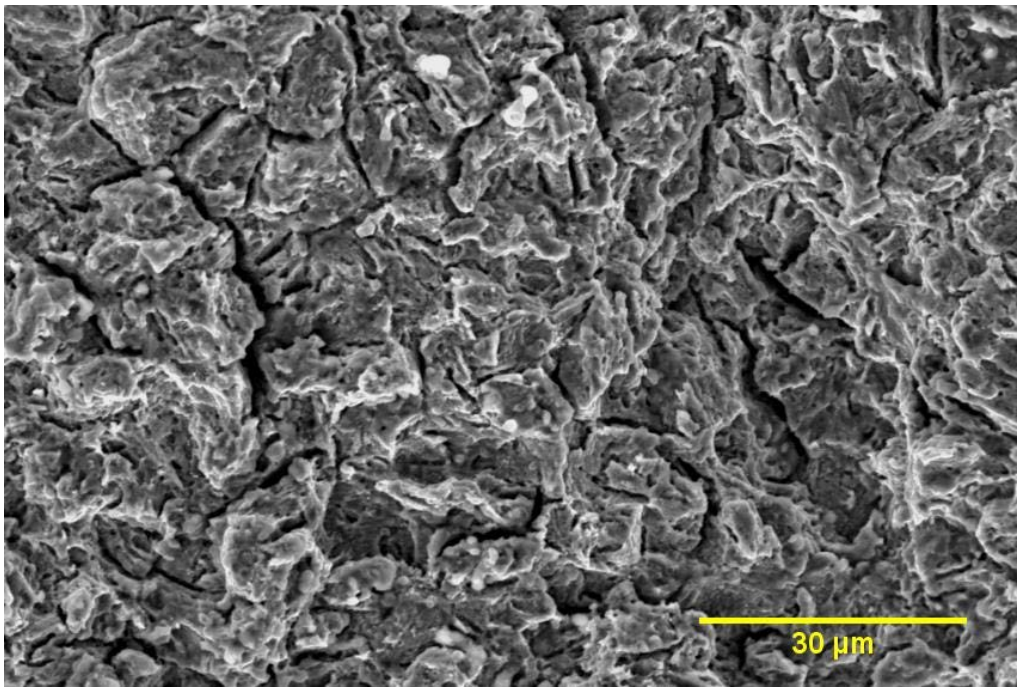

Figure 4.25: Seamless L80-B fracture mode.

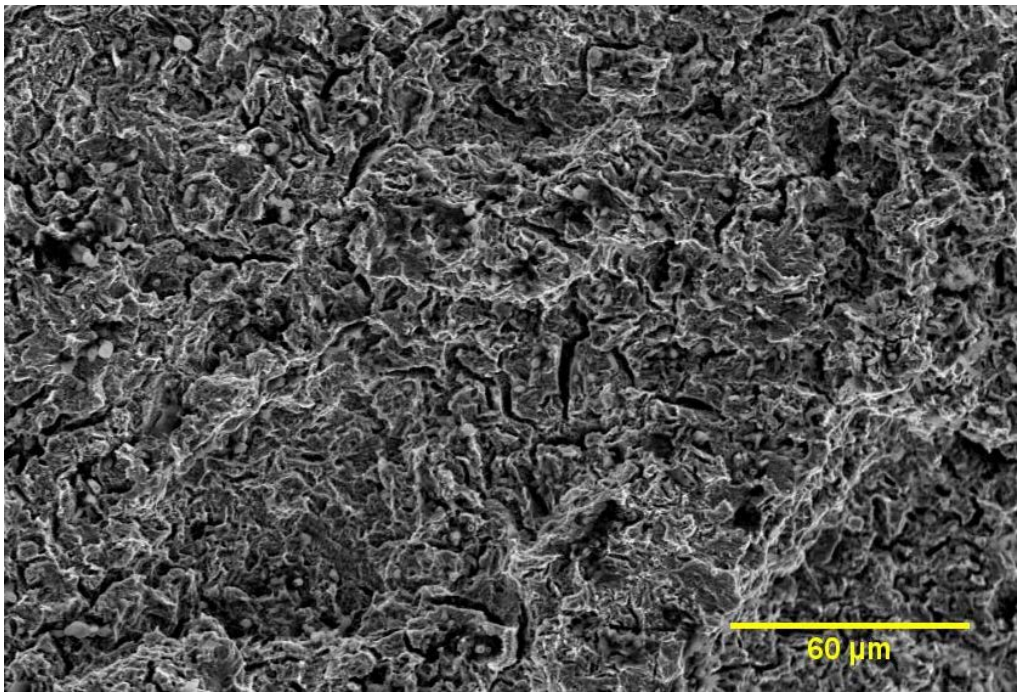

Figure 4.26: ERW L80-CrMo fracture mode.

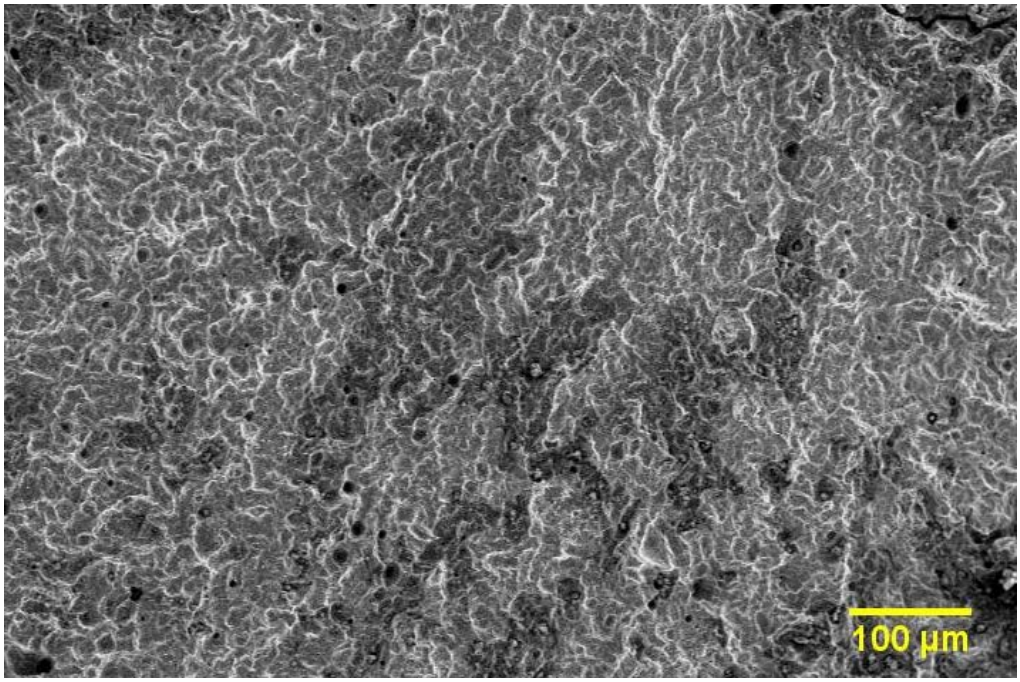

Figure 4.27: ERW L80-B fracture mode.

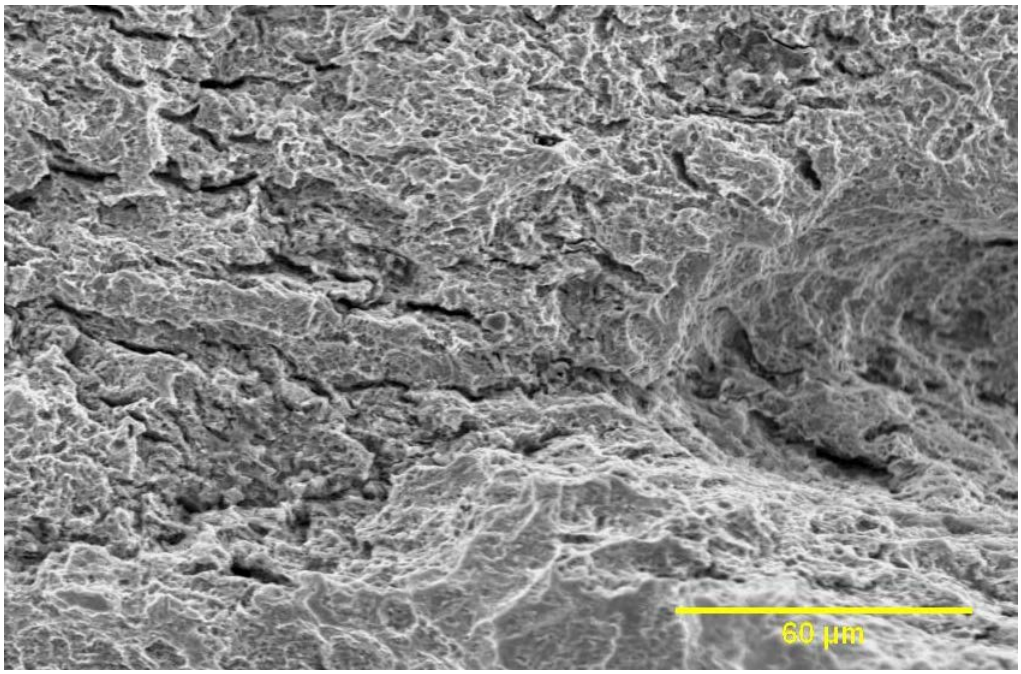

Figure 4.28: HSLA 80-2 fracture mode.

4.4 SSRT test results

SSRT tests have been performed on three steels, namely ERW L80-0.5Mo, Seamless L80-B, and ERW L80-MnCr in the same NACE A test environment and in air as a reference. The reason for choosing these three steels is because they represent different alloying strategies as previously mentioned in Chapter 3.1. ERW L80-0.5Mo is alloyed with Cr-Mo, Seamless L80-B is alloyed with Ti-B, and ERW L80-MnCr is alloyed with Mn-Cr.

Figure 4.29 shows the stress-strain curve for ERW L80-MnCr steel in NACE A test environment and in air. The ERW L80-MnCr steel tested in air shows a typical stress-strain curve for low alloy steels. The ERW L80-MnCr steel tested in NACE A environment with saturated H_2S failed in the solution soon after yielding. The effect of hydrogen embrittlement is quite significant. The specimen failed in a brittle manner with no necking taking place. Similar stress-strain curves are observed for Seamless L80-B and ERW L80-0.5Mo steels tested in air and in NACE A environment.

Figure 4.30 compares the stress-strain curves for these three steels, namely ERW L80-MnCr, Seamless L80-B, and ERW L80-0.5Mo in NACE A

environment. All three steels exhibit the same yield character with a defined Luders band plateau in the NACE environment. All specimens got out of the Luders band before failing in the solution. The Luders band plateaus were not observed in the stress-strain curves of all three steels in air. ERW L80-0.5Mo steel exhibits a larger Luders band plateau than Seamless L80-B and ERW L80-MnCr. Further discussion of the effect of Luders band on SSC is given in Chapter 5. Time to failure for ERW L80-MnCr, Seamless L80-B, and ERW L80-0.5Mo are 21.6 hours, 27.9 hours, and 33.6 hours respectively.

Figure 4.31 compares total strain to failure and fracture stress for all three steels in NACE environment. The SSC resistance of the three steels in terms of total strain to failure is consistent with the ranking of cracking resistance determined from constant load SSC test (i.e. proof ring test). ERW L80-0.5Mo steel shows higher SSC resistance with the higher total strain to failure and higher fracture stress than Seamless L80-B followed by ERW L80-MnCr which has the lowest total strain to failure and fracture stress.

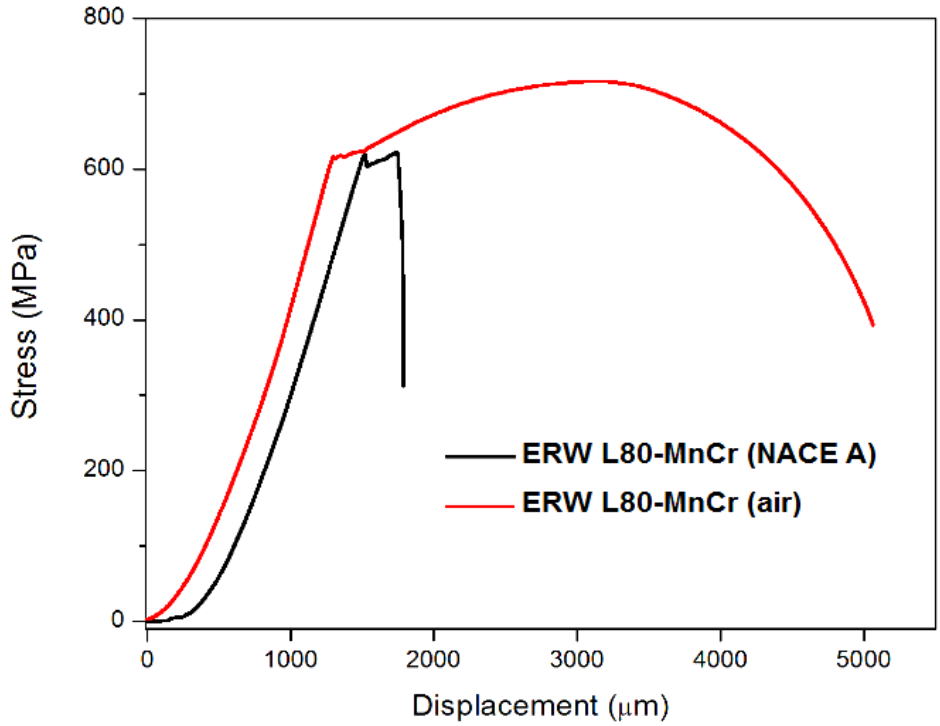

Figure 4.29: Stress-Strain curves for ERW L80-MnCr steel in NACE environment and in air.

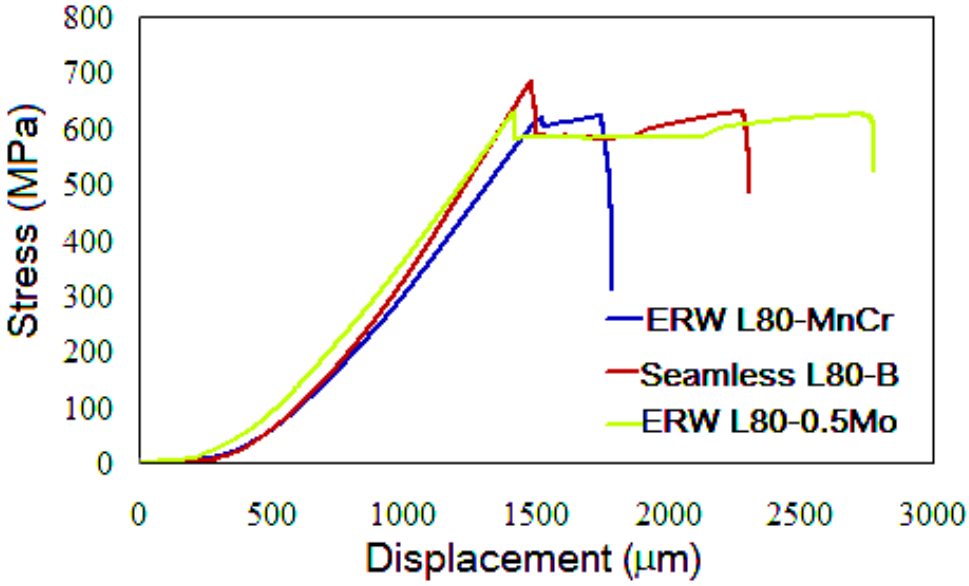

Figure 4.30: Comparison of stress-strain curves for three different alloying steels in NACE A environment.

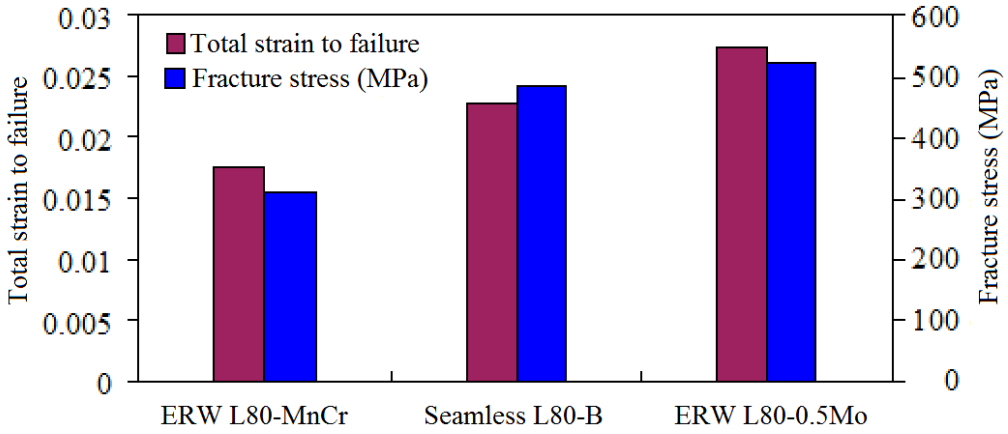

Figure 4.31: Comparison of total strain to failure and fracture stress for three different alloying steels in NACE A environment.

4.5. Characterization of inclusions

Quantitative assessments were based on ASTM E45-2005 standard and JIS G0555 standard. In both standards, inclusions are characterized by size, shape and concentration rather than chemical compositions. Although compositions are not identified, these two standards defined four most common types of inclusions, namely elongated sulfide, elongated alumina, elongated silicate, and globular oxides. Quantitative assessments were

performed using two different techniques. One is SEM equipped with EDX, and the other is OM equipped with Clemex CIR 5.0 software. This chapter will first present the results from quantification analysis using SEM-EDX technique. After that, quantification results using OM-Clemex CIR 5.0 software will be present. In the end, quantification results obtained from both evaluations will be compared.

4.5.1 Quantitative assessment of inclusions using SEM-EDX

As mentioned in Chapter 3, ten random 0.5 mm^2 rectangular field per specimen were examined under SEM at 2500X magnification. The inclusion data (i.e. shape, density, type, and size of inclusion) were recorded manually for each specimen. Due to the time consuming process, only Seamless L80-Mo and ERW L80-0.5Mo steels were examined using this method. Seamless L80-Mo is alloyed with Mn-Cr, and ERW L80-0.5Mo is alloed with Cr-Mo strategy. These two steels exhibit very different cracking behaviors in H_2S environment. As determined from the SSC proof ring test, Seamless L80-Mo (RAR=0.15) is more susceptible to SSC than ERW L80-0.5Mo (RAR=0.30). This chapter will evaluate if the inclusion affects the SSC susceptibility of these two steels.

The inclusions are characterized by inclusion content (in terms of inclusion density and severity levels), maximum inclusion size, and inclusion shape (%) and the results are present in Chapter 4.5.1.1-4.5.1.3.

4.5.1.1 Inclusion content

Figure 4.32 shows the inclusion density for different types of inclusions. According to ASTM E45 standard, the inclusion density of sulfide (elongated), alumina (elongated), and silicate (elongated) is measured as inclusion length (mm) per area (mm^2). For oxides, it was measured as the number of globular oxides per area (mm^2). The length was measured in SEM (accuracy:±2%). As shown in the figure, the inclusion density in Seamless L80-Mo is higher than

that of ERW L80-0.5Mo. For sulfide and alumina, the inclusion density is about two times higher in Seamless L80-Mo. Silicate and oxides inclusions are almost triple in inclusion density for Seamless L80-Mo in comparison to ERW L80-0.5Mo steel.

Table 4.3 shows the severity levels of inclusions. These severity values were determined from Table 3.2 using the measured inclusion density. As seen in the table, the severity values of sulfide, alumina, and silicate are half units higher in Seamless L80-Mo than ERW L80-0.5Mo. For oxides, the severity value of Seamless L80-Mo is two units higher than ERW L80-0.5Mo. These values will be compared with the results from OM-Clemex evaluation in next chapter.

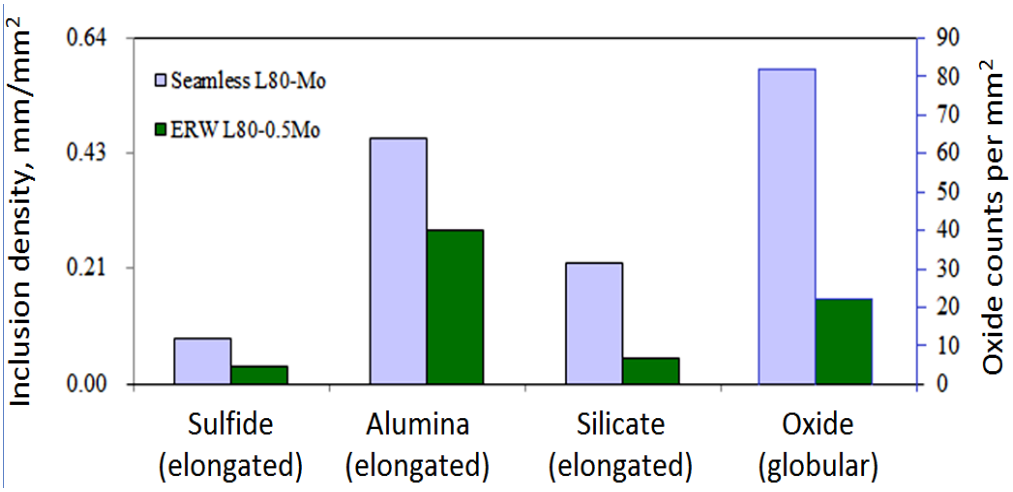

Figure 4.32: Inclusion density for Seamless L80-Mo and ERW L80-0.5Mo.

Table 4.3: Severity levels of inclusion for Seamless L80-Mo and ERW L80-0.5Mo.

	Sulfide	Alumina	Silicate	Oxides
Seamless L80-Mo	0.5	1.5	1	3.5
ERW L80-0.5Mo	0	1	0.5	1.5

4.5.1.2. Maximum inclusion size

Figure 4.33 shows the maximum length of inclusions for Seamless

L80-Mo and ERW L80-0.5Mo steel. The length was measured in SEM (accuracy:±4%). As shown in the figure, maximum inclusion length in Seamless L80-Mo is almost double in size compared with ERW L80-0.5Mo steel for all four types of inclusions.

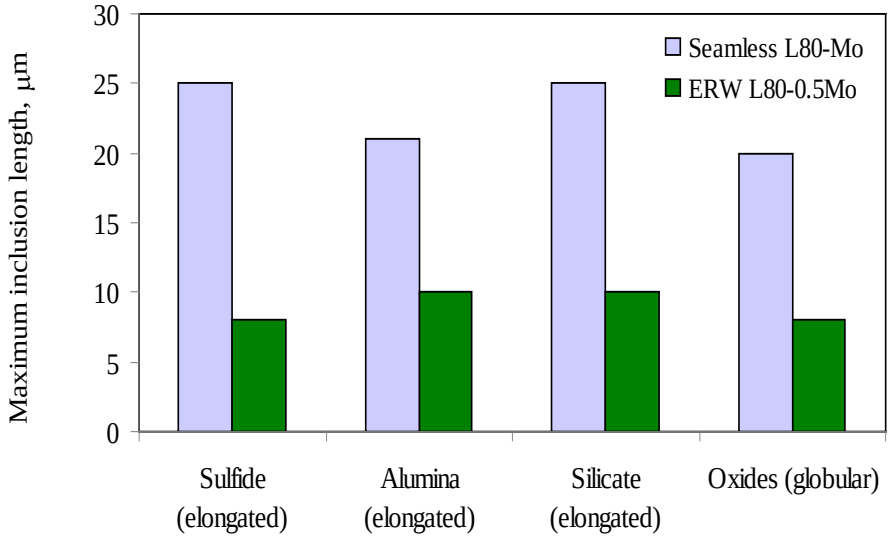

Figure 4.33: Maximum inclusion length for Seamless L80-Mo and ERW L80-0.5Mo.

4.5.1.3. Inclusion shape

Figure 4.34 shows the percentage of inclusion shape for Seamless L80-Mo and ERW L80-0.5Mo. This percentage is determined as the number of specific shape of inclusions divided by the total number of inclusions. As shown in the figure, the percentages of elongated, globular, and cubic inclusions are all higher for Seamless L80-steels.

In summary, Seamless L80-Mo has higher inclusion density, inclusion length, and percentage of different shapes of inclusions than ERW L80-0.5Mo steel. These results may be related to the higher SSC susceptibility of Seamless L80-Mo compared to ERW L80-0.5Mo. This will be compared with the results from OM-Clemex in Chapter 4.5.4.

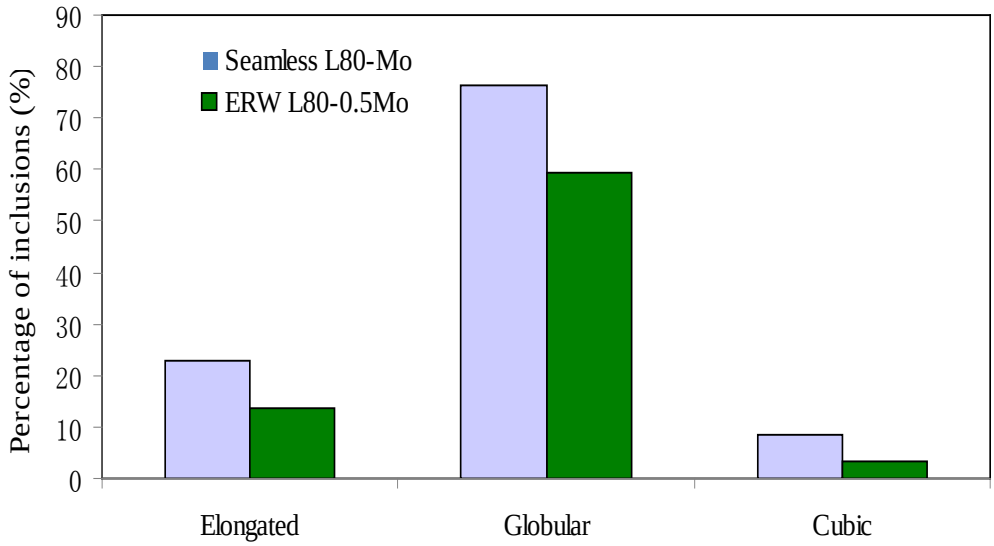

Figure 4.34: Percentage of inclusion shape for Seamless L80-Mo and ERW L80-0.5Mo steels.

4.5.2. Quantitative assessment of inclusions using OM-Clemex

Quantifications using OM-Clemex software were performed on all steels. A total of 320 microscopic fields per specimen were examined. The severity levels (ASTM E45 standard) and area fraction of inclusions (JIS G0555 standard) were determined automatically by Clemex. The following chapters 4.5.2.1-4.5.2.3 will present the characterization results on inclusion content (expressed by severity values), inclusion fractions and inclusion shape.

4.5.2.1. Inclusion content

Figures 4.35 and 4.36 show the severity level of inclusions for all steels. In addition to inclusion types, the inclusions were sub-divided into thin and heavy series by the software based on the width of the inclusions (as shown in Table 3.3). In Figure 4.35, it can be seen that oxides are higher in severity levels among all inclusion types for all steels. This is normal due to the formation of oxides from deoxidation. In general, the steels on the right of the figure (ERW L80-CrMo, ERW L80-B, HSLA 80-2, and ERW L80-0.5Mo)

showed a lower severity level. ERW L80-MnCr and ERW L80-0.5Mo has zero severity level for sulfide and silicate. ERW L80-CrMo has zero severity level for silicate. In Figure 4.36 for heavy series, oxides were observed for all steel with a severity level of 0.5 except for Seamless L80-Mo, which has a severity level of 1.0. Sulfide content with a severity level of 0.5 was also observed for Seamless L80-Mo. There were zero severity levels of alumina and silicates for all steels in heavy series. In both figures, the severity of zero does not mean the content of certain types of inclusion is zero. It should be noted that these values are the minimum length or number for each inclusion type. So when the severity level falls between two values, it is rounded down to the nearest whole or half units as specified by the ASTM E45-2005 standard. As a result, it is hard to make a conclusion from Figure 4.35 and 4.36 regarding the differences in inclusion contents between steels.

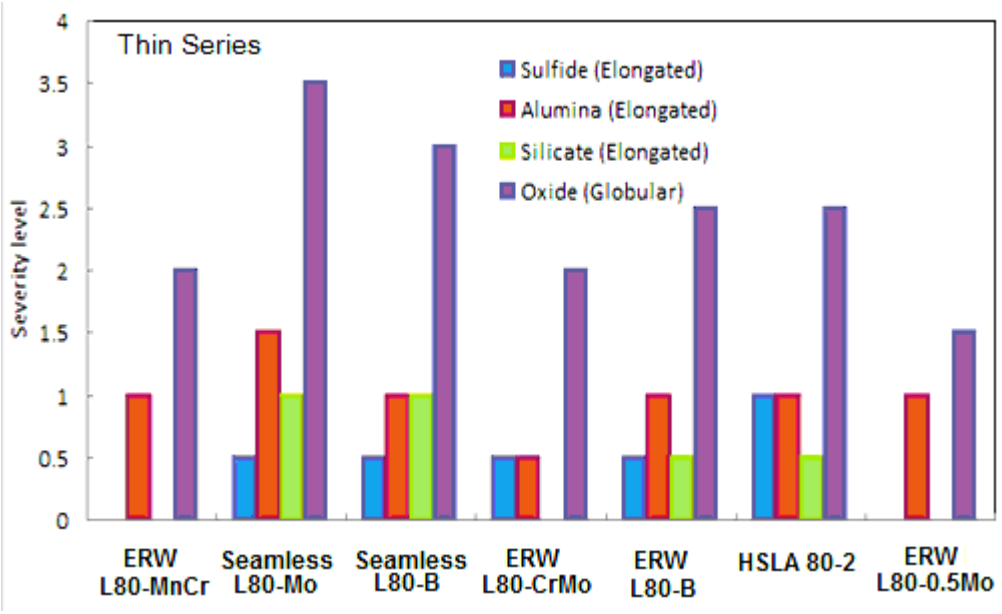

Figure 4.35: Thin series severity level of inclusions.

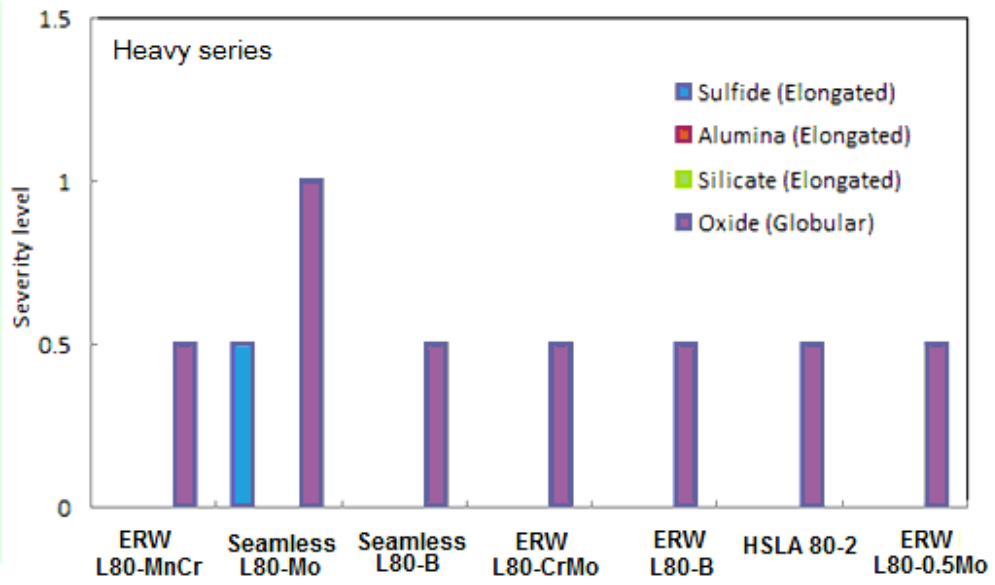

Figure 4.36: Heavy series severity level of inclusions.

4.5.2.2 Inclusion fraction

Figures 4.37 and 4.38 show the total inclusion fraction versus the SSC resistance in terms of RA ratio and time-to-failure from SSC test. The total inclusion fraction is the total area fraction of inclusions determined from all the microscopic fields by Clemex. As mentioned earlier in Chapter 3, the supplied casing steels can be divided into two main alloying strategic groups, one with Ti-B alloying and the other with Mn-Cr-Mo alloying. In Figure 4.37, it can be seen that there is no obvious relationship between RAR and inclusion fraction for all steels. But for steels within the same alloying group, RAR decreases as total inclusion fraction increases. Similarly in Figure 4.38, for the steels within the same alloying group, time to failure decreases as the total inclusion fraction increases. So the effect of inclusion fraction on SSC resistance is related to alloying composition of steels. The result after separation of alloying strategies is shown in Figures 4.39 and 4.40 for better illustration.

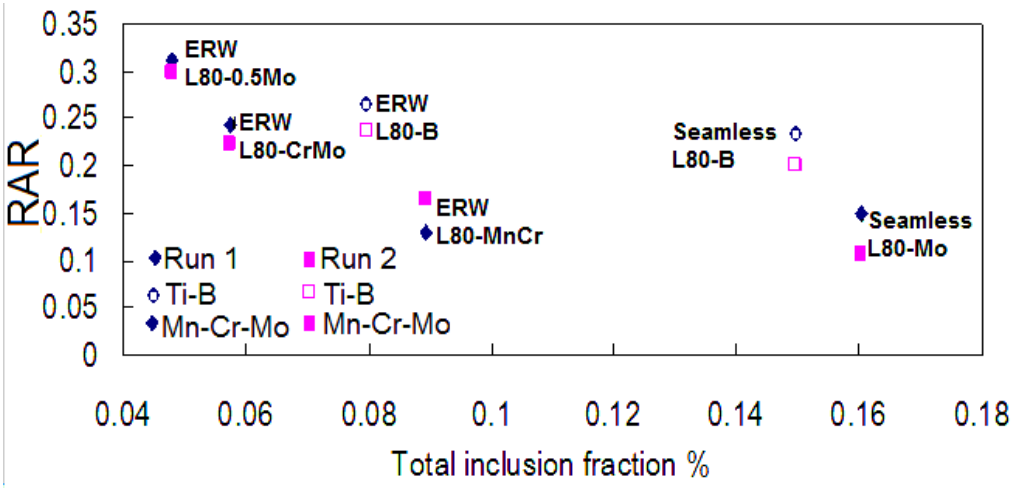

Figure 4.37: Total inclusions fraction % vs. RAR.

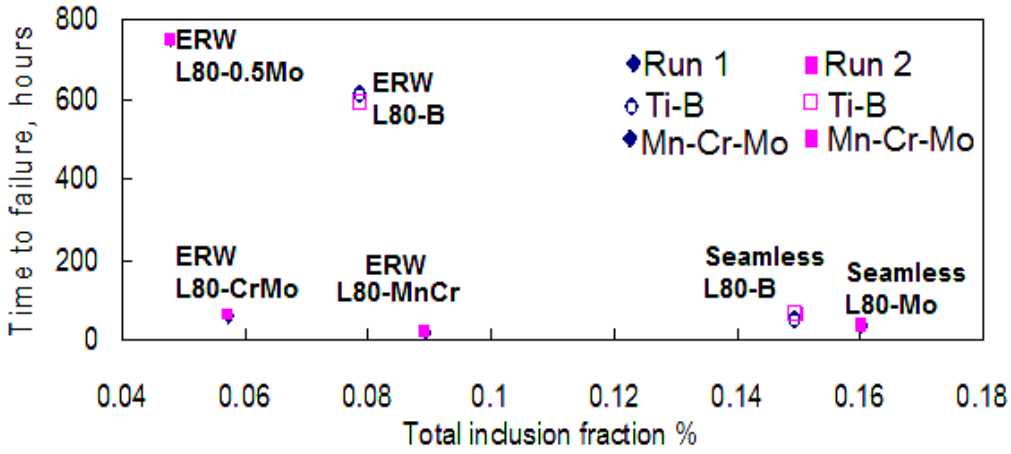

Figure 4.38: Total inclusions fraction % vs. time-to-failure.

Figure 4.39 shows the relationship between total inclusion area fraction and RAR for Mn-Cr-Mo steels (i.e. ERW L80-0.5Mo, ERW L80-CrMo, ERW L80- MnCr and Seamless L80-Mo). It can be seen that higher inclusion fraction results in lower RAR (i.e. lower SSC resistance). Figure 4.40 shows the relationship between total inclusion area fraction and RAR for Ti-B steels (i.e. ERW L80-B and Seamless L80-B). Similarly, the trend is that RAR decreases as total inclusion fraction increases. The SSC sensitivity of different alloying steels can be calculated from the slope of the linear relationship between total inclusion fraction and RAR. It was found that Mn-Cr-Mo steels had a sensitivity of -1.4 and Ti-B steels had a sensitivity of -0.12. The

Mn-Cr-Mo steels were more susceptible due to the presence of inclusions.

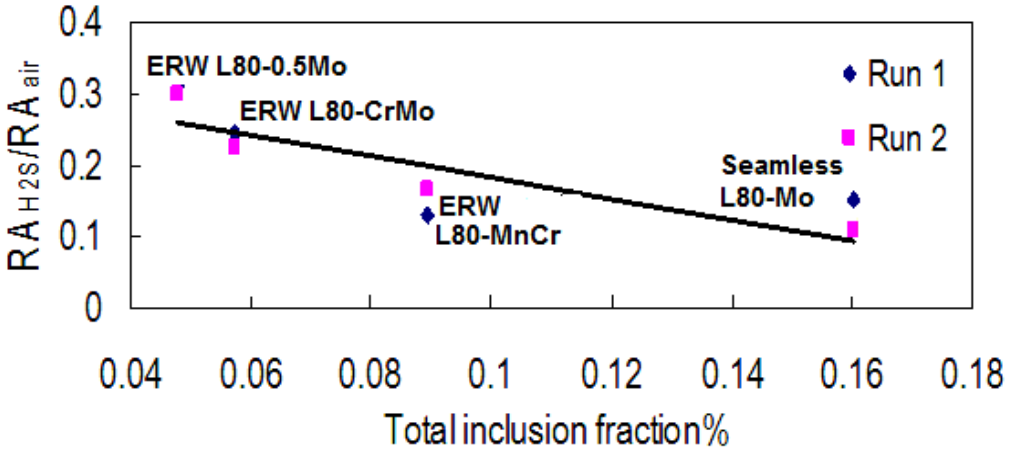

Figure 4.39: Total inclusions fraction % vs. RAR for Mn-Cr-Mo steels.

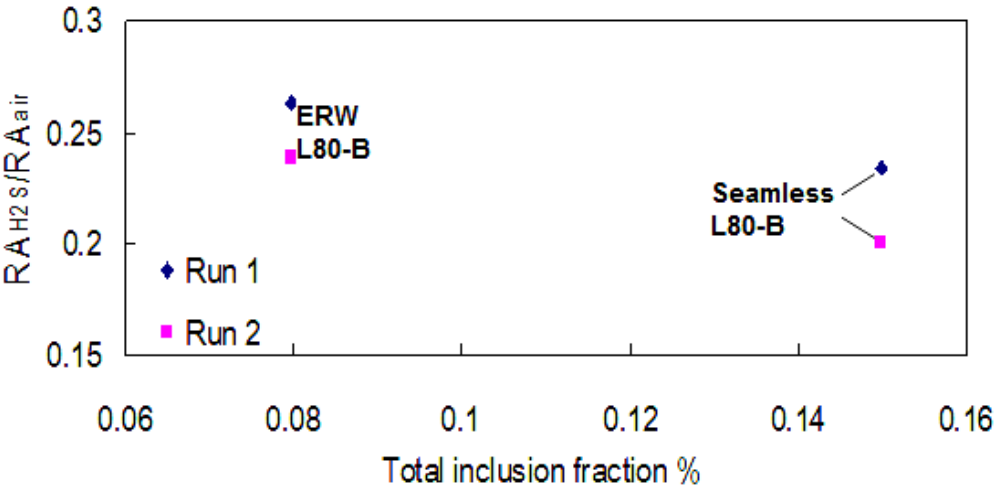

Figure 4.40: Total inclusions fraction % vs. RAR for Ti-B steels.

As mentioned in Chapter 3, the inclusions were categorized into four types, namely sulfide (elongated), alumina (elongated), silicate (elongated), and oxides (globular) as specified by ASTM E45 and JIS G0555 standard for quantification. These are the most common types of inclusions derived from

historical data collected on inclusions [62]. The effect of sulfide, alumina, silicate, and oxides on SSC resistance for Mn-Cr-Mo steels and Ti-B steels are shown in Figures 4.41-4.44 and Figures 4.45-4.48, respectively. For both Mn-Cr-Mo steels and Ti-B steels, the SSC resistance decrease as the sulfides, alumina, silicate and oxide fractions increase. Further discussion of the effect of inclusion type on SSC resistance is given in Chapter 5.

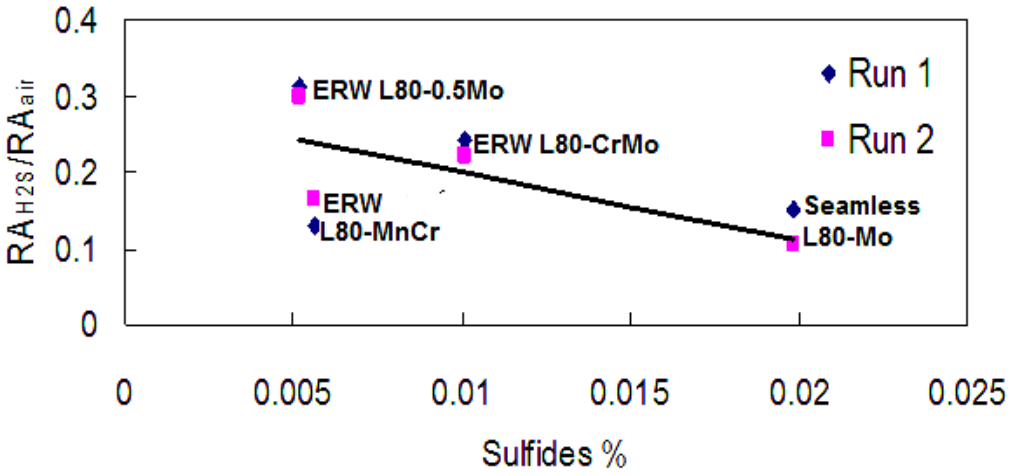

Figure 4.41: Effect of sulfide on SSC resistance for Mn-Cr-Mo steels.

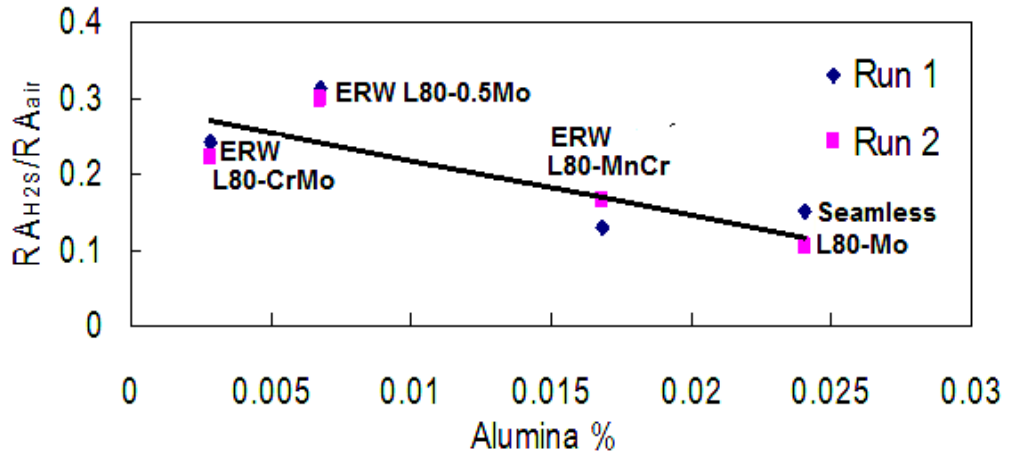

Figure 4.42: Effect of alumina on SSC resistance for Mn-Cr-Mo steels.

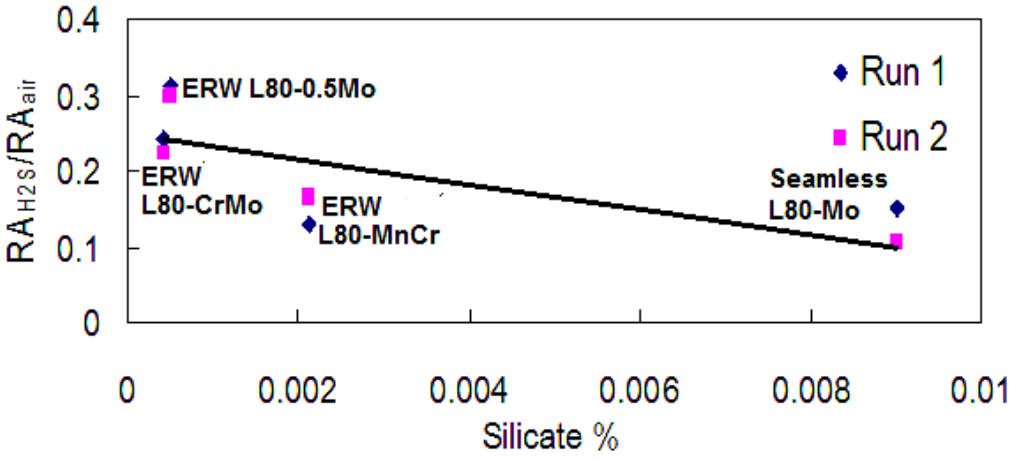

Figure 4.43: Effect of silicate on SSC resistance for Mn-Cr-Mo steels.

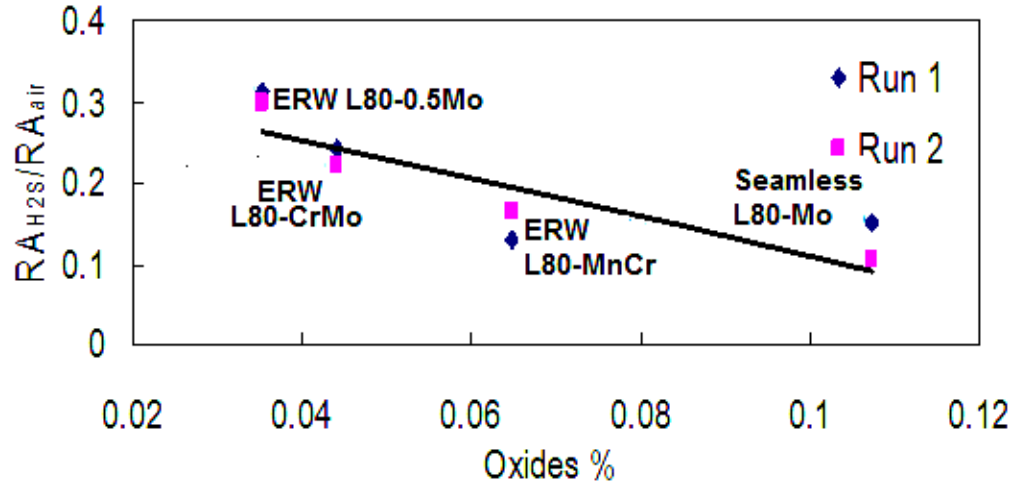

Figure 4.44: Effect of oxides on SSC resistance for Mn-Cr-Mo steels.

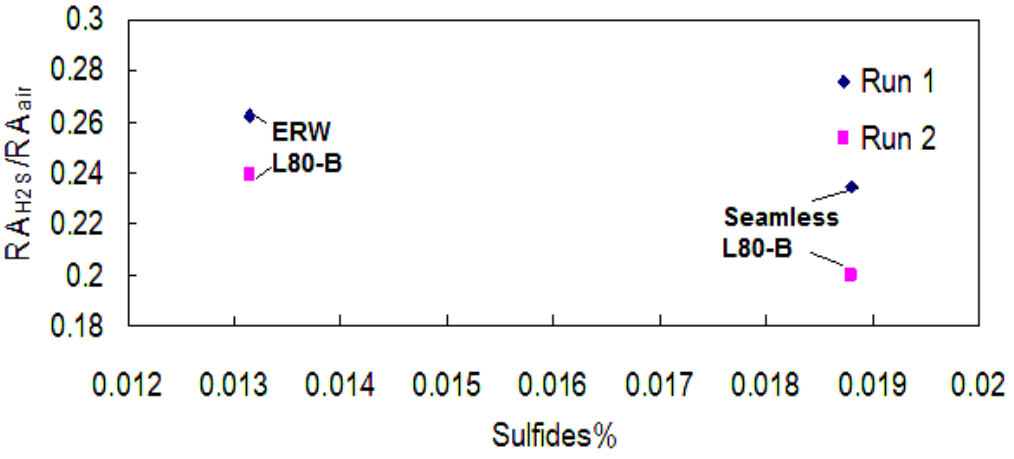

Figure 4.45: Effect of sulfide on SSC resistance for Ti-B steels.

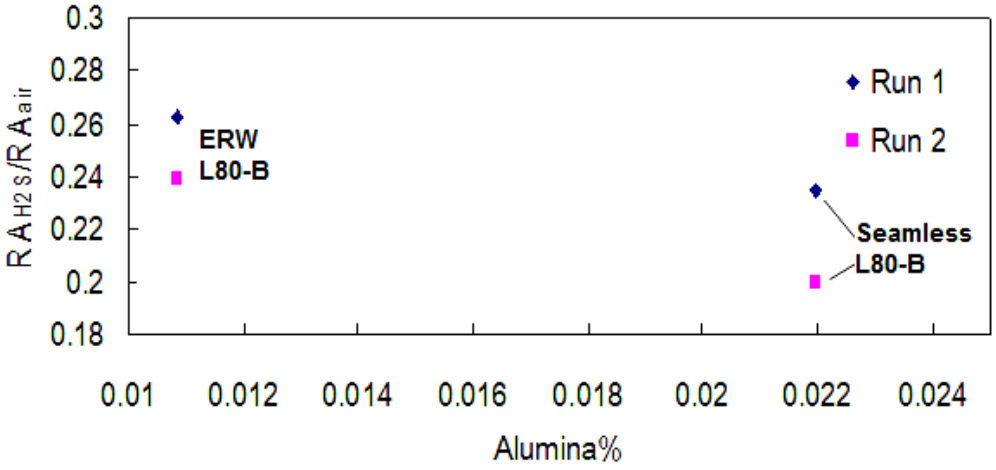

Figure 4.46: Effect of alumina on SSC resistance for Ti-B steels.

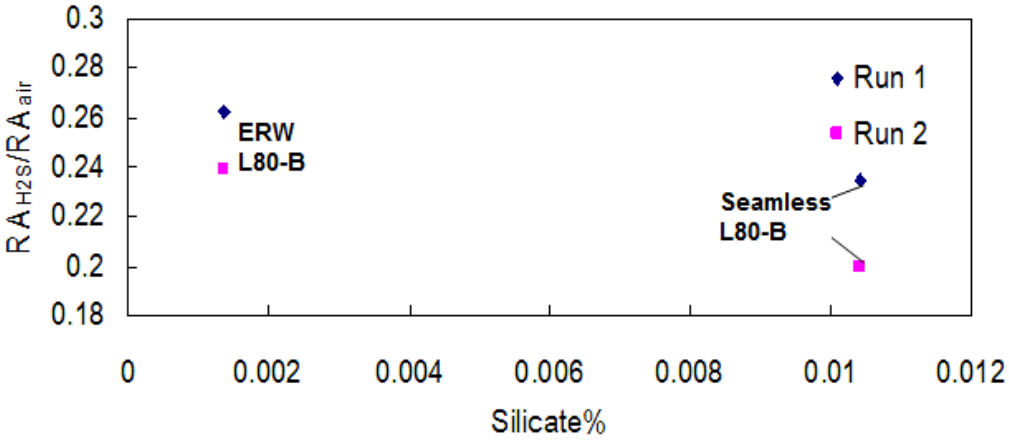

Figure 4.47: Effect of silicate on SSC resistance for Ti-B steels.

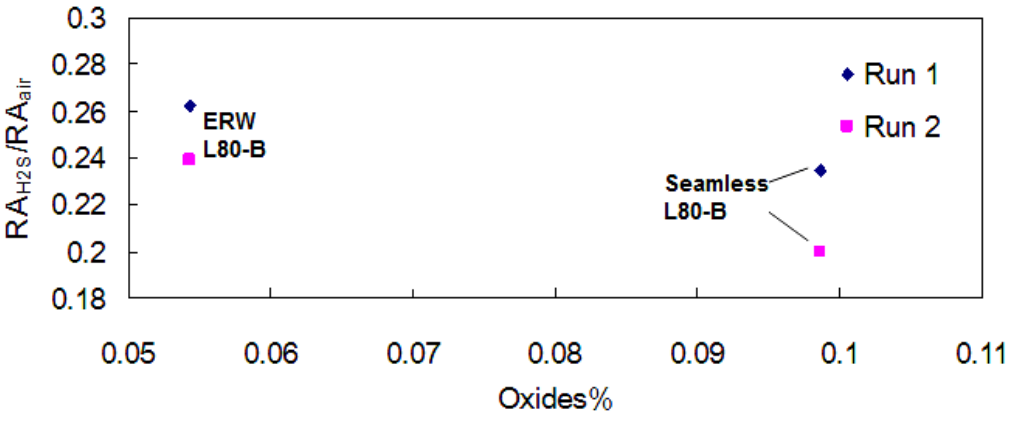

Figure 4.48: Effect of oxide on SSC resistance for Ti-B steels.

4.5.2.3. Inclusion shape

Inclusion shapes have strong effect on SSC resistance. A sharp interface with the matrix provides an ideal condition for easy crack propagation. Therefore, shape modification of inclusion is an effective way to improve cracking resistance. Calcium is usually added to the steels to modify the shape of soft, ductile MnS stringers inclusions into globular CaS particles which do not elongate during rolling. Figure 4.49 shows the total area fraction of different shapes of inclusions in the steels. As shown in the Figure, the fraction of globular inclusions is higher than the fraction of elongated inclusions for all steels. This is because all the steels contain more globular oxide inclusions than other elongated type of inclusions (i.e. elongated sulfide, elongated alumina, elongated silicate) as previously shown in Figures 4.41-4.48. In addition, the steels have been calcium treated to modify the shape of elongated sulfide stringers into globular shape (Figure 4.50 and Figure 4.51).

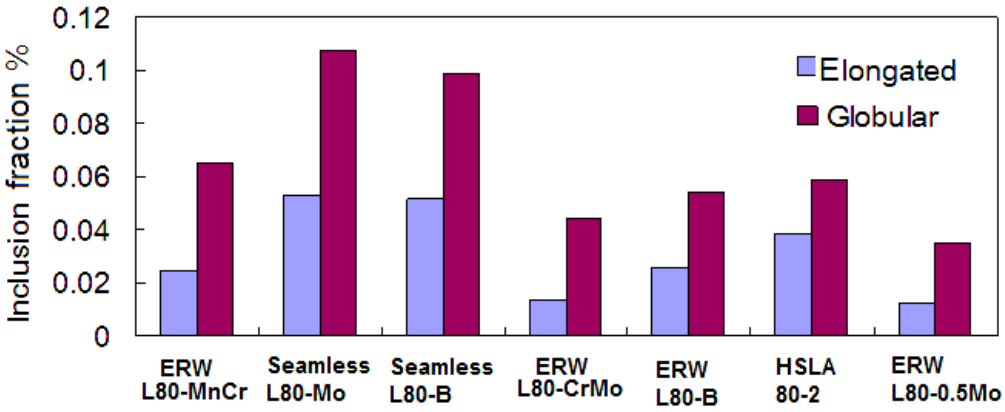

Figure 4.49: Fraction of inclusions with different shapes in the steels.

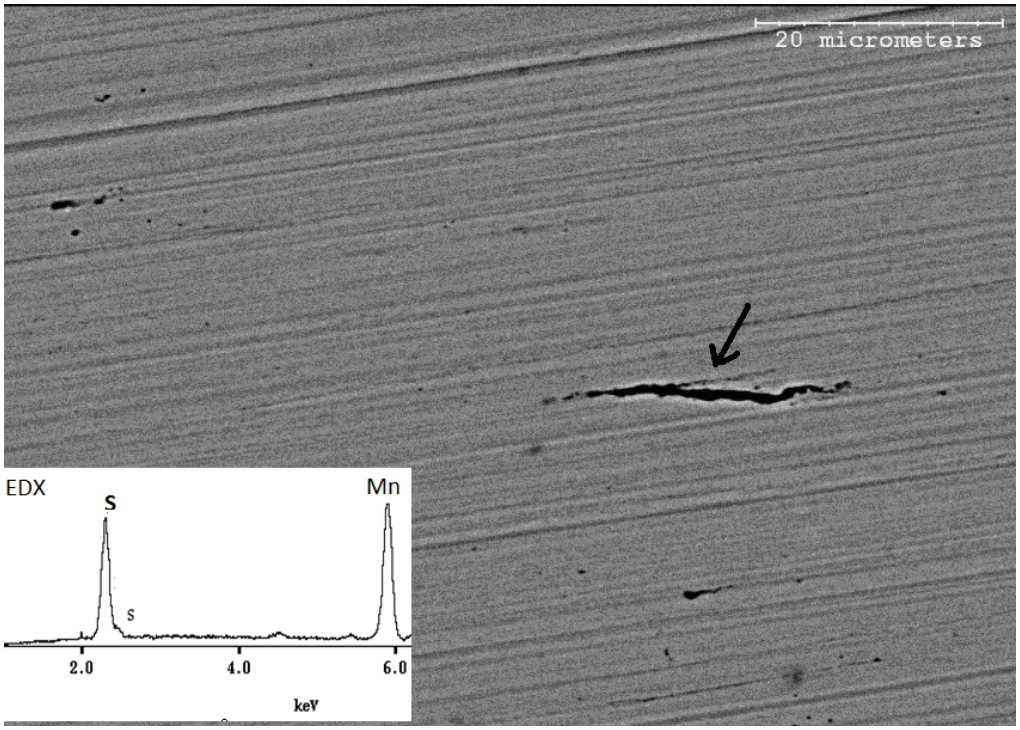

Figure 4.50: SEM image of elongated MnS inclusions in Seamless L80-B. Composition was determined by EDX.

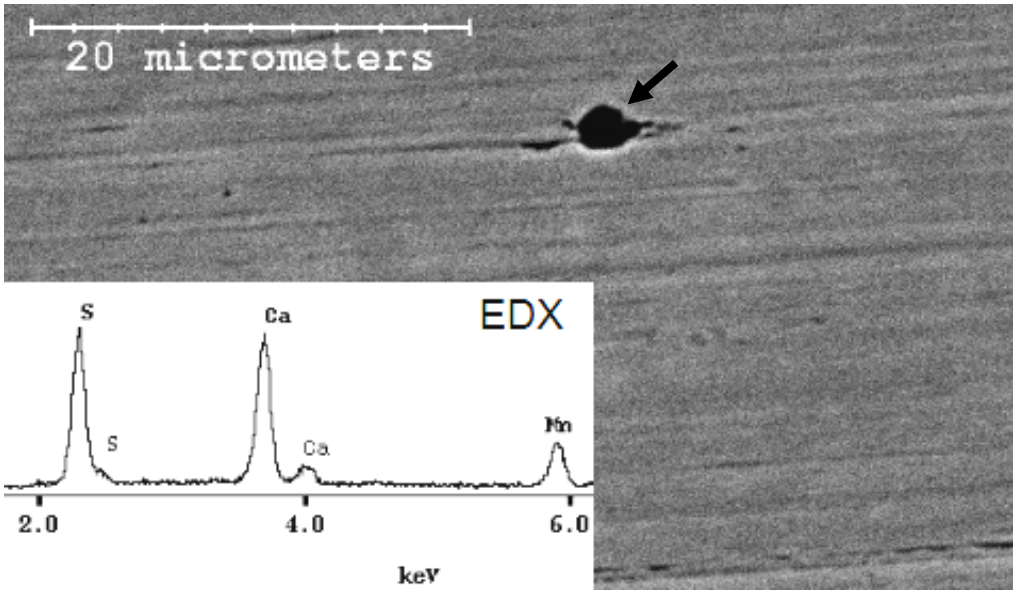

Figure 4.51: SEM image of Ca-modified MnS inclusion in ERW L80-0.5Mo. Composition was determined by EDX.

Figure 4.52 and 4.53 compares the effect of elongated and globular inclusions on SSC resistance for Mn-Cr-Mo steels, respectively. As seen in both figures, RAR decreases as the fraction of elongated and globular

inclusions increases. Similar trends of relationship between inclusion shapes and RAR were observed in Figure 4.54 and 4.55 for Ti-B steels. Both the elongated and globular shape inclusions have shown adverse effects on SSC resistance for both Mn-Cr-Mo steels and Ti-B steels. Further discussion on the effect of inclusion shape is given in chapter 5.

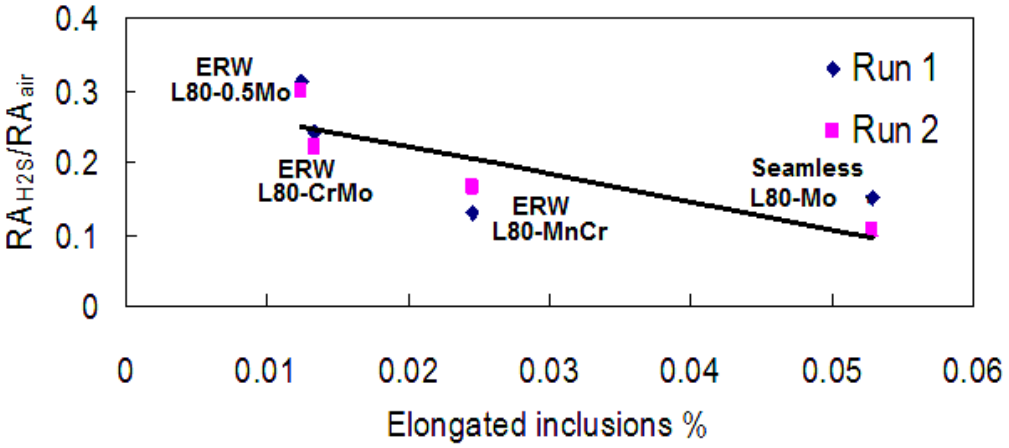

Figure 4.52: Effect of elongated inclusions on SSC resistance for Mn-Cr-Mo alloyed steels.

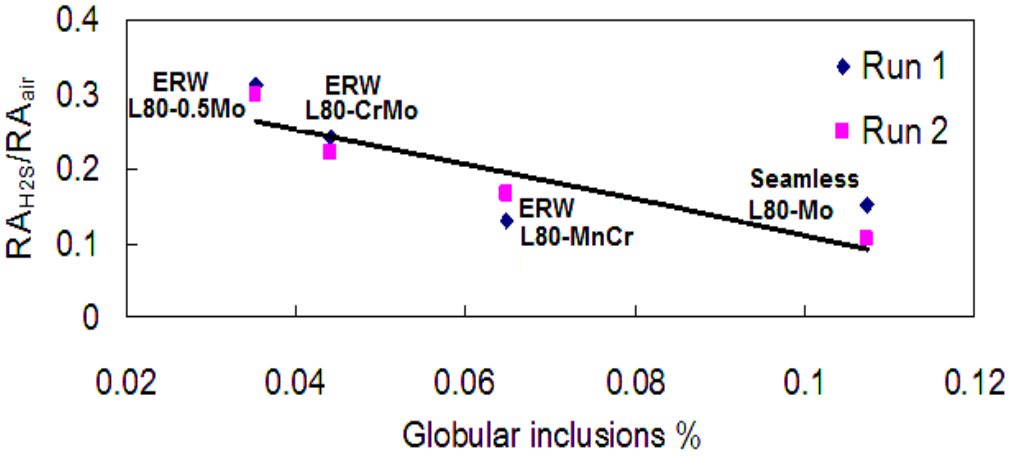

Figure 4.53: Effect of globular inclusions on SSC resistance for Mn-Cr-Mo alloyed steels.

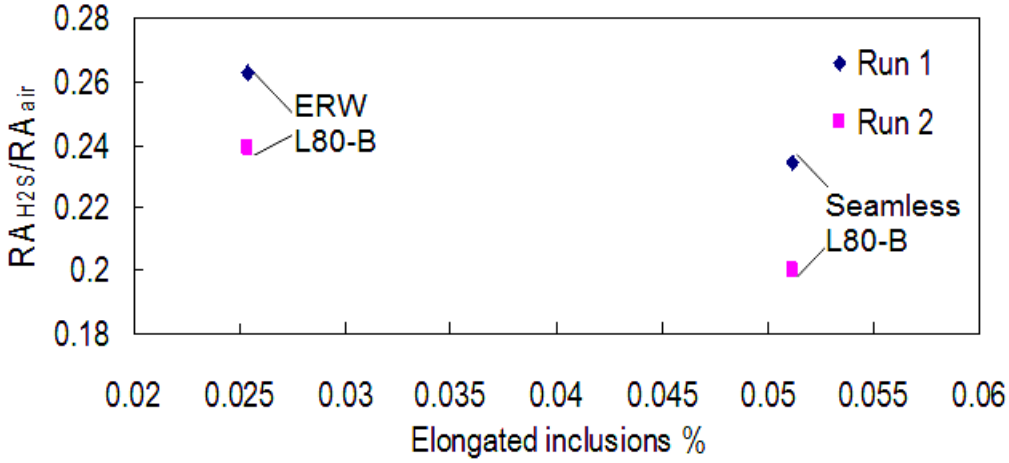

Figure 4.54: Effect of elongated inclusions on SSC resistance for Ti-B alloyed steels.

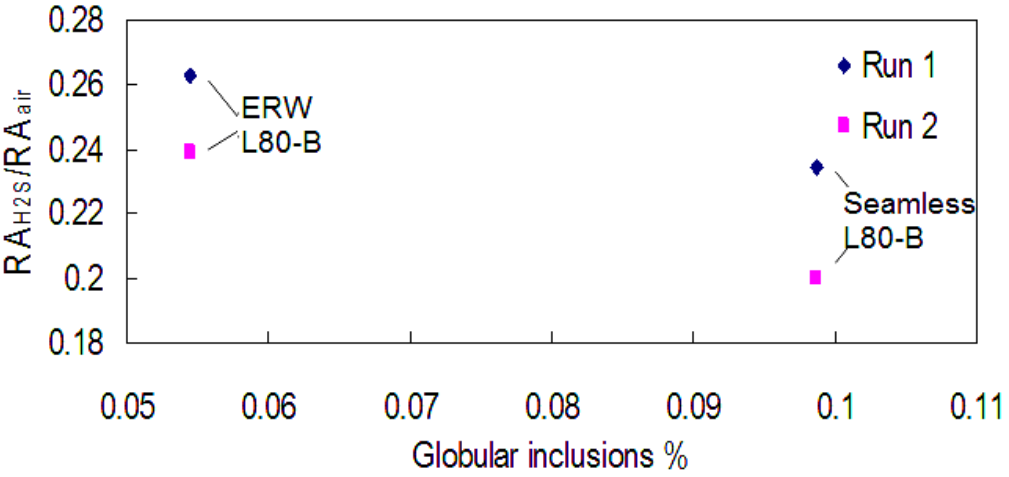

Figure 4.55: Effect of globular inclusions on SSC resistance for Ti-B alloyed steels.

4.5.3. Clustering of inclusions

Clustering of inclusions was examined qualitatively by SEM. Clustering of inclusions was observed in Seamless L80-Mo, Seamless L80-B, ERW L80-MnCr, and HSLA 80-2 steels. No clustering was observed in ERW L80-B and ERW L80-0.5Mo. Figures 4.56-4.58 show the SEM images of inclusion clusters found in the steels. The composition of the inclusion was determined by EDX. The clustering site was consisted of TiN and Ca-Al-O-S enriched inclusions in Figure 4.56. In Figure 4.57, the clustering site consisted of MnS

and TiN. In Figure 4.58, cracking was observed from a large broken alumina inclusion in ERW L80-MnCr steel even before SSC test. More clusters were observed at the centreline of the steel thickness which is likely caused by segregation during casting. These clustering sites have a size of ~30µm and are believed to be very detrimental for SSC resistance. Further discussion on effect of inclusion clustering is given in chapter 5.

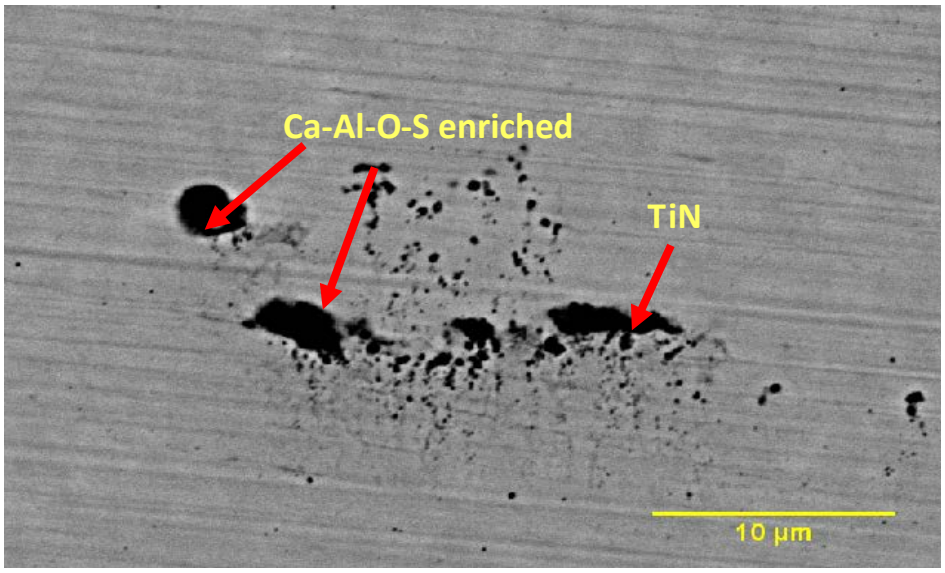

Figure 4.56: Clustering of inclusions at centerline location in Seamless L80-B steel. The composition of inclusion was determined by EDX.

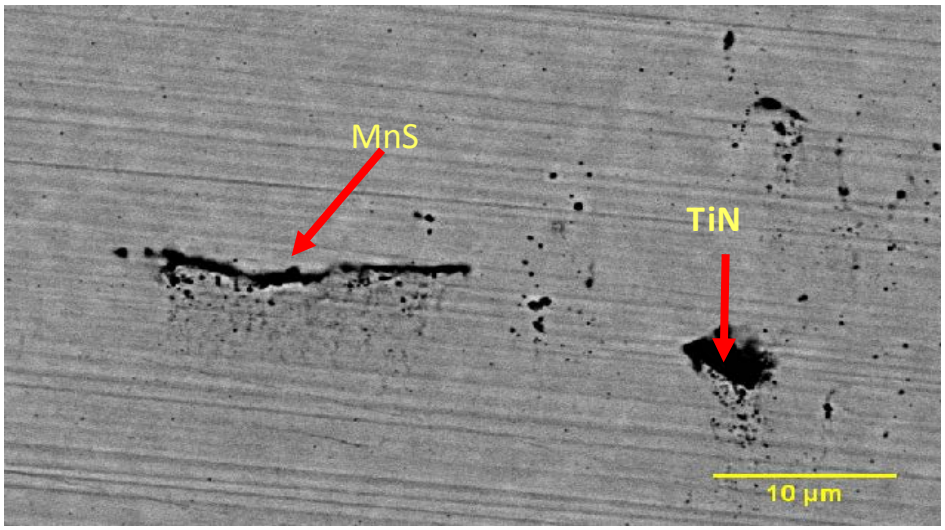

Figure 4.57: Clustering of inclusions at centerline location in Seamless L80-B steel. The composition of inclusion was determined by EDX.

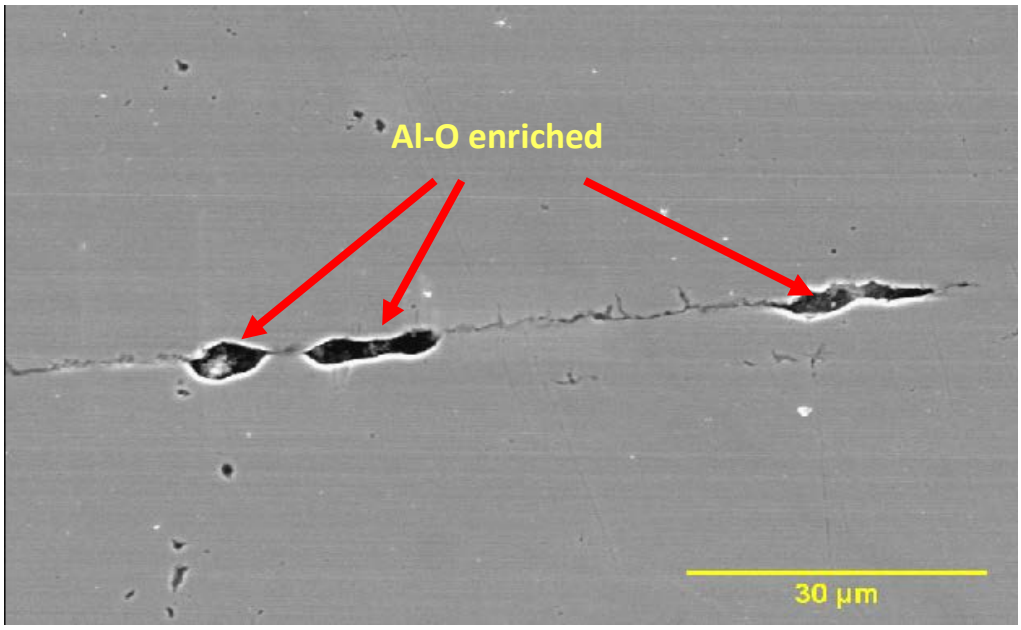

Figure 4.58: Clustering of inclusions at centerline location in ERW L80-MnCr steel. The composition of inclusion was determined by EDX.

4.5.4. Comparison of the quantification results from SEM and Clemex assessment

In previous chapters, characterization results of inclusions using SEM-EDX method and OM-Clemex method were present. For comparison purpose, results of Seamless L80-Mo and ERW L80-0.5Mo steels were used because SEM only evaluated these two steels. Both examination methods have revealed different information on inclusions. Table 4.4 summarizes the inclusion results of these two steels obtained from different examination methods. Inclusion density, severity values, and fraction % of inclusion shape were evaluated by SEM. Compositions of inclusion were determined by EDX. Clemex method was used to evaluate the severity value, fraction of different types of inclusion, and area fraction % of inclusion shape.

As determined from SSC test, these two steels have exhibited different SSC performance though they are both Mn-Cr-Mo alloyed steels. Seamless L80-Mo has shown to be more SSC susceptible (in terms of RAR and time-to-failure) than ERW L80-0.5Mo. From SEM and Clemex examination, Seamless L80-Mo has significantly higher inclusion density, inclusion fraction,

and inclusion length than ERW L80-0.5Mo steels, for all four types of inclusions. The severity value based on inclusion density from both examinations is quite consistent for both steels. The only difference is the severity value of silicate for ERW L80-0.5Mo steel. SEM revealed a half unit higher value than Clemex result. This difference is reasonable because SEM only examined 10 random microscopic fields of data while Clemex examined 320 microscopic fields. The difference in sampling volume of the two examination methods may result in differences in measurement of silicate contents.

The fraction % of inclusion shape was significantly different from these two examination methods. The fraction of inclusion shape was significantly smaller from Clemex results. But it should be noted that the fraction % of inclusion shape is defined differently in these two examinations. For Clemex assessment, the fraction % was the area fraction of inclusions in all microscopic fields. For SEM assessment, this fraction % was defined as the number of certain type of inclusion to total inclusions. So the fraction% of inclusion shape from Clemex was significantly smaller. From both examination methods, the fractions of elongated and globular inclusions were higher for Seamless L80-Mo steel. Clustering of inclusion was observed in Seamless L80-Mo but not in ERW L80-0.5Mo steel.

In summary, comparing the results from SEM and Clemex methods, they give different values of measurements but the same trends. Further discussion of the effect of inclusions is given in Chapter 5.

Table 4.4: Summary of inclusion results for Seamless L80-Mo and ERW L80-0.5Mo.

	Seamless L80-Mo		ERW L80-0.5Mo	
Pass/Fail	Fail		Pass	
RAR	0.15		0.3	
Time-to-failure (hour)	32		>720	
Inclusion density by SEM (mm/mm^2 or oxide $count/mm^2$)				
Sulfide	0.09		0.03	
Alumina	0.5		0.3	
Silicate	0.2		0.05	
Oxide	82		22	
Severity level				
	SEM	Clemex	SEM	Clemex
Sulfide	0.5	0.5	0	0
Alumina	1.5	1.5	1	1
Silicate	1	1	0.5	0
Oxide	3.5	3.5	1.5	1.5
Inclusion fraction% by Clemex				
Sulfide	0.02		0.005	
Alumina	0.02		0.007	
Silicate	0.009		0.0005	
Oxide	0.1		0.04	
Maximum inclusion length or diameter by SEM, μm				
Sulfide	25		8	
Alumina	21		10	
Silicate	28		10	
Oxide	20		6	
Fraction % of different inclusion shape				
	SEM	Clemex	SEM	Clemex
Elongated	23	0.053	14	0.012
Globular	76	0.11	59	0.035
Centerline clustering?	Yes		No	

4.6. Characterization of carbides

Characterization of carbides has been performed by Image analysis software (ImageJ 1.46) on ERW L80-0.5Mo, Seamless L80-Mo, ERW L80-B, and Seamless L80-B. These steels were chosen because they represent different alloying strategies. ERW L80-0.5Mo and Seamless L80-Mo are alloyed with Mn-Cr-Mo, while ERW L80-B and Seamless L80-B are alloyed with Ti-B steels. Mn-Cr-Mo alloying and Ti-B alloying are the two main alloying strategies for the supplied materials that have been mentioned in Chapter 3.

4.6.1. The effect of carbide shapes on SSC resistance

Figures 4.59 to 4.62 show the effect of carbide shape on SSC resistance. In terms of both RAR and time to failure used to measure SSC resistance, higher fraction of elongated carbides lead to lower cracking resistance; inversely, higher fraction of globular carbides results in higher cracking resistance. Further discussion on the effect of carbide shape is given in Chapter 5.

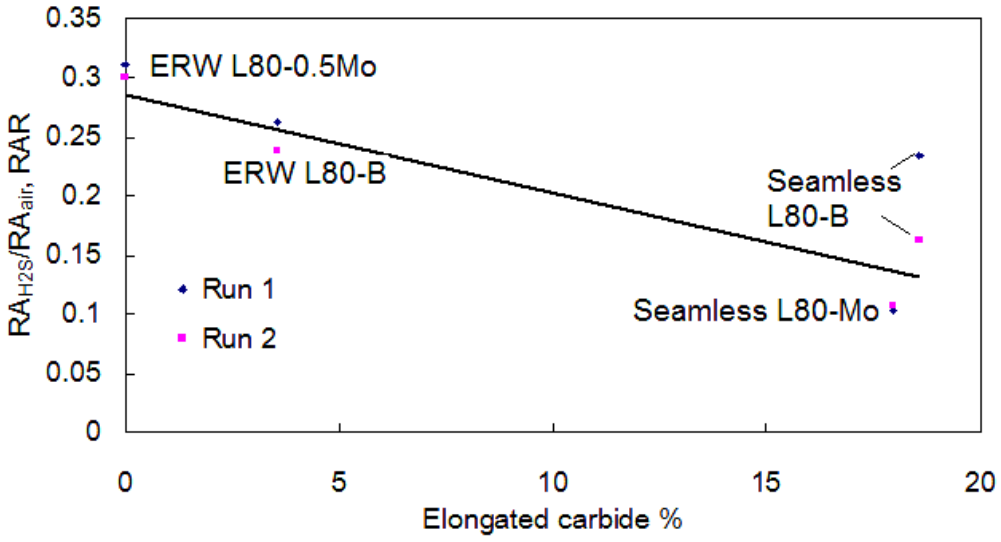

Figure 4.59: The effect of elongated carbide on RAR.

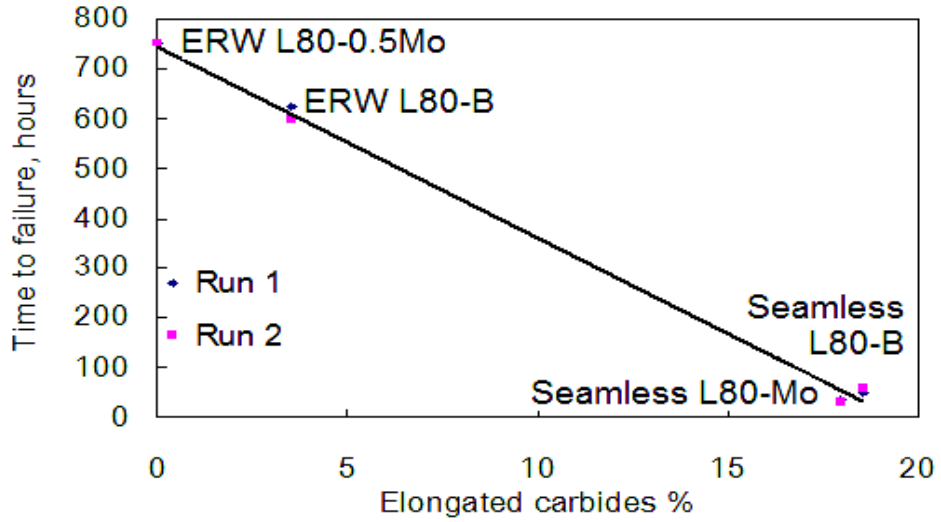

Figure 4.60: The effect of elongated carbide on time to failure.

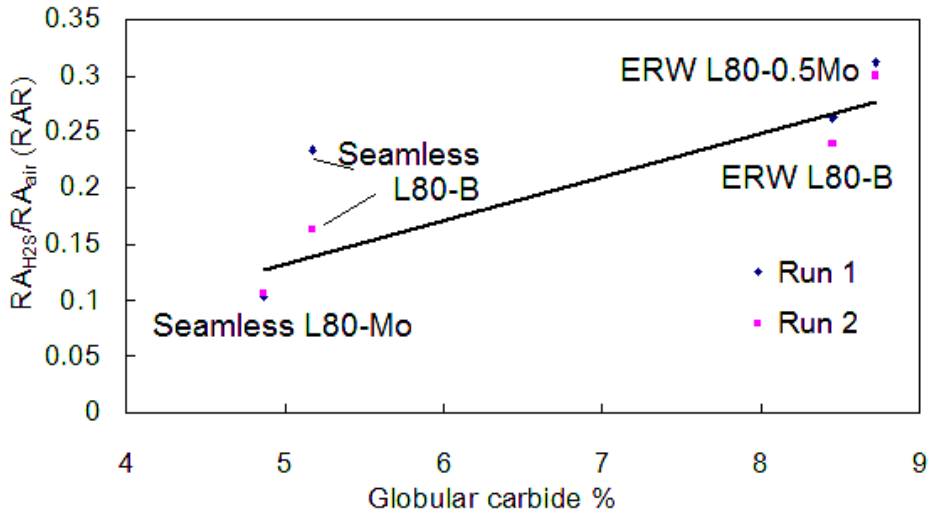

Figure 4.61: The effect of globular carbides on RAR.

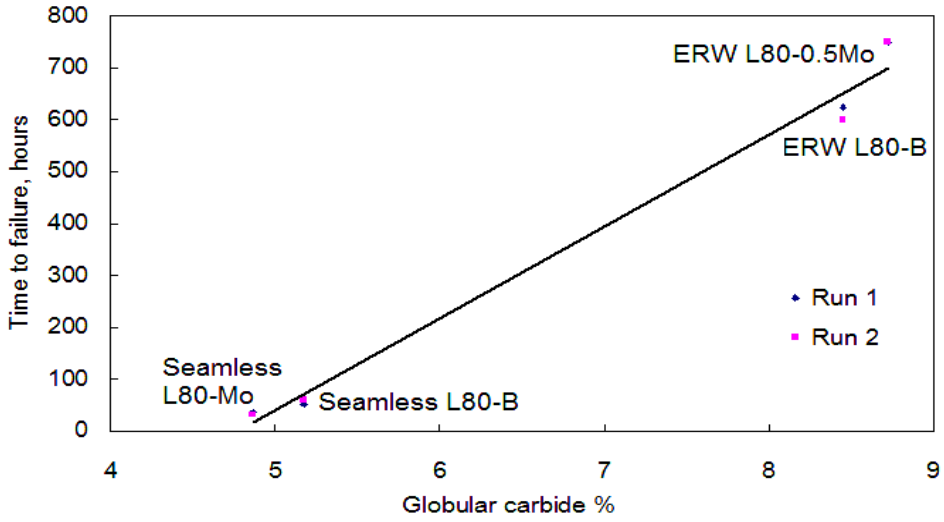

Figure 4.62: The effect of globular carbides on time to failure.

Auger Electron Spectrometer was used to determine the type of carbides in the steels. All carbides in the steels have been identified as iron carbides (cementite). For ERW L80-0.5Mo, molybdenum carbides are also observed. Figure 4.63 shows a SEM image of molybdenum carbide, as indicated by particle A. The molybdenum carbide has a globular shape. Figure 4.64 is the Auger spectrum of molybdenum carbides. It shows that particle A in Figure 4.63 is consisted of Mo and C. The Auger spectrum of the background (indicated by B in Figure 4.63) is shown in Figure 4.65, in which Mo is not detected.

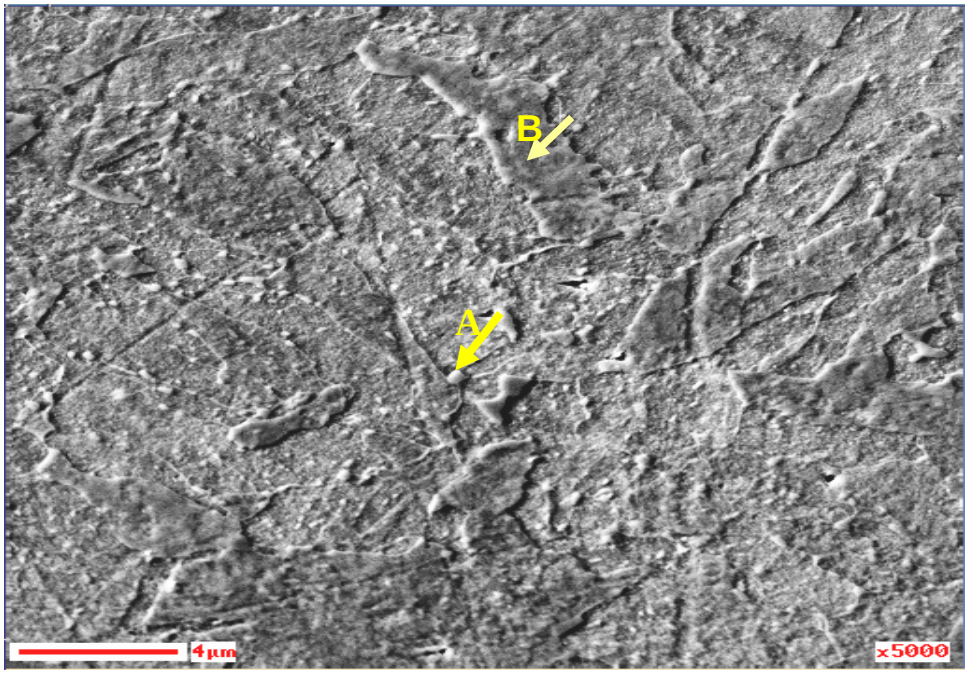

Figure 4.63: SEM image for globular molybdenum carbides (particle A) in ERW L80-0.5Mo steel. “B” represents the background for comparison.

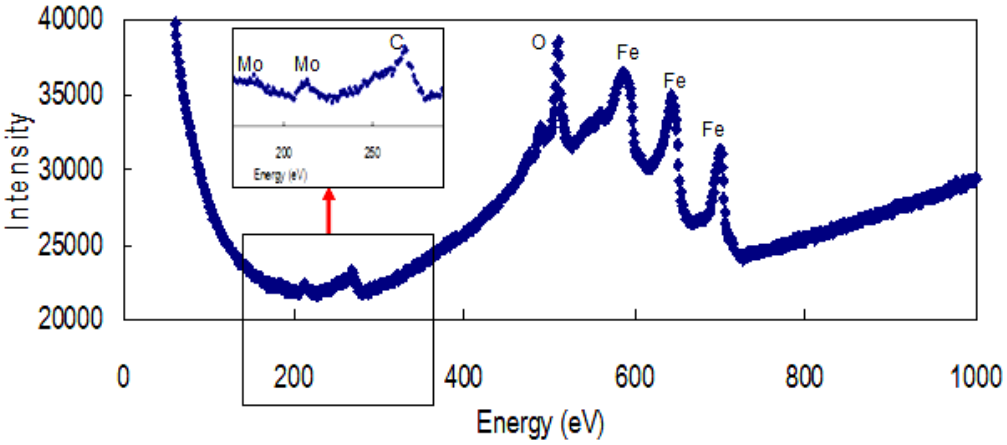

Figure 4.64: Auger spectrum for particle A in Figure 4.63.

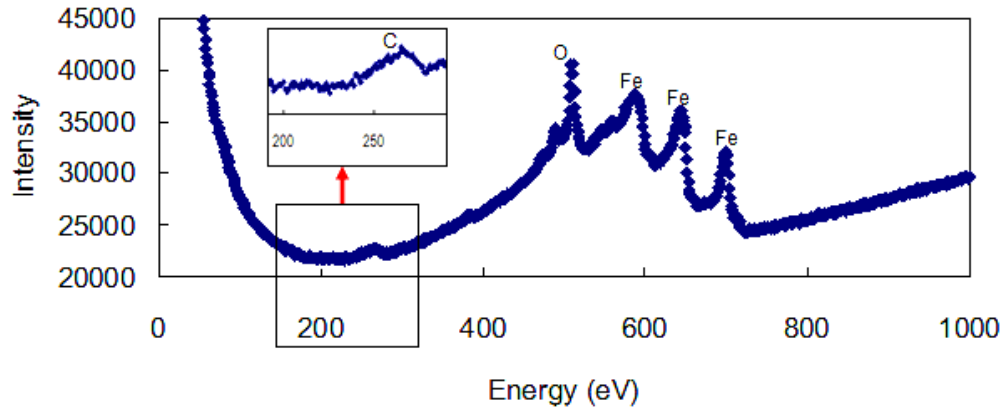

Figure 4.65: Auger spectrum for background B in Figure 4.63.

Figures 4.66 shows a SEM image of the different shapes of carbides in HSLA 80-2 steel. In this figure, both elongated and globular carbides are observed. The elongated carbides (as indicated by A in the figure) are nucleated as a cluster in the matrix. The globular carbide is indicated by G in the figure. Figures 4.67, 4.68, and 4.69 are the Auger spectra for particle A, background, and particle G in Figure 4.66, respectively. As can be seen from the Auger spectra, both elongated carbide (A) and globular carbide (G) are consisted of Fe and C. These carbides are believed to be cementite despite of their different shapes.

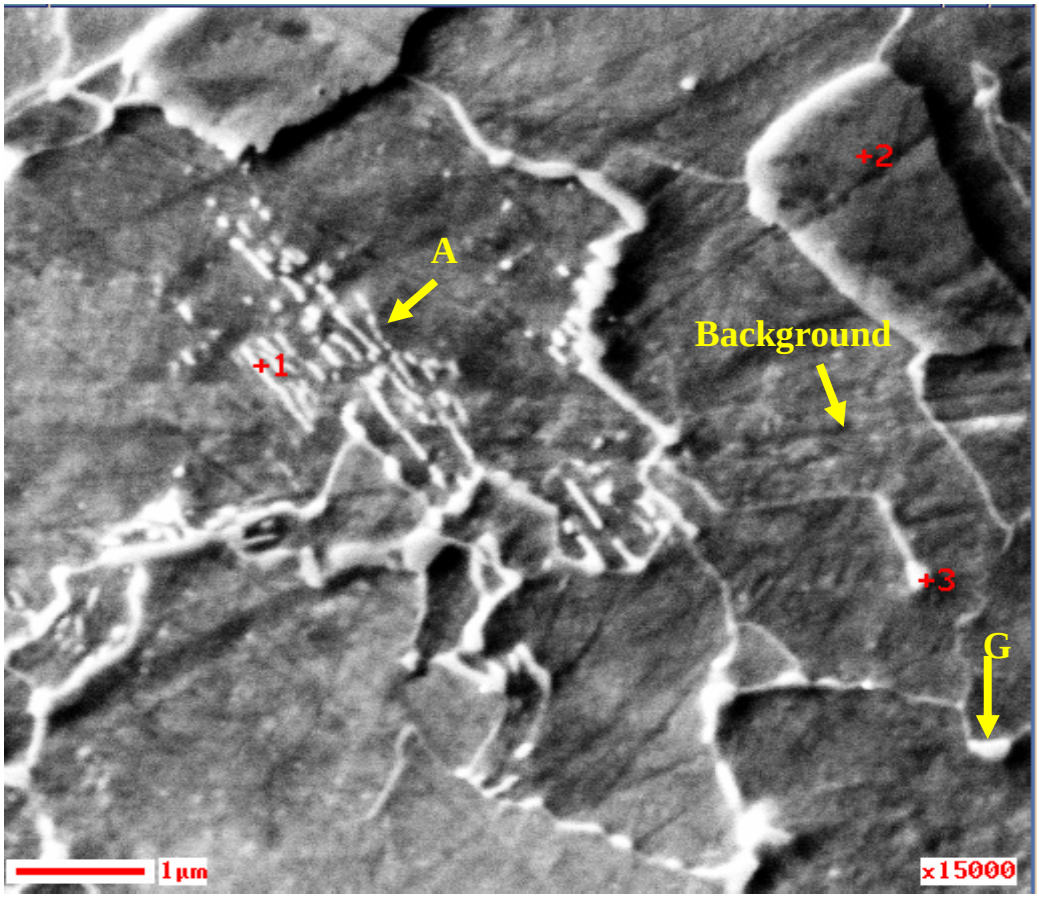

Figure 4.66: SEM image showing different morphologies of carbides in HSLA 80-2.

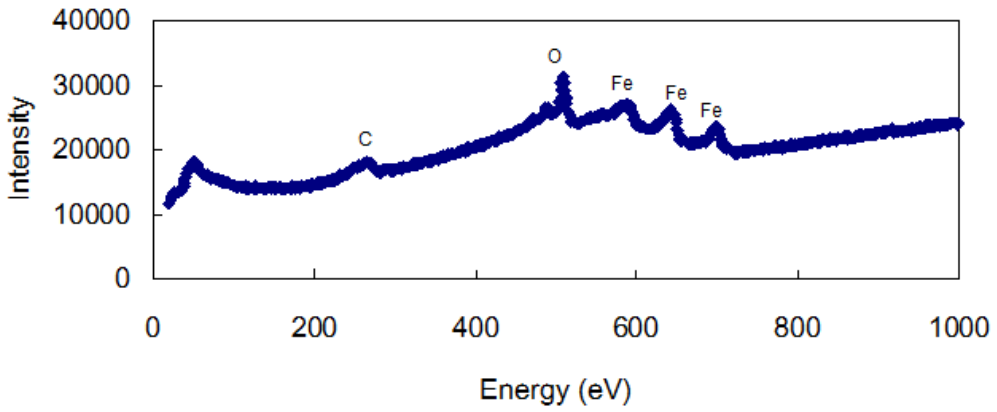

Figure 4.67: Auger spectrum for particle A in Figure 4.66.

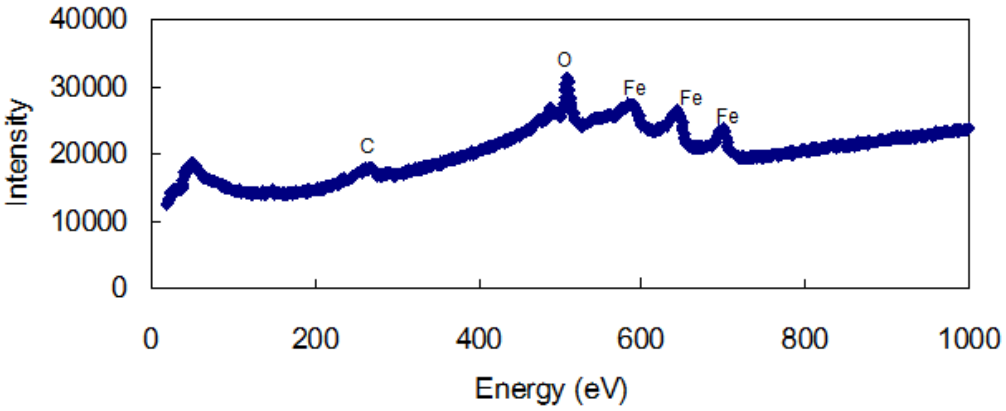

Figure 4.68: Auger spectrum for background in Figure 4.66.

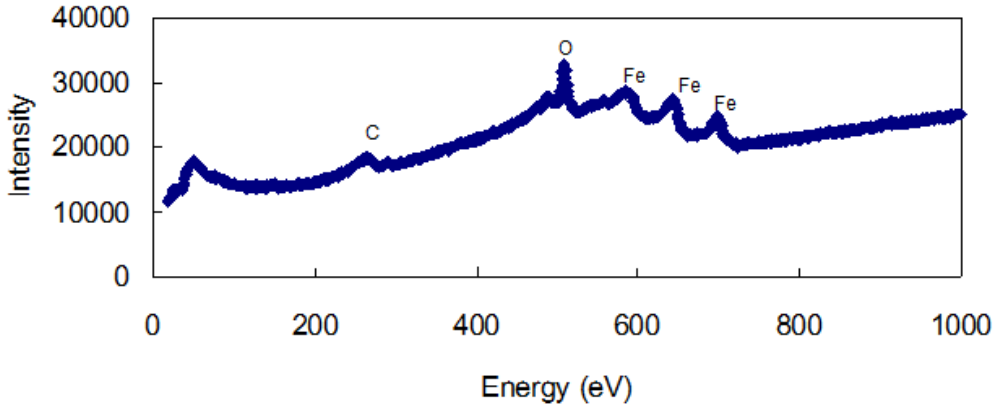

Figure 4.69: Auger spectrum for particle G in Figure 4.66.

5. DISCUSSIONS

The previous chapter has presented the SSC results from both proof ring and SSRT test, quantification results of inclusion using both SEM-EDX and OM-Clemex methods, and characterization of carbide shapes using image analysis. This chapter is focused on determining the mechanism and dominant factor for the SSC cracking behaviours of the investigated steels. Firstly, the SSC results are discussed. Secondly, a discussion of the effect of inclusion, carbide shape, alloying elements on SSC resistance is given. Finally, the dominant metallurgical factor for SSC behaviours is discussed.

5.1 Verification of test results

The SSC susceptibility of steels was evaluated using both constant load test (proof ring) and SSRT test. The constant load test is a conventional method for SSC evaluation using smooth tensile specimen. SSRT is not usually used for SSC evaluation but is attracting more researchers to use it recently because it can give a quick assessment. Specimens of the same dimension and orientation were used in both tests. Specimens were machined at 90 degree position from the weld seam or 0 degree (for seamless steel) in the longitudinal axis of the tube. The constant load test is used as the main test for SSC assessment in this study. SSRT test is used to compare and verify the results from the proof ring test. For the proof ring test, two experimental runs for each steel were conducted at exactly the same test conditions (i.e. applied load, test solution, specimen preparation) to confirm the reproducibility of the results. The results are considered to be reproducible if they are within 15% of each other. As previously shown in Table 4.2 in Chapter 4, all proof ring test results satisfy this criterion. The SSC results in terms of time-to-failure and RAR are consistent for both experimental runs. SSRT tests were performed on ERW L80-MnCr, Seamless L80-B, and ERW L80-0.5Mo steels. These three steels represent the different alloying strategies (i.e. Mn-Cr, Ti-B, and Cr-Mo alloying). SSRT results also showed the same tendency for SSC resistance of

the three steels in terms of time-to-failure, total strain to failure, fracture stress, and stress-strain behaviours (Chapter 4.4).

Quantification of inclusions was performed using SEM-EDX and OM-Clemex methods. SEM-EDX quantifications were conducted on two steels, namely Seamless L80-Mo and ERW L80-0.5Mo. OM-Clemex quantifications were conducted for all steels. Dimension (i.e. 160mm^2 test area) and orientation of the specimens are the same for both examination methods. The specimens were taken from a position of 90 degree from the weld seam or 0 degree (for seamless steel) in the longitudinal axis of the tube (Figure 3.9). The SEM method is used to complement and verify the results from Clemex measurements. Comparisons of the quantification results of Seamless L80-Mo and ERW L80-0.5Mo from both methods were shown in Table 4.4 in Chapter 4.5.4. As shown in Table 4.4, the severity values of the four types of inclusions (i.e. sulfide, alumina, silicate, oxide) obtained from both methods showed a good consistency for Seamless L80-Mo and ERW L80-0.5Mo steels. The only difference is the severity value of silicate in ERW L80-0.5Mo. SEM method measured a higher severity value of silicate compared with Clemex. This difference could be due to the different sampling volume of SEM method and Clemex method. The sampling volume of SEM method is relatively small compared to Clemex method, so the content of silicate may be measured to be higher in the sampling fields by SEM method. The fraction% of inclusion shape obtained from both examination methods also showed a difference in values for both steels. But this difference is mainly due to the different definitions of fraction % used in SEM and Clemex methods. In addition, the sampling volume of SEM is small compared to Clemex method. These may result in differences in the fraction% of inclusion shape.

Different shapes of carbides were characterized by performing image analysis (ImageJ 1.46 software) on SEM images. There are several limitations associated with image analysis techniques. Before taking SEM images, the specimens have to be well polished and etched to reveal only the

microstructural features rather than the scratches or pits from polishing. This limitation can be minimized by repeating the procedure outlined in Chapter 3.2. Measurements were performed on eight SEM images (at 5000X magnification) per specimen to obtain reliable data. For measurements of different shapes of carbides, the size and shape of the carbides were defined in ImageJ to ensure the results are independent of users. The size of a specific shape of carbides was defined in a range of value in the software and it was based on the measurements of 30 randomly selected carbides with the same shape. The shape of carbides was defined in a range from 0 to1 in the software, with 1 being perfectly globular. With the same input settings of size and shape of carbides, the data is repeated by the software for consistency regardless of who is operating the software.

5.2 SSC cracking behaviours

SSC is a cracking failure of steel under the combined action of tensile stress and corrosion in aqueous environments containing H_2S. The steels tested in this study include six quench-and temper L80 casing grade steels and one microalloyed steel (i.e. HSLA 80-2). As reviewed in Chapter 2, the L80 casing grade is required by API-5CT [12] specification to have controlled hardness and yield strength. For L80, it must not be harder than 23 Rockwell C and yield strength is controlled to within a variation of 15 ksi (i.e. in the range of 80-95ksi or 552-655MPa) [11, 12]. These limitations are usually used as a criterion for SSC prevention because strength is one of the factors affecting SSC resistance. It should be noted that among all tested steels, the yield strength of ERW L80-MnCr (682MPa) exceeded the upper limit for L80 casing product in API 5CT specification. However, although the other steels met the yield strength and hardness requirements of the API specification, SSC failure was still observed except for ERW L80-0.5Mo steel. The higher yield strength of ERW L80-MnCr may have some effect on its lower cracking resistance, but more importantly, it is believed that the lower cracking

resistance of ERW L80-MnCr is due to the presence of segregation banding in the microstructure. UTS is more sensitive to the hardest component in the microstructure. The relationship between UTS and RAR or time to failure in Figure 4.10 and 4.13 has shown that higher UTS lead to lower cracking resistance. ERW L80-MnCr has the highest UTS among the steels, followed by Seamless L80-Mo and Seamless L80-B that both have pearlite present in their microstructure. The presence of hard components in the microstructures of these three steels are most susceptible to cracking and results in higher SSC susceptibility.

SSC is generally accepted as a form of hydrogen embrittlement. When hydrogen is cathodically evolved on the steel surface (by H_2S corrosion reaction or cathodic charging), the presence of H_2S poisons the recombination reaction of hydrogen atoms to form hydrogen molecules on the surface and promotes the hydrogen atoms to enter the steel. In the steel, the hydrogen atoms diffuse to regions of high tri-axial stress or to some microstructural sites (e.g. inclusions, grain boundaries, vacancies etc) where they are trapped and reduce the ductility of the steel [18]. Corrosion pittings resulting from H_2S corrosion were observed in Figure 4.15 and 4.16. These pittings were found to be associated with inclusions which are discussed in next chapter. Brittle flat regions and HIC cracks observed from the fracture surface in Figures 4.15-4.20 are believed to be caused by the embrittling effect of trapped hydrogen. More HIC cracks are observed on ERW L80-MnCr and Seamless L80-Mo steels in Figures 4.17 and 4.18. These two steels have been shown to have higher SSC susceptibility (i.e. lower time-to-failure and RAR) among all the tested steels. This may be due to the higher hydrogen absorption in the susceptible microstructures. When the hydrogen accumulates to a critical value (i.e. saturation), cracking may result. Other steels were also observed to have HIC cracks either on the fracture surface (in the neutral axis) or along the gauge section of the specimen in a direction parallel to applied stress. Unlike SSC, HIC can occur in the absence of external stress in a susceptible

microstructure. Initiation of HIC is strongly dependent on the distribution and morphology of inclusions [64, 65]. Characterization of inclusions in Chapter 4.5 has shown a relationship between inclusion and SSC resistance that is further discussed in the next chapter. It is conceivable that the HIC cracks may facilitate the propagation of the SSC cracks to result in a faster time-to-failure. Figure 5.1 shows a SEM image of HIC connecting two adjacent SSC cracks in the gauge section of Seamless L80-B specimen. The HIC crack facilitated the SSC propagation in a direction perpendicular to applied stress.

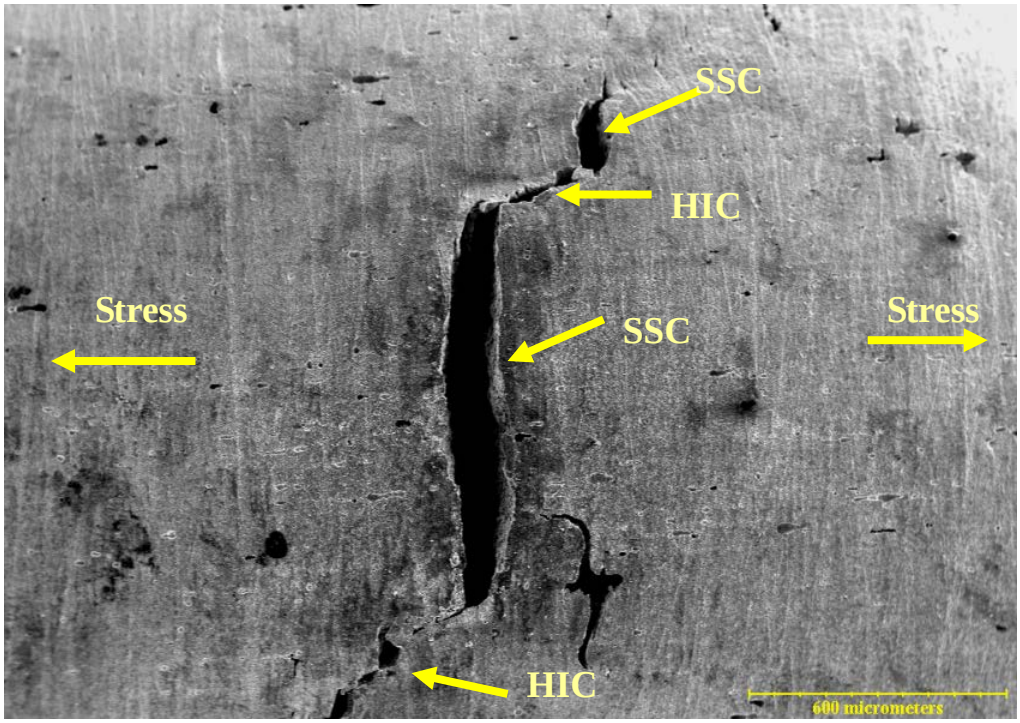

Figure 5.1: SEM image of HIC connecting two SSC propagating in a direction perpendicular to stress direction.

Examination of SSC fracture mode indicated that a mixed mode of intergranular and transgranular fracture was observed for more susceptible steels. For less susceptible steels, intergranular fracture was less prevalent. This is consistent with other researchers' findings. Asahi et al. [22] studied the SSC resistance of low alloy steels with tempered martensite structure and yield strength of 690-820MPa. They have shown that a sharp decrease in SSC resistance is associated with the onset of intergranular crack propagation that

occurs at lower SSC threshold stress, and the portion of intergranular cracking increases.

SSRT tests have shown some interesting results on stress-strain behaviours of steels (Figure 4.30). Three steels (i.e. ERW L80-MnCr, Seamless L80-B, and ERW L80-0.5Mo) with different alloying strategies (i.e. Mn-Cr, Ti-B, and Cr-Mo alloying) were tested by SSRT in NACE environment containing H_2S. All three steels exhibit the same yield character with a defined Luders band plateau in H_2S environment. All specimens got out of the Luders band before failing in the solution. ERW L80-0.5Mo (RAR=0.30) steel exhibits a larger Luders band plateau than Seamless L80-B (RAR=0.24) and ERW L80-MnCr (RAR=0.13). It is conceivable that the presence of hydrogen may somehow promote the influence of Cottrell atmospheres and hence promoting Luders band development. There may be a connection between SSC resistance and the straining behaviour of steels.

Similar findings were found in Kaneko's research. Kaneko[66] and coworkers evaluated the SSC performance of three API-C90 (yield strength: 90 ksi) tubular steels by SSRT in the same NACE environment at a strain rate of $1x10^{-6}$ s^{-1}. Similar to our study, the tensile specimens were pre-immersed in NACE environment for 24 hour before straining to achieve a steady state hydrogen distribution. The three steels had different microstructures. The first is a conventional tempered martensite structure. The second one is tempered martensite structure with finer prior austenite grains compared to the first one. The third one is ultra-fine ferrite with well-distributed fine carbides. They also observed the Luders band plateau for these three steels and they found that the elongation of the Luders band was related to grain size (Figure 5.2). The three microstructures are indicated as I through III in the figure. A significant influence of grain refining on Luders elongation can be observed in this figure. SSC failure in SSRT tests usually occur during plastic deformation, i.e. between yield strength and ultimate tensile strength[66]. Kaneko concluded that a refined microstructure with larger Luders elongation resulted in stress

relaxation at the stress concentrated site and allowed larger total strain up to failure in the SSRT test[66]. This behaviour results in an improvement of SSC resistance.

In this study, ERW L80-0.5 Mo which showed a larger Luders elongation in SSRT test has a microstructure of tempered martensite with uniformly distributed fine carbides. The other two steels, namely Seamless L80-B and ERW L80-MnCr, had banded microstructure. The more uniform microstructure of ERW L80-0.5Mo may be one of the reasons for its higher SSC resistance. The effect of microstructure refining on improvement of SSC resistance could be an interesting study for the future.

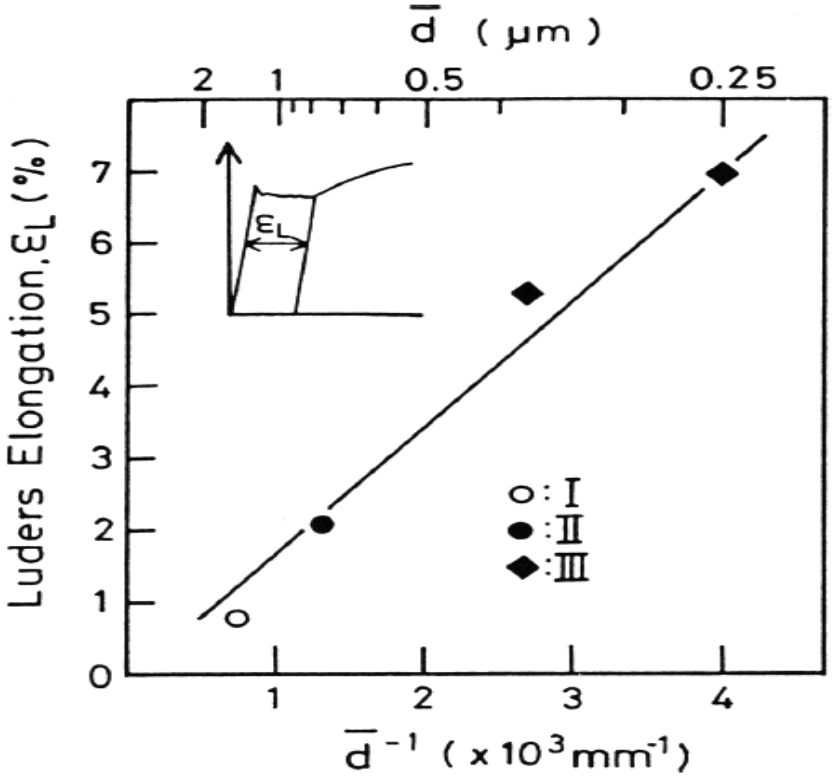

Figure 5.2: Relation between Luders elongation and mean recrystallized grain size for microstructure I through III [66].

5.3 The effect of alloying element

Addition of alloying elements can have several effects on the properties of steels such as improving hardenability, corrosion resistance, deformability, and machinability. The relationship between alloying elements, heat treat condition

and hydrogen diffusion is very complex. The resulting microstructure of a quench and temper steel can be very different depending on the alloying composition and heat treat conditions.

The steels tested in this study consisted of three main alloying strategies, namely Mn-Cr, Cr-Mo, and Ti-B alloying. Addition of these alloying elements has an influence on the mechanical properties and resulting microstructure. From literature review, it has been reported that a fully martensitic structure followed by heavily tempering treatment can offer the best SSC performance [49, 50]. To achieve a fully martensitic microstructure, good hardenability is required. Mn and Cr are used conventionally to improve hardenability. But Mn tends to segregate during continuous casting and can lead to formation of elongated MnS inclusions which can result in crack initiation. In addition Cr can improve hardenability and corrosion resistance, but high levels of Cr (>0.5 wt%) result in formation of M_7C_3 and $M_{23}C_6$ carbides which are incoherent with the matrix and can lead to crack initiation from hydrogen accumulation [10, 47, 48]. Mo is an important solid solution strengthener and also plays a role in precipitation strengthening. It can significantly improve hardenability, promote development of a hard martensitic structure, and as well as maintain sufficient impact toughness. The literature review showed that less than 1wt% Mo can provide good SSC resistance. Above 1wt%, acicular Mo_2C precipitates can form and act as crack initiator [49]. Boron has also been reported to improve hardenability and is usually alloyed with Ti to scavenge the residual nitrogen before boron can be effective.

Solid solutions effects of these alloying elements play a role in improving the mechanical properties and SSC performance of the steels. But their effect can only be explained with respect to the resulting microstructure, inclusion and carbide characteristics. Taking Cr-Mo steels for instance, both Seamless L80-Mo and ERW L80-0.5Mo have the same alloying strategies. Their yield strength showed some difference (642MPa for Seamless L80-Mo and 610MPa for ERW L80-0.5Mo) which could be due to the differences in

alloy additions, heat treat condition and the resulting microstructure. ERW L80-0.5Mo has a higher addition of Mo (0.5wt % Mo) compared to Seamless L80-Mo (0.06wt% Mo). Their microstructure and SSC susceptibility are very different. Seamless L80-Mo has a microstructure consisting of ferrite and lamellar structure of pearlite, and it exhibits high SSC susceptibility (RAR=0.15, time to failure=36 hours). ERW L80-0.5Mo has a homogeneous tempered martensitic structure with well-distributed, fine globular carbides, and it exhibits lower SSC susceptibility (RAR=0.30, time to failure >720hours). In addition, characterization of carbides in Chapter 4.6.1 has shown that globular molybdenum carbides were found in ERW L80-0.5Mo but not in Seamless L80-Mo. Inclusion characterization (as will be discussed in next chapter) also showed that ERW L80-0.5Mo has less elongated inclusions and no inclusion clustering compared with Seamless L80-Mo. So, addition of higher Mo amount in ERW L80-0.5Mo plays a role in improving the strength, refining the microstructure, formation of molybdenum carbide which may have an effect on strength as well, and improving SSC resistance.

5.4. The effect of cleanliness on SSC crack initiation

Hydrogen trapping at inclusions is an important concern. The critical hydrogen concentration required for crack formation equals the combination of diffusible hydrogen in reversible traps and lattice and the immobile hydrogen in irreversible traps [67]:

$$C_{critical}=C_{reversible}+C_{irreversible} \quad 5\text{-}1$$

Inclusions are generally considered as having irreversible trapping behaviour[67]. Inclusions are strong trapping sites for hydrogen because of the interface between inclusion and steel matrix and the local stresses around the inclusion arising from the different thermal expansion coefficients of inclusion and matrix during steel processing [67]. These local stresses promote the accumulation of hydrogen gas at the inclusion/matrix interface. This in turn

could lead to very high internal gas pressure and exceed $C_{ctitical}$ to nucleate cracking at inclusions. As a result, cleanliness of the steel, especially the presence of oversize oxide inclusions and the inclusions that have a sharp interface with the matrix, could act as stress raisers and provide easier crack path for brittle crack propagation, and is found to be an important factor governing the crack initiation stage.

5.4.1. Inclusion type

Results from previous chapters have shown that higher inclusion density, higher fraction of sulfide, alumina, silicate and globular oxides increase SSC susceptibility. The steels were separated into different alloying groups for comparison. Mn-Cr-Mo steels include ERW L80-0.5Mo, ERW L80-CrMo, ERW L80-MnCr, Seamless L80-Mo. Ti-B steels include ERW L80-B and Seamless L80-B. The sensitivities of different types of inclusions on SSC susceptibility can be calculated from the slope of the linear relationship between RAR and inclusion fraction% in Figures 4.41-4.44 for Mn-Cr-Mo steels and Figures 4.45-4.48 for Ti-B steels. The sensitivities of different types of inclusion on SSC susceptibility are summarized in Table 5.1.

Table 5.1: Sensitivity of different types of inclusion to SSC susceptibility.

Steels	Sulfide	Alumina	Silicate	Oxide
Mn-Cr-Mo	-8.7	-7.4	-16.6	-2.4
Ti-B	-6.9	-3.5	-4.3	-0.64

For Mn-Cr-Mo steels, SSC susceptibility was most susceptible to elongated silicate. However, for Ti-B steels, elongated sulfide had the greatest effect on SSC behaviours. Elongated sulfide inclusion (e.g. MnS stringer) has been well documented in literature [68] to be one of the most detrimental sites for cracking. Unfortunately both ASTM E45-2005 and JIS G055 do not take

into account the Titanium nitride (TiN) particles for characterization. TiN should be more prominent in the Ti-B treated steels and has reported in literature [69] to be one of the major nucleation sites for HIC in addition to MnS. The following chapter will further address the effect of inclusion shape on SSC resistance.

5.4.2. Inclusion shape

Inclusion shape is an important concern for SSC resistance. Both elongated and globular inclusions had an adverse effect on SSC resistance in Chapter 4.5.2.3. Table 5.2 compares the sensitivities of inclusion shape to SSC. The sensitivities were determined by calculating the slope of the linear relationship between RAR and inclusion shape % in Figures 4.52-4.55. It can be seen that SSC susceptibility is still more sensitive to elongated inclusions than to globular inclusions, for both Mn-Cr-Mo and Ti-B steels. The adverse effect of globular inclusion could be due to the presence of oversize oxide (>10μm) inclusions in the steels.

Table 5.2: Sensitivity of inclusion shapes to SSC susceptibility.

Steels	Elongated inclusions	Globular inclusions
Mn-Cr-Mo	-3.8	-2.4
Ti-B	-1.5	-0.8

Fracture surface examination by SEM and EDX demonstrated that cracking was initiated from elongated and oversize globular inclusions. Figures 5.3 and 5.5 show that cracking initiation at stringer inclusions. EDX spectra in Figure 5.4 show that the stringer inclusion in Figure 5.3 is consisted of Mn and S. In Figure 5.6, EDX spectra show that the stringer inclusion (in Figure 5.5) is consisted of Al, Si, and O.

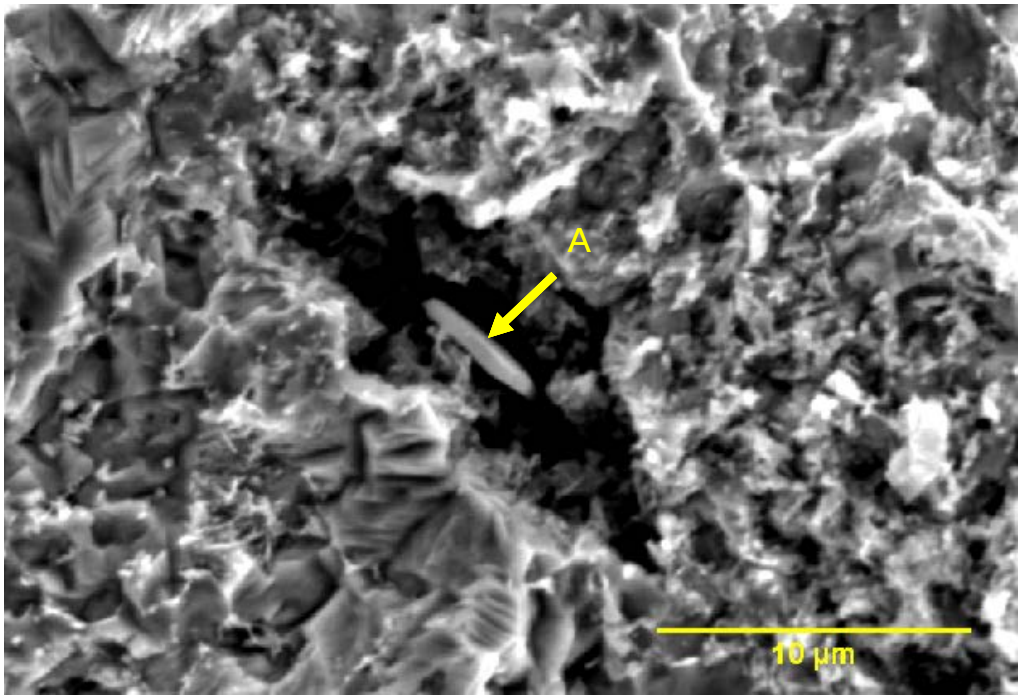

Figure 5.3: Crack initiation at elongated inclusion A in Seamless L80-Mo steel.

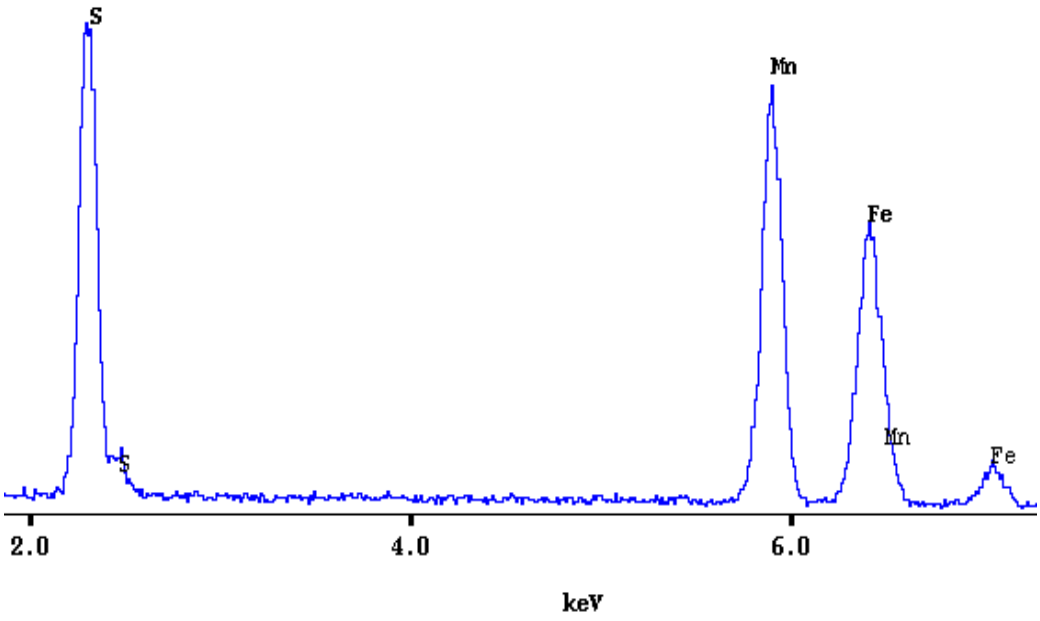

Figure 5.4: EDX spectra for particle A in Figure 5.3.

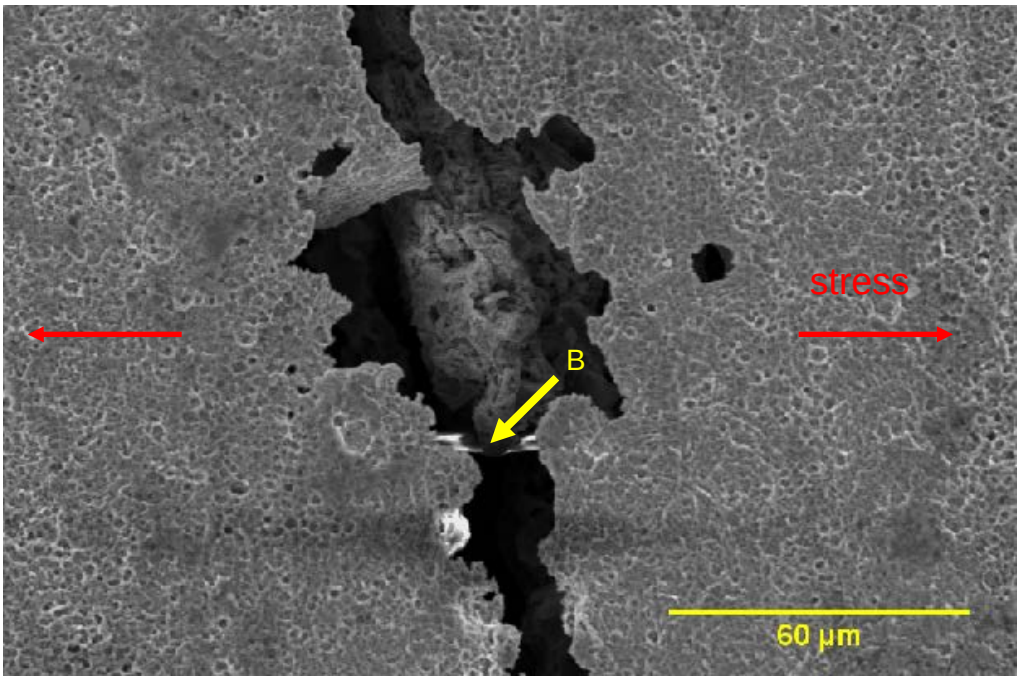

Figure 5.5: SSC crack perpendicular to applied stress initiated at stringer inclusion B in Seamless L80-B steel.

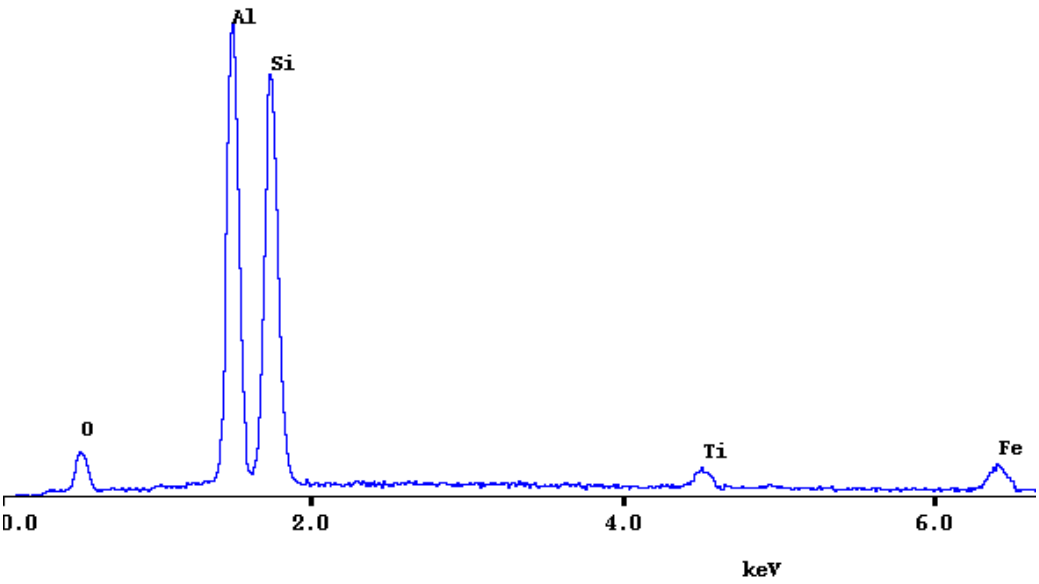

Figure 5.6: EDX spectra for particle B in Figure 5.5.

Figure 5.7 shows cracking initiation at large globular oxide inclusions. The inclusion has a size of about 10μm. EDX spectra in Figure 5.8 show that the particle was consisted of Ca, O and little amount of S.

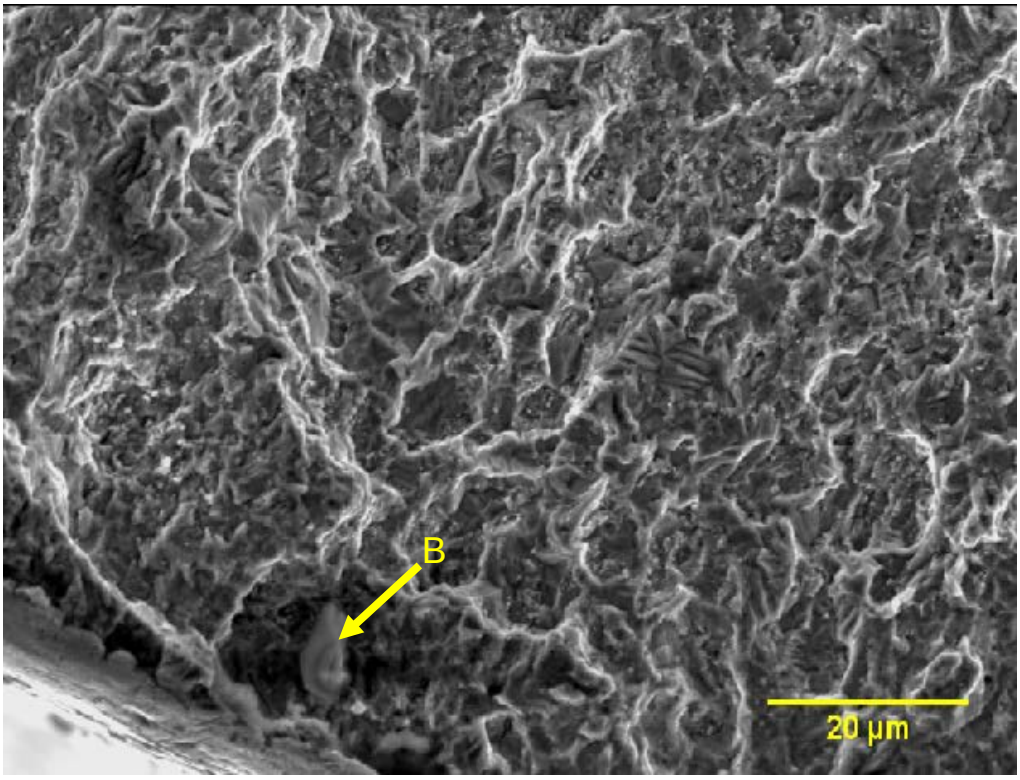

Figure 5.7: Crack initiation at globular inclusion B in Seamless L80-Mo steel.

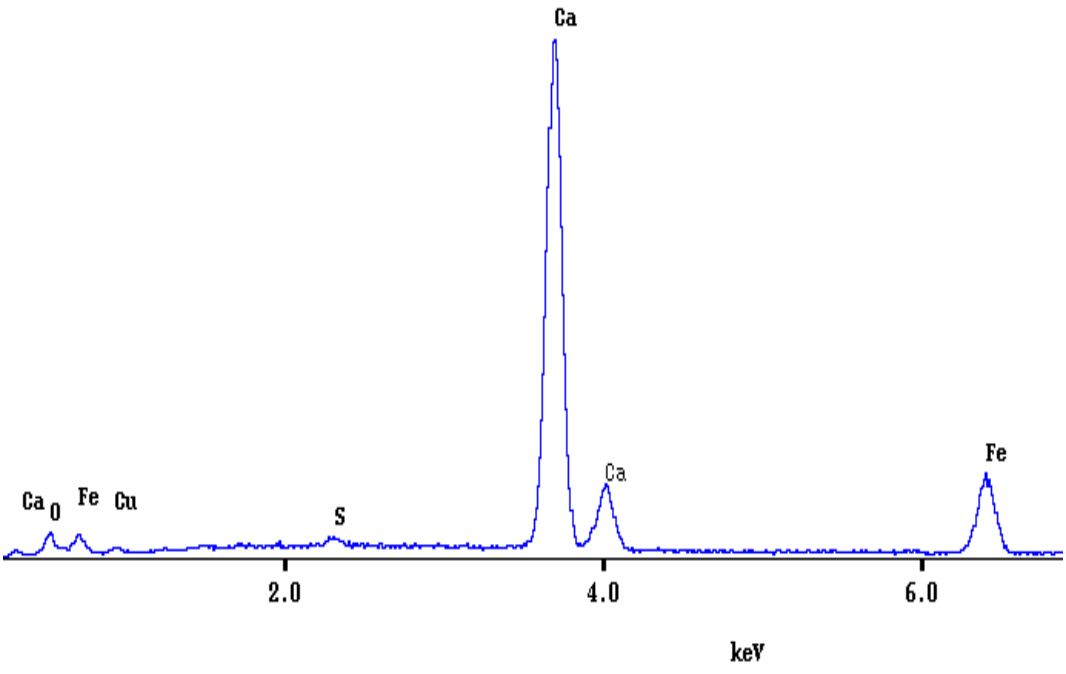

Figure 5.8: EDX spectra of particle B in Figure 5.7.

5.4.3. Inclusion clustering

Inclusion clustering was examined qualitatively by SEM equipped with EDX. Table 5.3 summaries the relationship between inclusion clustering and SSC resistance in terms of RAR and time-to-failure. The steels with inclusion clustering (i.e. Seamless L80-Mo, Seamless L80-B, ERW L80-MnCr, and HSLA 80-2 steels) all have shown a lower RAR and time-to-failure in SSC test, compared to the steels with no clustering (i.e. ERW L80-B and ERW L80-0.5Mo).

Table 5.3: Relationship between inclusion clustering and SSC resistance

	Presence of clustering?	RAR	Time to failure (hours)
ERW L80-B	No	0.28	624
Seamless L80-B	Yes	0.24	52
ERW L80-MnCr	Yes	0.13	20
Seamless L80-Mo	Yes	0.15	36
ERW L80-CrMo	Yes	0.25	60
ERW L80-0.5Mo	No	0.30	>720
HSLA 80-2	Yes	0.26	60

Examination of the fracture surface of Seamless L80-B found the crack was initiated from the corrosion pits as indicated by the circle in Figure 5.9. Higher magnification within the circle region (in Figure 5.10 and 5.13) found the pittings were associated with a cluster of particles. EDX spectra in Figures 5.11, 5.12, 5.14, 5.15 show that the particles in Figure 5.10 were enriched in Ti, and in Figure 5.13 were enriched in Ca, Al and O. The Ti-enriched particle has a size about 7 μm. The cluster of Ca and Al-enriched particles is a complex oxide inclusion which has size about 20 μm. Stress concentrations at these

large and hard inclusions are typical crack nucleation site and increase SSC susceptibility.

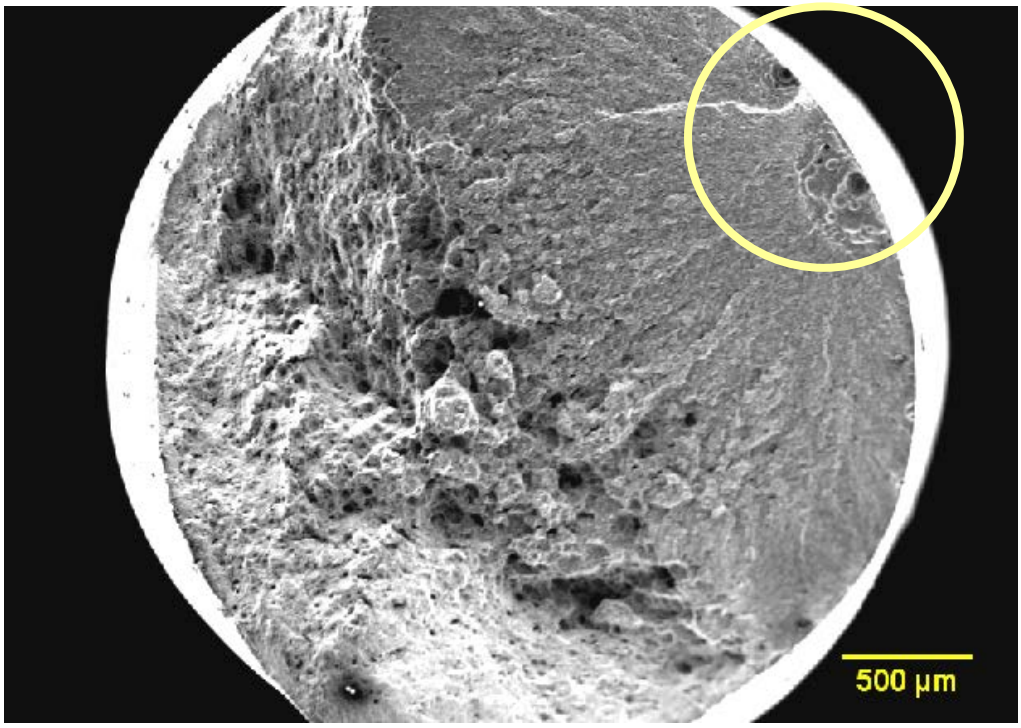

Figure 5.9: Crack initiation from the pitting sites (indicated by the circle) near the surface of Seamless L80-B steel.

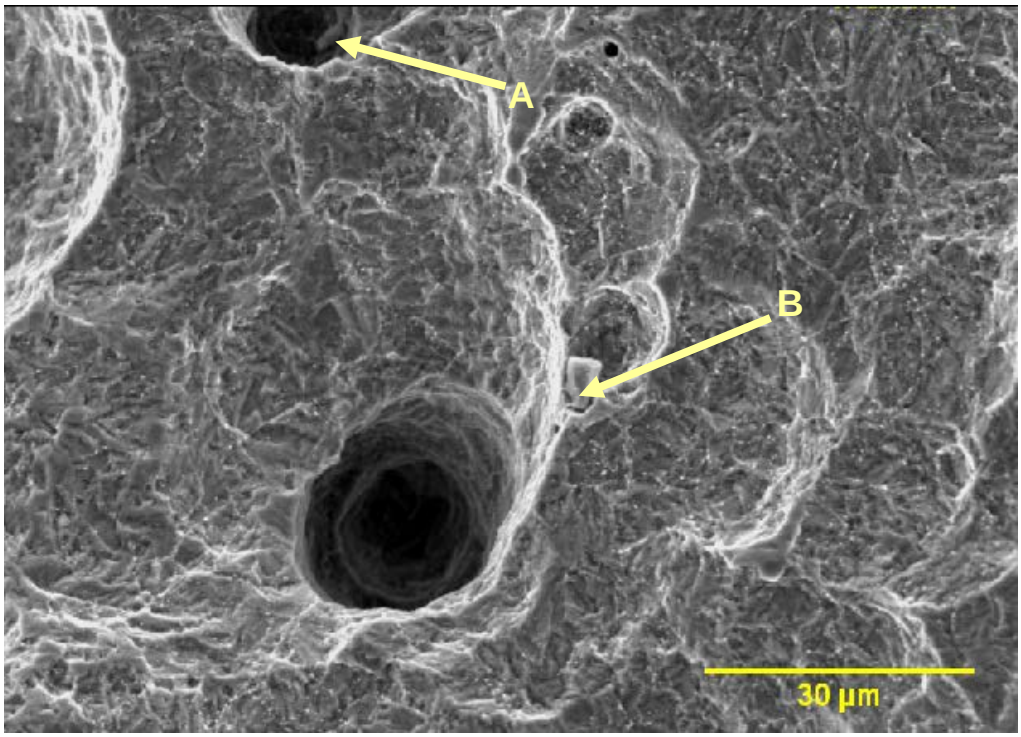

Figure 5.10: Crack initiation from corrosion pits associated with particles A and B in Seamless L80-B steel.

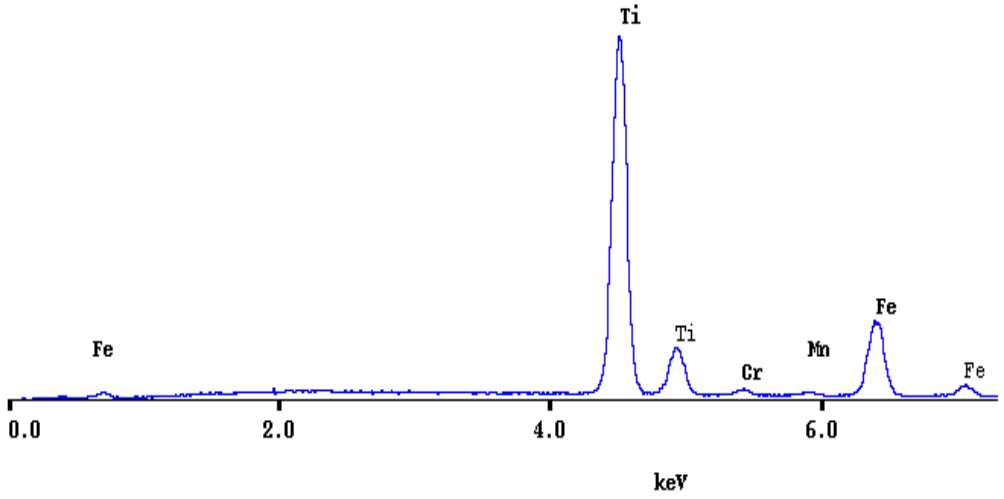

Figure 5.11: EDX spectra for particle A in Figure 5.10.

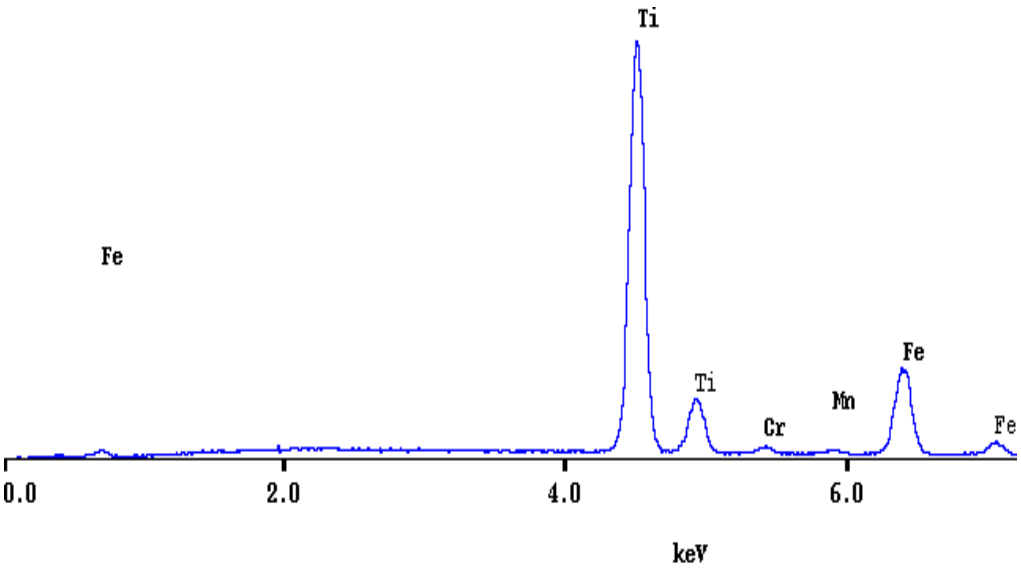

Figure 5.12: EDX spectra for particle B in Figure 5.10.

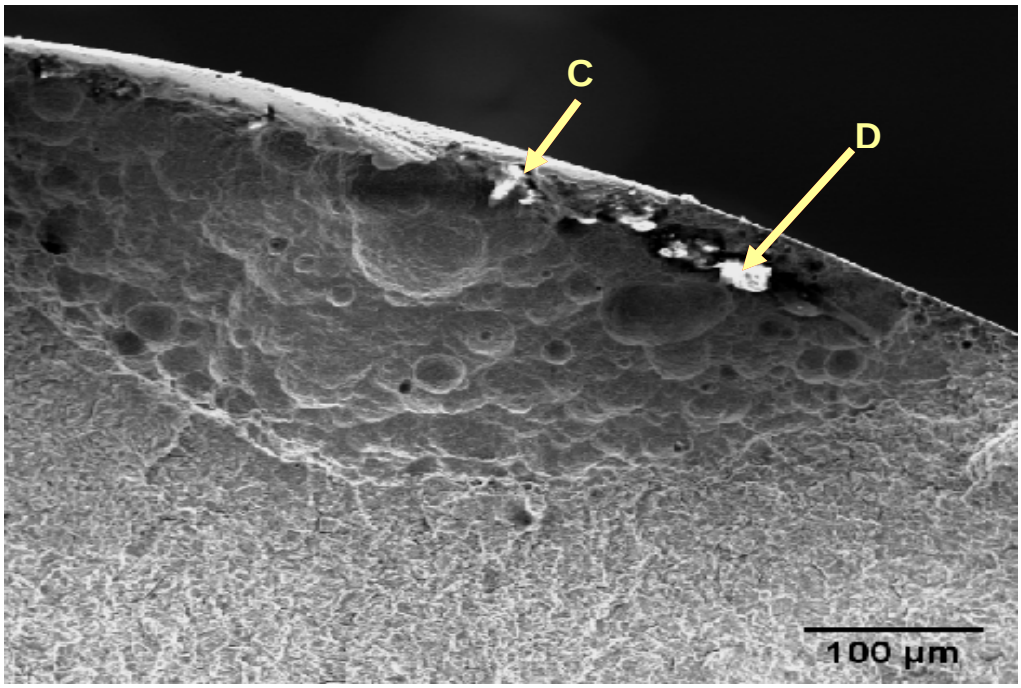

Figure 5.13: Crack initiation from inclusion clusters in Seamless L80-B steel.

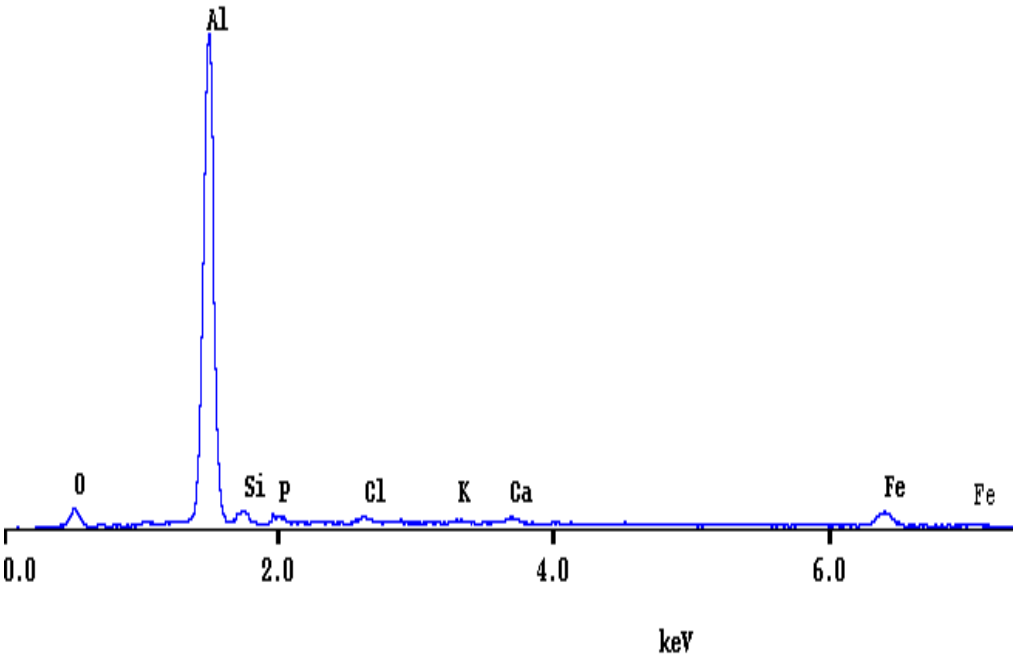

Figure 5.14: EDX spectra for particle C in Figure 5.13.

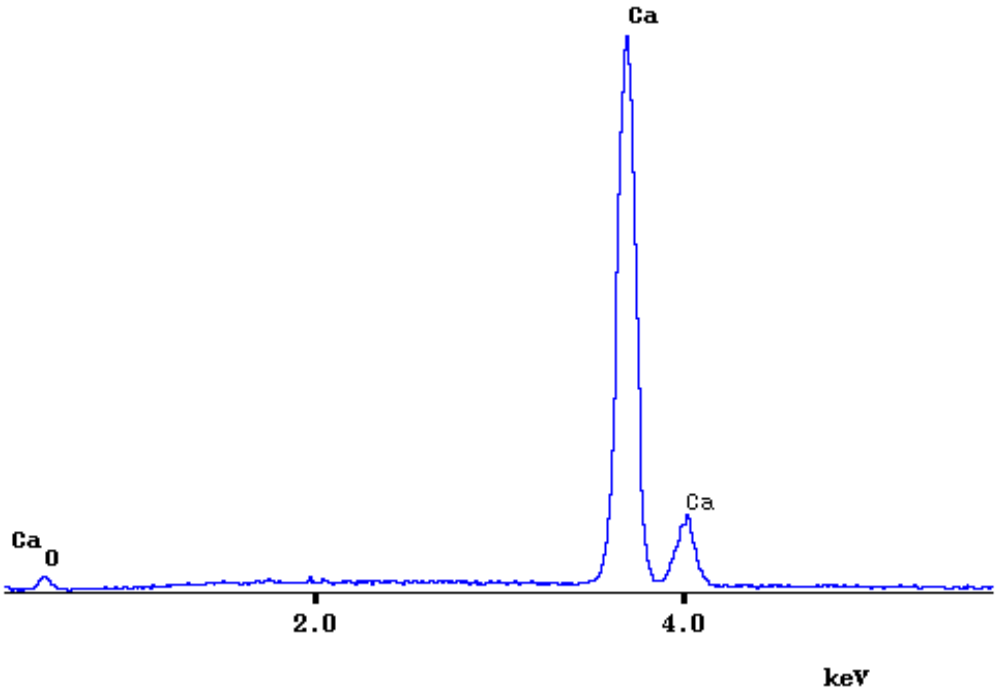

Figure 5.15: EDX spectra for particle D in Figure 5.13.

Similar results were observed by Kim et al.[53] who studied the effect of metallurgical factors on SSC of low alloy steel. They found cracking were primarily nucleated at inclusion clusters enriched in Al-Ca-O.

5.5. The effect of carbide shape on SSC resistance

Similar to the effect of inclusions, the carbide precipitates could also act as strong trapping sites for hydrogen [67]. Whether they are acting as irreversible or reversible trapping sites depend on their binding energy with hydrogen. Kang et al. [70] have defined the different trapping sites by calculating activation energies for hydrogen desorption using thermal desorption spectrometry (TDS) for 0.2C–Cr and 0.2C–Cr–Mo steels. Their study found that reversible trapping sites for hydrogen are grain boundaries and lath boundaries of martensite, while carbide/matrix interfaces act as irreversible trapping sites for hydrogen. Earlier literature from Pressouyre [71] and Lee [72] also documented about the irreversible hydrogen trapping behavior at TiC interface. Therefore it is reasonable to assume that carbides

are irreversible trapping sites in present study. If these irreversible traps with high hydrogen binding energy and low hydrogen saturability are finely and uniformly dispersed in the matrix, it minimizes the diffusion of mobile hydrogen to susceptible regions to cause embrittlement.

Characterizations of carbides were performed on four steels, namely ERW L80-0.5Mo, ERW L80-B, Seamless L80-B, and Seamless L80-Mo. These four steels were chosen because they represent different alloying strategies. ERW L80-0.5Mo and Seamless L80-Mo are alloyed with Mn-Cr-Mo. ERW L80-B and Seamless L80-B are alloyed with Ti-B. Characterization results in Chapter 4.6 have shown that SSC resistance decrease as the elongated carbide % increases. Increase of globular carbides leads to an increase of SSC resistance. The sensitivity of carbide shape on SSC resistance can be calculated from the slope of the linear relationship between RAR and carbide shape % in Figures 4.59 and 4.61. For elongated carbides, the sensitivity was determined to be -0.0078. For globular carbides, the sensitivity was 0.036. In other words, SSC resistance is more sensitive to a change in globular carbide% than to elongated carbide, and it can be improved by increasing the content of globular carbides in the steels.

ERW L80-0.5Mo steel, which has a uniformly dispersed globular carbides microstructure, has shown a higher cracking resistance in sour environment from SSC test results compared to Seamless L80-Mo or Seamless L80-B steel that exhibit banded structure of elongated carbides colonies (pearlite) in the microstructure. One can easily imagine the adverse effect of elongated carbides. Not only they are hard particles and present as clusters/colonies in the steel microstructures which act as large hydrogen trapping sites, but they also provide a ready crack path for brittle crack initiation and propagation once the hydrogen accumulation reached a critical value. Figure 5.16 shows an SEM image of transgranular HIC crack which nucleated from the pearlite colonies (indicated by the circle in the figure) and propagated through the matrix in Seamless L80-Mo steel (2% Nital etched).

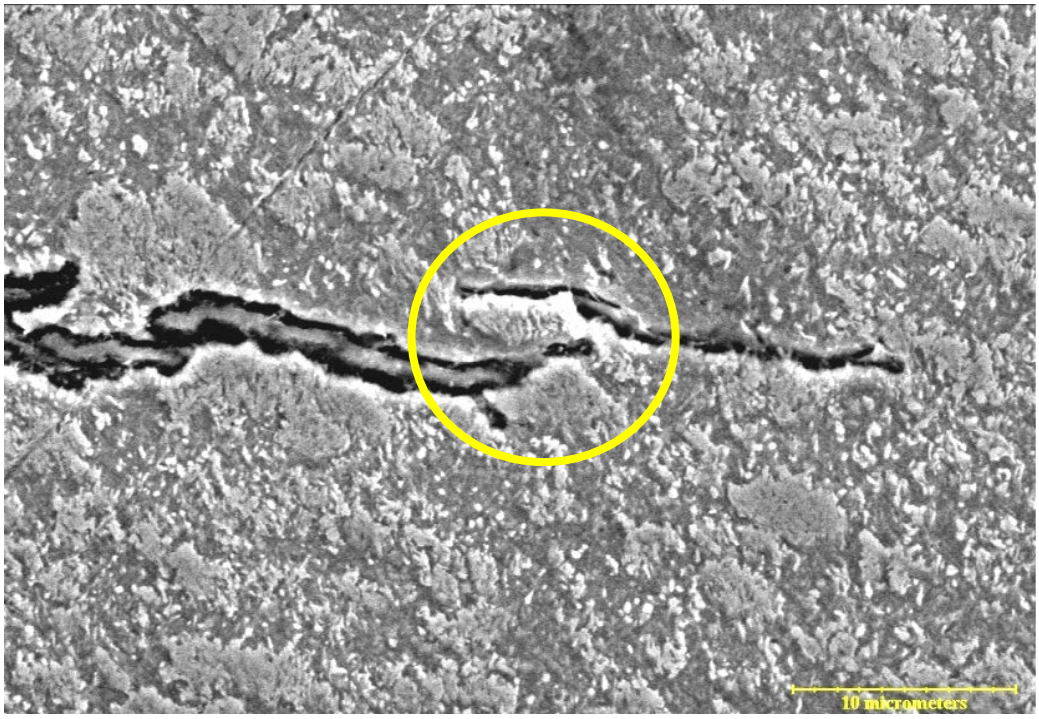

Figure 5.16: Transgranular HIC (propagating in the neutral axis) initiated from the pearlite colonies (indicated by the circle) and propagated through the matrix in Seamless L80-Mo steel (2% Nital etched).

Similar results have been reported in Kang et al.'s work [70] for the study of the effect of carbide formation on hydrogen delayed fracture of 1.2GPa quench and temper 0.2C–Cr–Mo steels, 0.2C–Cr steels, and 0.3C–Si steels. They found that chromium (Cr) and molybedum (Mo) additions can increase the spheroidization rate and decrease the carbide size. Also, the spherical carbides obstruct the initiation and propagation of microcracks where elongated shape carbides facilitate crack propagation[70].

5.6. The dominant factor for SSC performance

SSC is a hydrogen embrittlement phenomenon which results in a steel failing well below its yield strength. The metallurgical factors (i.e. alloying composition, cleanliness, microstructure etc) play an important role in the steel's performance in sour environment. Data from laboratory studies or field

experience have shown that even an extremely low H_2S concentration is enough to result in SSC failure of a susceptible material [18]. It is important to improve the SSC resistance of steel to withstand the increasingly harsh environment. However, the dominant factor for SSC behaviors is not yet understood in literature.

In this study, the effect of mechanical properties, inclusion, and carbide morphology on SSC resistance were investigated. SSC cracking behaviors can not be solely explained by mechanical properties (i.e. YS, UTS and hardness), because mechanical properties depend on the alloying composition, heat treat condition and the microstructure of materials. Inclusion and carbides were characterized and discussed in relation to SSC resistance in previous chapters. Table 5.4 compares the sensitivity values of inclusions and carbides on SSC resistance (in terms of RAR). It was found that inclusions had a greater effect on SSC resistance than carbides. Fracture surface examination shown in Chapter 5.4 also revealed that inclusions were the critical crack nucleation sites for SSC.

Table 5.4: Comparison of sensitivity of inclusion and carbides on SSC resistance.

Steels	Elongated inclusions (sulfide+alumina+silicate)	Globular inclusions (oxide)	Elongated carbides	Globular carbides
Mn-Cr-Mo	-3.8	-2.4	-0.0078	0.036
Ti-B	-1.5	-0.8		

However, this does not mean that carbides do not have an effect on SSC cracking behavior. A good microstructure should be able to stop the crack from propagation once a crack has initiated. The distribution and morphology of carbides in the microstructure were believed to play an important role in SSC

propagation. As discussed in previous chapter, SSC resistance is more sensitive to a change in globular carbide% and can be improved by increasing the content of globular carbides in the steels. Comparisons of the microstructure of ERW L80-0.5Mo to other steels have shown that a uniform microstructure with fine globular carbides can improve SSC resistance. This may be due to the high density and uniform distribution of carbide traps in the microstructure which minimizes the diffusion of mobile hydrogen to susceptible regions (e.g. inclusions or an existing crack initiated from an inclusion) to cause embrittlement. Inversely, clusters of elongated carbides in the microstructure (e.g. Seamless L80-B and Seamless L80-Mo) act as large hydrogen accumulation sites and provide a ready crack path for crack propagation. Furthermore, the ferrite grain size is much smaller in ERW L80-0.5Mo compared to other steels. A refined microstructure is known to improve the toughness of steels and thus preventing the crack from propagation.

6. CONCLUSIONS

In this study, the SSC susceptibility of casing steels with different alloying strategies (i.e.Ti-B, Mn-Cr, and Cr-Mo) was investigated. Characterization of inclusions and carbides were performed. The dominant factor contributing to SSC susceptibility was determined.

The microstructures of the steels examined were mostly tempered martensitic structures. The most important difference between the microstructures of the steels was the distribution and shape of carbides. The microstructures examined were summarized as follows:

- ERW L80-B steel: The microstructure is consisted of tempered martensite. The carbides are mostly globular in shape and distributed randomly in the matrix.
- Seamless L80-B steel: The microstructure is consisted of ferrite and carbides, and islands of lamellar pearlite. Most of the elongated carbides are clustered in the lamellar structure. Globular carbides are distributed inside the ferrite or along the grain boundaries.
- ERW L80-Mn-Cr steel: The microstructure is consisted of tempered martensite. The carbides appear to be globular in shape. Segregation banding is observed.
- Seamless L80-Mo steel: The microstructure is consisted of ferrite and carbides, and islands of lamellar pearlite. Most of the elongated carbides are clustered in the lamellar structure. Globular carbides are distributed inside the ferrite or along the grain boundaries.
- ERW L80-CrMo steel: The microstructure is consisted of tempered martensite. The carbides are distributed inside ferrite and along grain boundaries.
- ERW L80-0.5Mo steel: The microstructure is consisted of tempered martensite. However the carbides appeared to be smaller and more dispersed throughout structure.
- HSLA 80-2 steel: The microstructure consists of polygonal ferrite and

carbides. Most carbides are distributed along the grain boundaries, with some inside the ferrite.

The microstructures of the seamless materials indicate that Seamless L80-B and Seamless L80-Mo may not have been properly quenched during processing visible by the presence of lamellar cementite.

SSC susceptibility assessments

- Constant load SSC test (proof ring) and SSRT test were used to evaluate the SSC susceptibility of steels. Comparisons of results from both tests showed a good consistency in tendency of SSC resistance. SSRT tests can be used to replace SSC tests for evaluation of cracking susceptibility of steels as it showed the same trend in crack susceptibility under much lower testing duration.
- SSC resistance generally decreases with increase of material strength.
- A linear relationship could be used to predict RAR from yield strength:

  $$RAR=-0.0017\ (Y.S.)+1.31,\ 580\ MPa \leq YS \leq 682MPa$$

- The following SSC resistance ranking could be proposed in terms of RAR:

ERW L80-0.5Mo > HSLA 80-2 > ERW L80-B > ERW L80-CrMo > Seamless L80-B > ERW L80-MnCr > Seamless L80-Mo.

- For steels with lower SSC resistance, a mixed mode of transgranular and intergranular fracture was observed, for higher resistance steels, intergranualr fracture is less prevalent.

Effect of inclusions

- The inclusion shape, type, and severity levels were characterized using both SEM-EDX and OM-Clemex techniques. Comparison of results from both examination methods showed small differences in severity levels and shape fraction due to different sampling volume and definition of parameters.

- Lower inclusion density, lower fractions of sulfide, alumina, silicate and globular oxides have shown to lead to higher SSC resistance.
- The effect of inclusion fraction on SSC resistance is related to alloying composition. Mn-Cr-Mo steels were more susceptible to the presence of inclusions than Ti-B steels.
- Both elongated and globular inclusions had an adverse effect on SSC resistance, but SSC susceptibility was found to be more sensitive to elongated inclusions than to globular inclusions. The adverse effect of globular inclusions was attributed to the presence of large oxide inclusion (with size >10μm).
- Fracture surface study found that cracking were initiated mainly from elongated inclusions enriched in Mn-S, Al-Si-O, or large globular oxide inclusions (with size >10μm) enriched in Ca-O-S.
- Clusters of inclusions were important crack initiation sites for SSC.

Effect of carbides and microstructure

- Carbides of different shapes were characterized by image analysis. AES was used to determine the composition of carbides.
- Higher fraction of elongated carbides led to lower cracking resistance.
- SSC resistance is more sensitive to a change in globular carbide% than to elongated carbide%, and it can be improved by increasing the content of globular carbides in the steels.
- The carbides (elongated and globular) in all steels were characterized as cementite. Globular molybdenum-carbides were observed only in ERW L80-0.5Mo steel.

Comparisons between effect of inclusions and carbides

- SSC susceptibility was found to be more sensitive to inclusions than to carbides. Inclusions were the critical nucleation sites for SSC.
- The distribution and morphology of carbides in the microstructure

were believed to play an important role in SSC propagation. ERW L80-0.5Mo which has a uniform microstructure with fine globular carbides was found to improve SSC resistance. This may be due to the high density and uniform distribution of carbide traps in the microstructure which minimizes the diffusion of mobile hydrogen to susceptible regions (e.g. inclusions or an existing crack initiated from an inclusion) to cause embrittlement. Inversely, clusters of elongated carbides in the microstructure (e.g. Seamless L80-B and Seamless L80-Mo) act as large hydrogen accumulation sites and provide a ready crack path for crack propagation.

7. FUTURE WORK

The following future work is recommended.

7.1 Spheroidization of carbides

In this study, carbide morphology was characterized by image analysis technique. Other characterization methods may be conducted to compare the results from image analysis. Increase of globular carbides in the microstructure was found to improve SSC resistance. Further study can be conducted to evaluate the effect of globular carbides in microstructure and determine the optimum processing conditions for spheroidization.

7.2 Effect of Luders band on SSC resistance

From SSRT test, the stress-strain curves of the specimens showed Luders band plateau when testing in NACE-H_2S environment. Kaneko's paper [65] reported that this Luders elongation was related to grain size of the microstructure. The effect of Luders bands on SSC resistance and the effect of grain size on Luders bands can be further studied using SSRT. In addition, prior to straining in SSRT, the specimen was pre-immersed in NACE-H_2S environment for 24 hours to achieve a steady state hydrogen distribution. It is conceivable that hydrogen may play a role in the development of Luders bands. The relationship between hydrogen concentration and Luders elongation can be explored as well.

7.3 Hydrogen trapping behaviors of inclusions and carbides

The hydrogen trapping behaviors in the steel matrix is very complex and not yet clearly understood. The relationship between hydrogen concentration, hydrogen diffusion, and contents of inclusions and carbides can be explored. The distribution of hydrogen around inclusions or carbide/matrix interface was studied by some researchers using tritium autoradiography [73, 74]. If equipment is available, tritium autoradiography can be used to identify the hydrogen trapping sites.

REFERENCES

1. Pouliquen, F., C.Blanc, E.Arretz, I.Labat, J.Tournier-Lasserve, A.Ladousse, J.Nougayrede, G.Savin, R.Ivaldi, M.Nicolas, J.Fialaire, R.Millischer, C.Azema, L.Espagno, H. Hemmer and J.Perrot, *Hydrogen Sulfide*, in *Ullmann's Encyclopedia of Industrial Chemistry*. 2000, Wiley-VCH Verlag GmbH & Co.
2. Zhao, M.-C., Tang, Bei., Shan, Yi-Yin., Yang, Ke., *Role of microstructure on sulfide stress cracking of oil and gas pipeline steels.* Metallurgical and Materials Transactions A, 2003. **34**(5): p. 1089-1096.
3. Elboujdaini, M., *Hydrogen induced cracking and Sulfide Stress cracking*, Uhlig's Corrosion Handbook, R.W. Revie, John Wiley & Sons, Inc. 2011, p. 183-193.
4. Venegas, V., F.Caleyo, J. L.González, T.Baudin, J. M. Hallen, and R.Penelle, , *EBSD study of hydrogen-induced cracking in API-5L-X46 pipeline steel.* Scripta Materialia, 2005. **52**(2): p. 147-152.
5. Sponseller, D.L., R.Garber and J.A.Straatman, *Effect of Microstructure on Sulfide-Stress-Cracking Resistance of High Strength Casing Steels*, MiCon 82:Optimization of Processing, Properties, and Service Performance Through Microstructure Control, ASTM STP 792, Halle Abrams, American Society for Testing and Materials, 1983, p.172-204.
6. *Directive 010-Minimum Casing Design Requirements*, Energy Resource Conservation Board, Calgary, AB, 2009.
7. *NACE MR0175/ISO 15156-Petroleum And Natural Gas Industries—Materials For Use In H_2S-Containing Environments In Oil And Gas Production*, NACE. International, Houston, Tx., 2003.
8. *IRP Volume 1-Critical Sour Drilling, An Industry Recommended Practice for the Canadian Oil and Gas Industry.*, Drilling and Completion Committee, Calgary, AB, 2008.

9. Jordan, J. and L. Collins, *Development of Electric-Resistance Welded, High Strength Steel Casing for Critical Sour Service*, Northern Area Western Conference proceeding, NACE International, February 6-8, Regina,Saskatchewan,Canada, 2011, Paper No. 013.
10. Marsh, P.G. and W.W. Gerberich, *Stress-Corrosion Cracking of High-Strength Steels (Yield Strengths Greater Than 1240 MPa)*, Stress-Corrosion Cracking Materials Performance and Evaluation, R. H.Jones, ASM International, Materials Park, Ohio, 1992, p. 63-89.
11. Urband, B.E. and S. Morey, *High Strength Sour Service C110 Casing*, SPE/IADC Drilling Conference proceeding, Society of Petroleum Engineers, Amsterdam, Netherlands, March 9-11, 1999, Paper No.52843-MS.
12. *API 5CT- Specification for Casing and Tubing*, American Petroluem Institure, Washington, D.C., 2005.
13. Rogers, W.F. and J.A. Rowe. Jr, *Corrosion Effects of Hydrogen Sulphide and Carbon Dioxide in Oil Production*. World Petroleum Congress conference proceeding, Rome, Italy, June 6 - 15, 1955., p. 479-499.
14. Weil, E.D., S.R. Sandler, and M. Gernon, *Sulfur Compounds*, in *Kirk-Othmer Encyclopedia of Chemical Technology*, R.E. Kirk, John Wiley & Sons, Inc. 2000, p. 107-168.
15. Kane, R.D. and M.S. Cayard, *Roles of H_2S in the Behavior of Engineering Alloys: A Review of Literature and Experience*. Corrosion *98*, NACE International, San Diego Ca, March 22 - 27, 1998, Paper No.274.
16. Gerus, B.R.D., *Detection and Mitigation of Weight Loss Corrosion in Sour Gas Gathering Systems*, in *SPE Symposium on Sour Gas and Crude*. Tyler, Texas, 1974, paper No.:SPE 5188.

17. Gafarov, N., Gocharov, A., Grintsov, A. and Kushnarenko, V., *Corrosive media of Orenburg gas condensate field on the condition of metal structures.* Chemical and Petroleum Engineering, 1996. **32**(6): p. 610-614.
18. *NACE TM0177-Standard Test Method - Laboratory Testing of Metals for Resistance to Sulfide Stress Cracking and Stress Corrosion Cracking in H_2S Environments.*, NACE International, Houston, Tx., 2005.
19. Chattoraj, I., *The effect of hydrogen induced cracking on the integrity of steel components.* Sadhana-academy proceedings in engineering sciences,1995. **20**(1): p. 199-211.
20. Botvina, L., T. Tetyueva, and A. Ioffe, *Stages of multiple fracture of low-alloy steels in a hydrogen sulfide medium.* Metal Science and Heat Treatment, 1998. **40**(2): p. 61-70.
21. Kovalev, A.I., D.L. Wainstein, V.P.Mishina and V.V. Zabilsky, *Effect of Residual Stress on Hydrogen Embrittlement and Stress Corrrosion Cracking*, in *Handbook of Residual Stress and Deformation of Steel*, G. Totten, M. Howes, T.Inoue, ASTM International., 2002, p. 70-86.
22. Asahi, H., Y. Sogo, M. Ueno and H. Higashiyama, *Effects of Mn, P, and mo on sulfide stress cracking resistance of high strength low alloy steels.* Metallurgical and Materials Transactions A, 1988. **19**(9): p. 2171-2177.
23. Elboujdaini, M., R.W. Revie, V. S.Sastri, M.T. Shehata and R.R. Ramsingh, *Hydrogen-Induced Cracking and Effect of Non-Metallic Inclusions in Linepipe Steels*. Corrosion 98, NACE International, San Diego, Ca., March 22 - 27, 1998, Paper No.748.
24. *Reference Tool for Sour Service Conversion of Existing Carbon Steel Pipelines*, Alberta Energy and Utilities Board, Calgary, Alberta, 2004.
25. Troiano, A.R., *The role of hydrogen and other interstitials in the*

mechanical behavior of metals. Trans.ASM, 1960. **52**: p. 54.

26. Beachem, C.D., *A New Model for Hydrogen-Assisted Cracking (Hydrogen "Embrittlement").* Metallurgical and Materials Transactions B 1972. **3**: p. 437.
27. H.K.Birnbaum, Hydrogen Related Fracture of Metals, in *Atomistics of Fracture*, R.M. Latanision and J.R. Pickens, Plenum Press, Plenum, New York, 1983, p. 733.
28. Morasch, K.R. and D.F. Bahr, *The effects of hydrogen on deformation and cross slip in a BCC titanium alloy.* Scripta Materialia, 2001. **45**(7): p. 839-845.
29. Wen, M., S. Fukuyama, and K. Yokogawa, *Atomistic simulations of effect of hydrogen on kink-pair energetics of screw dislocations in bcc iron.* Acta Materialia, 2003. **51**(6): p. 1767-1773.
30. C.A.zapffe and C.E. Sims, *Hydrogen Embrittlement, Internal Stress and Defects in Steel.* Trans.AIME, 1941. **145**: p. 225.
31. Hancock, G.G. and H. H. Johnson, Trans. TMSAIME, 1965. **236**: p.513.
32. NACE *TM0284-Standard Test Method - Evaluation of Pipeline and Pressure Vessel Steels for Resistance to Hydrogen-Induced Cracking*, NACE International, Houston, Tx.,2003.
33. *ASTM G129-Standard Practice for Slow Strain Rate Testing to Evaluate the Susceptibility of Metallic Materials to Environmentally Assisted Cracking*, ASTM International, West Conshohocken, PA, 2006.
34. Sojka, J., M. Jérôme, M. Sozańska, P. Váňová, L. Rytířová, P. Jonšta, *Role of microstructure and testing conditions in sulphide stress cracking of X52 and X60 API steels.* Materials Science and Engineering: A, 2008. **480**(1–2): p. 237-243.
35. Ikeda, A., T. Kaneko, and Y. Ando, *On the evaluation method of sulfide stress cracking susceptibility of carbon and low alloy steels.* Corrosion

Science, 1987. **27**(10–11): p. 1099-1115.

36. Margot-Marette, H., G. Bardou, and J.C. Charbonnier, *The application of the slow strain rate test method for the development of linepipe steels resistant to sulphide stress cracking.* Corrosion Science, 1987. **27**(10–11): p. 1009-1026.
37. Hutchings, R.B. and A. Turnbull, *The effect of prior mechanical deformation on hydrogen transport through 13% chromium martensitic stainless steel.* Corrosion Science, 1992. **33**(5): p. 713-728.
38. I. Peñalva, G.A., F. Legarda, G. A. Esteban and B. Riccardi, *Interaction of Copper Alloys with Hydrogen*, in *Copper Alloys - Early Applications and Current Performance - Enhancing Processes*, L. Collini, Editor. 2012, InTech. p. 31-48.
39. Snape, E., *Sulfide Stress Corrosion of Some Medium and Low Alloy Steels.* Corrosion, 1967. **23**: p. 154-172.
40. C.M. Hudgins, R.L.M., P. Mehdizadeh and W.M. Rosborough, *Hydrogen Sulfide Cracking of Carbon and Alloy steels.* Corrosion, 1966. **22**: p. 238-251.
41. Kane, R.D. and J.B. Greer, *Sulfide Stress Cracking of High-Strength Steels In Laboratory and Oilfield Environments.* SPE Journal of Petroleum Technology, 1977(11): p. 1483-1488
42. Omura, T., K. Kobayashi, and M. Ueda, *SSC Resistance of High Strength Low Alloy Steel OCTG in High Pressure H_2S Environments*,. Corrosion 2009, NACE International, Atlanta, GA, March 22 - 26, 2009, Paper No.09102.
43. Asahi, H. and K. Nose, *Effects of Environmental Conditions on SCC Resistance of C125 OCTG*. Corrosion 99, NACE International, San Antonio, Tx, April 25 - 30, 1999, Paper No.601.
44. Gutzeit, J., *Cracking of Carbon Steel Components in Amine Service.* Mater. Perform., 1990. **29 (9)**(54).

45. Kobayashi, K., T.T. Omura, and M. Ueda, *Effect of Testing Temperature on SSC Properties of Low Alloy Steel*. Corrosion 2006, NACE International, San Diego Ca., March 12 - 16, 2006, Paper No.06127.

46. Vasilenko, I.I., O.Y. Shul'te, and O.I. Radkevich, *Effects of steel composition and production technology on hydrogen-induced cracking sensitivity and hydrogen sulfide corrosion cracking: Survey of foreign research.* Materials Science, 1991. **26**(4): p. 383-394.

47. Golovanenko, S.A., et al., *Effect of alloying elements and structure on the resistance of structural steels to hydrogen embrittlement.* Metal Science and Heat Treatment, 1978. **20**(1): p. 3-14.

48. Beidokhti, B., A. Dolati, and A.H. Koukabi, *Effects of alloying elements and microstructure on the susceptibility of the welded HSLA steel to hydrogen-induced cracking and sulfide stress cracking.* Materials Science and Engineering: A, 2009. **507**(1–2): p. 167-173.

49. *Forms of Corrosion in the Petrochemical Industry*, in *Corrosion in the Petrochemical Industry*, L. Garverick, Editor. 1994, ASM International: Materials Park, OH. p. 1-73.

50. D.L.Sponseller, R.G., and J.A. Straatmann, *Effect of Microstrucuture on Sulfide-Stress-Cracking Resistance of High-Strength Casing Steels*, in *MiCon 82: Optimization of Processing, Properties, and Service Performance through Microstructural Control*, H. Abrams, J. Hood and B.Seth, ASTM, Philadelphia, 1982, p. 172-204.

51. Hill, M., E.P. Kawasaki, and G.E. Kronbach, Materials Performance, 1972. **11**(January): p. 19-22.

52. Garber, P.J., D.L. Sponseller, and W.W. Cias, Materials Performance, 1975. **14**(6): p. 35-43.

53. W.K.Kim, K.Y.K., T.W.Yun and B.Y.Yang, *The Effect of Metallurgical Fractors on SSC of High Strength Pipeline Steel*. Corrosion, NACE

International, New Orlean, LA, 2008, Paper No.08496.

54. Holappa, L.E.K. and A.S. Helle, *Inclusion Control in High-Performance Steels.* Journal of Materials Processing Technology, 1995. **53**(1–2): p. 177-186.

55. Elboujdaini, M., C. Derushie, and R.W. Revie, *Effects of Metallurgical Parameters and Non-Metallic Inclusions on Behavior for Oil and Gas Industry Steels on Hydrogen Induced Cracking*. Corrosion, NACE International, San Diego, CA., March 2003, Paper No.03528.

56. Koh, S.U., B.Y. Yang, and K.Y. Kim, *Effect of Alloying Elements on the Susceptibility to Sulfide Stress Cracking of Line Pipe Steels.* Corrosion, Vol. **60**, No. 03, NACE International, 2004, p.262-274.

57. Al-Mansour, M., A.M. Alfantazi, and M. El-boujdaini, *Sulfide stress cracking resistance of API-X100 high strength low alloy steel.* Materials & Design, 2009. **30**(10): p. 4088-4094.

58. Ghosh, A., *Segregation in cast products.* Sadhana, Vol **26**(part 1 & 2), 2001, p. 5-24.

59. Fujda, M., *Centerline Segregation of Continuously Cast Slabs Influence on Microstructure and Fracture Morphology.* Journal of Metals,Materials and Minerals (JMMM), 2005. Vol **15**(2): p. 45-51.

60. Lement, B.S., Averback, B.L. and Cohen, M., *Further Study of Microstructural Changes on Tempering Iron-Carbon Alloys.* Trans ASM, 1955. **47**: p. 291-319.

61. McIntyre, D.R., *Ranking Materials for Extreme Sour Gas Service Using the Slow Strain Rate Method*, in *Hydrogen Embrittlement: Prevention and Control, ASTM STP 962*, L.Raymond, American Society for Testing and Materials (ASTM): Philadelphia, 1988, p. 178-189.

62. *ASTM E45-05:Standard Test Methods for Determining the Inclusion Content of Steel*, ASTM International, West Conshohocken, PA., 2005.

63. *JIS G0555-Microscopic Testing Method for the Non-Metallic*

Inclusions in Steels, Japanese Standards Association, Tokyo, Japan, 2003.

64. Yu, G.H., et al., *Hydrogen Accumulation and Hydrogen-Induced Cracking of API C90 Tubular Steel.* Corrosion, 1997. **53**(10): p. 762-769.

65. Jin, T.Y., Z.Y. Liu, and Y.F. Cheng, *Effect of non-metallic inclusions on hydrogen-induced cracking of API5L X100 steel.* International Journal of Hydrogen Energy, 2010. **35**(15): p. 8014-8021.

66. Kaneko, T., Y. Okada, and A. Ikeda, *Influence of Microstructure on SSC Susceptibility of Low-Alloy, High-Strength Oil Country Tubular Goods.* Corrosion, 1989. **45**(1): p. 2-6.

67. R.Brachvogel, L.E.Collins, R. O'Hara and M.Kostic. *Development of ERW Casing for Horizontal/Thermal Wells*, Materials for Resource Recovery and Transport proceeding, Canadian Institute of Mining, Metallurgy, and Petroleum, Calgary, Alberta, August 16-19, 1998.

68. Liao, C.-M. and J.-L. Lee, *Effect of Molybdenum on Sulfide Stress Cracking Resistance of Low-Alloy Steels.* Corrosion, Vol. **50**, No. 9, 1994, pp. 695-704.

69. H.-Y. Liou, F.-I.W., S.-C. Wang and R.-I. Shieh, *Roles of Microalloying Elements in Hydrogen Induced Cracking Resistant Property of HSLA Steels.* Corrosion, Vol. **49**, No. 5, 1993, p.389-398.

70. Kang, H.J., Jae Seok Yoo, Ji Tae Park, Soon Tae Ahn, Namhyun Kang and Kyung-Mox Cho, *Effect of nano-carbide formation on hydrogen-delayed fracture for quenching and tempering steels during high-frequency induction heat treatment.* Materials Science and Engineering: A, 2012. **543**(0): p. 6-11.

71. Pressouyre, G., *A classification of hydrogen traps in steel.* Metallurgical and Materials Transactions A, 1979. **10**(10): p. 1571-1573.

72. Lee, H.G. and J.-Y. Lee, *Hydrogen trapping by TiC particles in iron.*

Acta Metallurgica, 1984. **32**(1): p. 131-136.

73. Ohmisawa, T., S. Uchiyama, and M. Nagumo, *Detection of hydrogen trap distribution in steel using a microprint technique*, Journal of Alloys and Compounds, 356–357, 2003, p.290–294.

74. Garet,M.,A.M.Brass, C. Haut, F. Guttierez-solona, *Hydrogen trapping on non-metallic inclusions in Cr-Mo low alloy steels*,Corrosion Science, Vol. **40**, No.7, Pergamon, Great Britain, 1998, p.1073-1086.

APPENDIX A-PROOF RING CALIBRATION CHART

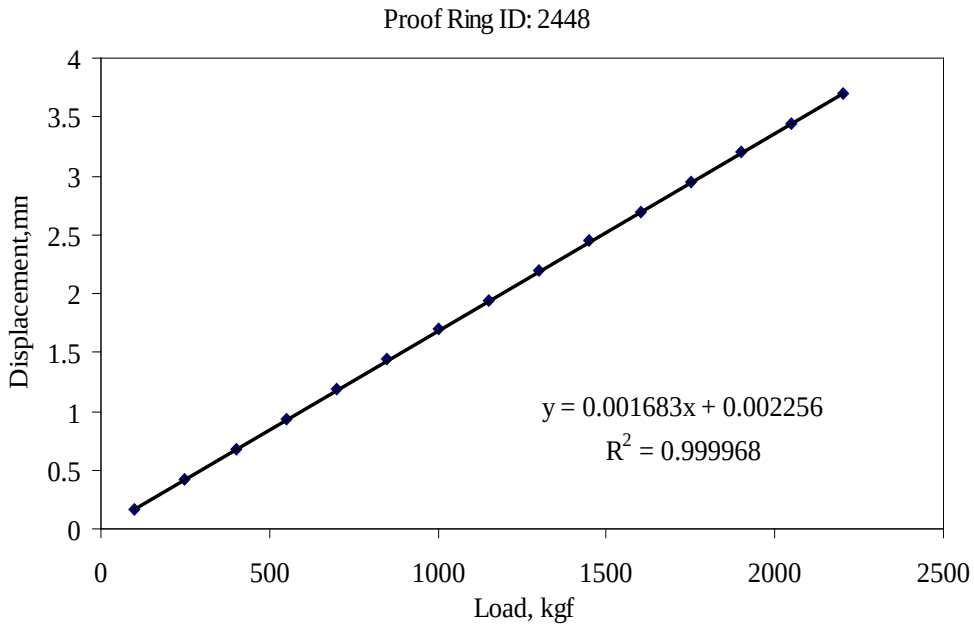

Figure A1: Calibration chart for proof ring.

Table A1: Proof ring calibration data.

Axial load	Deflection
(kgf)	(mm)
100	0.159
250	0.417
400	0.673
550	0.929
700	1.184
850	1.438
1000	1.692
1150	1.945
1300	2.197
1450	2.448
1600	2.698
1750	2.948
1900	3.198
2050	3.446
2200	3.694

APPENDIX B-SAFE OPERATING PROCEDURE FOR H_2S TEST

SCOPE:

Hazard Identification:

1.36 kg (3 lb) cylinder (or a cylinder max. 8 kg by weight) of hydrogen sulfide gas is used for the duration of this experiment.

Hydrogen sulfide is a toxic, flammable liquid and gas under pressure. It may be fatal if inhaled. It can form explosive mixtures with air and may cause respiratory tract and central nervous system damage. The gas deadens the sense of smell and the symptoms may be delayed.

The effects of a single (acute) overexposure

- Inhalation – Depresses activity of the central nervous system, causing respiratory paralysis. Effects of overexposure include headache, dizziness, vertigo, giddiness, confusion, chest pains, olfactory fatigue, unconsciousness, and death. Rhinitis, pharyngitis, pneumonitis, pulmonary edema, and cyanosis may occur. The lack of oxygen can kill.
- Skin Contact – Irritates the skin, causing local redness and swelling. Liquid may be corrosive and cause frostbite, a cryogenic injury resembling a burn.
- Swallowing – A highly unlikely route of exposure; this product is a gas at normal temperature and pressure, but frostbite of the lips and mouth may result from contact with the liquid.
- Eye Contact – Irritates the eyes, causing excess redness of the conjunctiva.

Below is a table that summarizes the health affects from short-term exposure to hydrogen sulfide.

Table B1: Health effects from short term exposure to H_2S.

Concentration (ppm)	Health effect
0.01 – 0.3	Odour threshold.
1-20	Offensive odour, possible nausea, tearing of the eyes or headaches with prolonged exposure.
20-50	Nose, throat and lung irritation; digestive upset and loss of appetite; sense of smell starts to become fatigued; acute conjunctivitis may occur (pain, tearing and light sensitivity).
100-200	Severe nose, throat and lung irritation; ability to smell odour completely disappears.
250-500	Pulmonary edema (build up of fluid in the lungs)
500	Severe lung irritation, excitement, headache, dizziness, staggering, sudden collapse (knockdown), unconsciousness and death within a few hours, loss of memory for the period of exposure.
500-1000	Respiratory paralysis, irregular heart beat, collapse and death without rescue.
>1000	Rapid collapse and death

Handling acid and alkali: Acetic acid and sodium hydroxide are used in the test. The MSDS information on these chemicals must be read. Safety precaution should be applied when handling corrosive, flammable, toxic chemicals. Personal protective equipment should be worn: safety glasses, rubber gloves to prevent skin exposure, or respirator etc. The corrosive, toxic chemicals should be handled in a well-ventilated fume hood.

Training Required:

- All personnel involved into this experiment should be WHMIS trained.
- All personnel should be acquainted with the Hazard Assessment Sheets (MSDS Sheets) for the area and be trained to use the personal protective equipment (PPE) and how to act in emergency situations.
- All personnel performing the test should be familiar with NACE TM0177-2005 standard.
- The proper waste handle training in accordance with University of Alberta and Chemical and Materials Engineering Department requirements should be provided.

Control/Protective Measures:

- The test should perform in a ventilated fume hood.
- Ensure H_2S cylinder is properly anchored at all times.
- Ensure area around the fume hood is clear to allow adequate room to carry out the experiment.
- Check high pressure gauge frequently to ensure proper working condition.
- Three single H_2S gas detectors type "Altair" are used to detect the H_2S concentration in the area. One is mounted inside the ventilated hood in the proximity of the H_2S cylinder, a second – at the wall down near the floor nearby the hood, the third one – on the heap of the operator. All three detectors are to be kept on at all times. If any of 3 gas detectors is alarmed (i.e. loud sound and flash light are on) the valve at H_2S cylinder must be shot down, and all personnel should leave the dangerous area immediately.
- Fire extinguisher in good working state should be located at working area.
- The fume hood sashes should be moved down to slot level no more than 12".
- All H_2S gas lines should be equipped with stop- and check valves.
- The three gas detectors will be calibrated once per year.

- A plastic chemical resistant tray (with dimension 36”x24”x1.5”, able to contain 5000 mL solution) is placed under the test cell (500mL/cell) to contain the spill solution in case the Pyrex test vessel breaks during the test.
- Prepare sodium hydroxide (~2L, 25% concentration) as a scrubber solution to neutralize the outlet H_2S gas from the test cell to further reduce the amount of H_2S.
- Ensure the scrubber solution is clear, replace the solution if it turns milky.
- Talk to the people in the lab CME 213 and the office area outside CME213 to make sure them aware of the H_2S test and review emergency response procedure with them.

Emergency Procedures:

- Any leak of Hydrogen Sulfide gas should be documented and reported to Mrs. Andee Koenig, CME Safe and Healthy Officer, at 2-5159.
- Before starting any activity involving H_2S gas, all accesses to the area should be marked with sign “Do not enter! Hazardous gas test is in progress!”, and all personnel that are not involved in the test should leave the area.
- All electrical equipment should be in spark-proof performance.
- The test shall be performed in a well-ventilated fume hood to exhaust all of H_2S flow. The H_2S flow rates should be kept low to minimize the quantity exhausted.
- A 25% NaOH scrubber solution for effluent gas is used to further minimize the quantity of exhausted gas. This solution needs periodic replenishment at the moment when its color changes in milk-white or yellow.

General Test Procedure

Solution preparation

There are three test solutions described in the NACE0177-2005 standard. Only test solution A is used in this procedure. Test solution A contains 5.0wt% sodium chloride (NaCl) and 0.5wt% glacial acetic acid (CH_3COOH) dissolved in distilled water and saturated with H_2S. Reagent grade solvent or chemically pure (>99.5% purity) chemicals shall be used for the test.

1. To prepare 1 litre of solution A, the following should prepare using any appropriate measuring devices:

• 50.0g NaCl

• 5.0g glacial acetic acid

• 945g distilled water

2. Mix the solution well in a vessel (not the Pyrex vessel of the proof ring).
3. Use a thermometer to check the temperature of the solution. The test solution shall be maintained at 24 ±3°C.
4. De-aerate with N_2 at a rate of at least 100mL/min for 1 to 1.5 hours for 1L of solution.
5. Prepare ~2L, 25% sodium hydroxide as a scrubber solution to neutralize the outlet H_2S gas from the test cell to further reduce the amount of H_2S. (Note: Ensure the scrubber solution is clear, replace the solution if it turns milky or yellow.)

Calculation of the required ring deflection

1. Measure the minimum gauge diameter (d) of the test specimens using a micrometer.
2. Calculate the cross section area ($A=\pi/4\times d2$) of the gauge section.
3. Calculate the load (P) for stressing the specimen: $P=S\times A$; where S is the desired stress (e.g. use 85% Specified Minimum Yield Stress).
4. Use the proof ring calibration chart to determine the ring deflection required to obtain the desired load P. Record the ring deflection value.

Set up the test

1. Insert o-rings in top and bottom of the Pyrex test vessel.
2. Insert Teflon seats in top and bottom of the Pyrex test vessel, ensure the bottom Telflon seat is tight.
3. Put on small o-ring on one end of the specimen, insert it through both top and bottom Teflon seats, tighten it into one stainless steel grip.
4. Apply small o-ring, tighten stainless steel grip to the other end of the specimen.
5. Thread the bottom stainless steel grip on the stud of the ring assembly. At least half of the threads of the stud should be engaged in the stainless steel grip.
6. Thread the top stainless steel grip to the loading bolt, ensure at least half of the threads are engaged.
7. Loosen the loading bolt a bit to make sure no load applied on the specimen.
8. Adjust the height of the dial displacement gauge on a stand and touch the probe of the dial indicator perpendicularly to the top ring surface. Adjust the indicator to zero by loosening the outer indicator ring when the proof ring is unloaded at this time. (Note: the Teclock model AI-921dial indicator (from CME 416) is used. It has 0.001" increment, range of indicator is 1.0". The Teclock AI-921 dial indicator from CME 416 has been calibrated before.)
9. Use the calculated value, deflect the ring to the prescribed strain by turning the loading nut.
10. Fill the Pyrex vessel with the prepared de-aerated test solution to immerse the whole gauge section of the specimen.
11. Purge the cell with N_2 for 20 minutes at a rate of at least 100mL/min.
12. Loosen the screw on Microswitch Support and adjust Microswitch so that it has just tripped on the inside of the proof ring. This will connect to the Cortest Timer to record the duration of the test.

13. Introduce H_2S for 10 to 30 minutes at a rate of at least 100mL/min. (Note: The saturation process must be handled in a well-ventilated fume hood.)
14. Turn down the flow rate of H_2S to produce a bubble every 1-2 seconds.
15. Reset the Timer of Cortest Control Panel, and start the test period.

Hazardous Waste Disposal Procedures

All hazardous waste shall be disposed through the University hazardous waste management system. Hazardous waste pick-up requests can be made through Chematix.

Equipment Maintenance Procedures

- Calibration and maintenance of the H_2S detector.
- Regular checks of the regulator assembly on the cylinders to ensure the connections are free of debris, corrosion etc.
- The cylinder is replaced when the pressure drops till 0.5-0.7 MPa because regulator control may become erratic.
- Maintain records.

Prepared By: Weishan (Sandy) Huang

Approved by: Hani Henein, Jingli Luo

Date: August 31, 2010

(Department Chair)Fraser Forbes